BERGISCHE
UNIVERSITÄT
WUPPERTAL

Lehrstuhl für
Großflächige
Opto-
Elektronik

Nonlinear Optical Waveguide and Material Concepts for Enhanced Sensing and Light Manipulation

Zur Erlangung des akademischen Grades eines
Doktors der Ingenieurwissenschaften (Dr.-Ing.) genehmigte

Dissertation

von M. Sc. Maximilian Buchmüller

an der Fakultät 6 - Elektrotechnik,
Informationstechnik und Medientechnik.

Referenten:
Prof. Dr.-Ing Patrick Görrn
Prof. Dr. rer. nat. Thomas Riedl

Bergische Universität Wuppertal

2025

Preface

First, I would like to express my deepest gratitude for the opportunity to pursue my PhD at the Chair of Large Area Optoelectronics, University of Wuppertal. In particular, I would like to thank Prof. Dr.-Ing. Patrick Görrn, my supervisor and “Doktorvater”, for his continuous support, guidance, and dedication ever since I started my work at the chair. He consistently gave me the freedom to follow my own path, while always supporting me when I was stuck or needed advice. I will never forget his trust and encouragement he invested in me and my work. Thank you, Patrick!

Next, I would also like to thank all my current and former colleagues at our chair for the great collaboration and the productive atmosphere throughout my PhD time. I am grateful for the many helpful discussions, the teamwork, and the moments of success (and also failure) that we experienced together, which made this journey truly memorable. Hoping that I haven’t forgotten anyone, I would like to mention by name: M. Sc. René Anfang, Dr. Su Bongu, M. Sc. Shahrzad Dehghani, M. Sc. Shaghayegh Eskandari, M. Sc. Andreas Henkel, M. Sc. Christopher Knoth, Dr.-Ing. Maik Meudt, B. Sc. Janna Neumann, M. Sc. Sven Oliver Schumacher, and Dr.-Ing. Ivan Shutsko. Much of the results presented in this thesis were not achieved by our chair alone but were made possible through close collaboration with many dear colleagues from other chairs and research groups. In this context, I would like to thank my second referee Prof. Dr. Thomas Riedl, both for serving as co-referee of my dissertation and for the great collaboration over the past years. I thereby also want to extend my thanks to his entire team at the Chair of Electronic Devices for their support and productive collaboration as well as all other industry and academic partners.

Last but not least I would like to thank my family and friends—without whom I would not be writing these acknowledgements today. I am especially grateful to my parents, Martina and Andreas; my aunt Tina and uncle Dirk; my grandmother Rosi, who sadly passed away too early to see this achievement, and my partner Anna for their unconditional support, for many valuable pieces of advice and perspective, and for their patience and thoughtfulness—especially during difficult times. Thank you for your constant understanding when, alongside my work, other things occasionally had to take a back seat. I could never have done this without you. Thank you!

List of Publications

Journal Articles

1. A. Henkel, C. Knoth, M. Buchmüller, and P. Görrn
   Electric Control of the In-Plane Deflection of Laser Beam Pairs within a Photonic Slab Waveguide
   Optics 5 (3), 342-352 (2024)

2. N. Kurahashi, M. Runkel, C. Kreusel, M. Schiffer, T. Maschwitz, R. Heiderhoff, M. Buchmüller, S.O. Schumacher, J. Brunner, Y. Vaynzof, P. Görrn, and T. Riedl
   Distributed Feedback Lasing in Thermally Imprinted Phase-Stabilized Cesium Lead Iodide Thin Films
   Advanced Functional Materials 34, 2405976 (2024)

3. S.R. Bongu, M. Buchmüller, D. Neumaier, and P. Görrn
   Introducing Optical Nonlinearity in PDMS using Organic Solvent Swelling
   Optics 5 (1), 66-75 (2024)

4. S.R. Bongu, M. Buchmüller, D. Neumaier, and P. Görrn
   Electric Control of Thermal Contributions to the Nonlinear Optical Properties of Nitrobenzene
   Advanced Physics Research 3, 2300053 (2024)

5. A. Henkel, M. Meudt, S.O. Schumacher, C. Knoth, M. Buchmüller, and P. Görrn
   High Contrast Switching of Light Enabled by Zero Diffraction
   Advanced Photonics Research 4, 2300230 (2023)

6. M. Buchmüller, I. Shutsko, S.O. Schumacher, and P. Görrn
   Harnessing Short-Range Surface Plasmons in Planar Silver Films via Disorder-Engineered Metasurfaces
   ACS Applied Optical Materials 1, 11, 1777-1782 (2023)

7. I. Shutsko, M. Buchmüller, M. Meudt, and P. Görrn
   Light-Controlled Fabrication of Disordered Hyperuniform Metasurfaces
   Advanced Materials Technologies 7, 2200086 (2022)

8. I. Shutsko, M. Buchmüller, M. Meudt, and P. Görrn
   Plasmon-Induced Disorder Engineering for Robust Optical Sensors
   Advanced Optical Materials 10, 2102783 (2022)

9. M. Meudt, A. Henkel, M. Buchmüller, and P. Görrn
   A Theoretical Description of Node-Aligned Resonant Waveguide Gratings
   Optics 3 (1), 60-69 (2022)

10. N. Pourdavoud, A. Mayer, M. Buchmüller, K. Brinkmann, T. Häger, T. Hu, R. Heiderhoff, I. Shutsko, P. Görrn, Y. Chen, H.-C. Scheer, and T. Riedl
    Distributed Feedback Lasers Based on MAPbBr3
    Advanced Materials Technologies 3, 1700253 (2018).

11. Mayer, M. Buchmüller, S. Wang, C. Steinberg, M. Papenheim, H.-C. Scheer, N. Pourdavoud, T. Haeger, and T. Riedl: Thermal Nanoimprint to Improve the Morphology of MAPbX3
    Journal of Vacuum Science and Technology B 35, (2017)

Conference Contributions

1. M. Buchmüller
   Light-Controlled Disorder-Engineering of Optical Metasurfaces
   MRS Graduate Student Award Presentation
   MRS Spring Meeting, Seattle (USA), (2024)
   MRS Graduate Student Silver Award

2. M. Buchmüller, S.O. Schumacher, and P. Görrn
   Light-Controlled Disorder-Engineering of Optical Metasurfaces: Aspects of Design and Applications
   MRS Spring Meeting, Seattle (USA), 2024

3. M. Buchmüller, A. Henkel, S.O. Schumacher, C. Knoth, and P. Görrn
   Zero Diffraction: A Novel Approach for High-Contrast Switching of Light
   MRS Spring Meeting, Seattle (USA), 2024

4. M. Runkel, T. Kraus, T. Maschwitz, C. Kreusel, K. Brinkmann, M. Buchmüller, P. Görrn, S. Olthof, and T. Riedl
   Room-Temperature Amplified Spontaneous Emission and Lasing in Recrystallized Cesium Tin Bromide Perovskite Thin Films
   MRS Fall Meeting, Boston (USA), 2023

5. M. Buchmüller, I. Shutsko, and P. Görrn
   Light-Controlled Disorder-Engineering for Functional Optical Metasurfaces
   World Congress of Advanced Materials Science, Barcelona, Spain, 2023

6. P. Görrn, A. Henkel, M. Meudt, and M. Buchmüller
   Optical Sensors Based on Symmetric Waveguide Gratings
   World Congress of Advanced Materials Science, Barcelona, Spain, 2023

7. M. Buchmüller, A. Henkel, M. Meudt, and P. Görrn
   Hybrid Photonic-Plasmonic Bound States in Continuum
   MRS Spring Meeting, Honolulu (USA), EQ10.09.10, 2022
   Nanophotonics Best Student Presentation Award

8. A. Henkel, M. Meudt, M. Buchmüller, C.Knoth, and P. Görrn
   Switchable Waveguides for Novel Laser Displays and Scanners
   MRS Spring Meeting, Honolulu (USA), EQ10.08.08, 2022

9. N. Pourdavoud, A. Mayer, M. Buchmüller, K. Brinkmann, T. Häger, T. Hu, R. Heiderhoff, I. Shutsko, P. Görrn, Y. Chen, H.-C. Scheer, and T. Riedl
   Low-Threshold Distributed Feedback Lasers Based on Thermally Imprinted MAPbBr3
   MRS Fall Meeting, Boston (USA) ES01.12.09, 2017

10. N. Pourdavoud, A. Mayer, S. Wang, M. Buchmüller, K. Brinkmann, T. Haeger, T. Hu, R. Heiderhoff, A. Marianovich, I. Shutsko, P. Görrn, Y. Chen, W. Kowalsky, H.-C. Scheer, and T. Riedl
    Low-threshold Distributed Feedback Lasers Prepared by Direct Thermal Nanoimprint of Resonator Gratings into Organo-Metal Halide Perovskites
    Photonics @ SG, Singapore (Singapore), 2017
    Nature Photonics Best Student Paper Award

Preprints

1. M. Buchmüller, I. Shutsko, S. O. Schumacher, and P. Görrn
   Harnessing Short-Range Surface Plasmons in Planar Silver Films via Disorder-Engineered Metasurfaces
   arXiv:2305.09983 (2023)

2. A. Henkel, M. Meudt, M. Buchmüller, and P. Görrn
   Electrically Switchable Broadband Photonic Bound States in the Continuum
   arXiv:2102.01686 (2021)

Table of Contents

Chapter 1

Introduction

Optical devices and systems, especially based on waveguides, play a crucial role in various modern fields of technology. Among others, these fields are communication including augmented and virtual reality technologies[1–3], healthcare[4–8], advanced manufacturing[9–11], as well as energy and environment[12–14]. Furthermore, quantum technologies are among the candidates that increasingly rely on advanced optical devices and systems[15,16].

Optical waveguides are fundamental components in many of these fields. They can be used to precisely direct and control the propagation of light in space. One prominent example is glass fibres, which are widely used in communication technology to transmit light over long distances with minimal losses and high bandwidth[17]. In fact, these low losses essentially mean minimal interaction with the surrounding environment of the fibre. However, there are also other types and applications of optical waveguides designed specifically to be highly sensitive to changes in the surroundings e.g. for optical sensing. Such waveguides often consist of more complex layer stacks compared to glass fibres and feature micro- and nanostructures[18]. A common challenge in using highly sensitive optical waveguides in sensing is the complex alignment requirements between the waveguide and the light source, particularly in miniaturized or even integrated systems.

Additionally, the spatial control of light in most waveguides is static, meaning that the propagation direction of light is predetermined by the waveguide geometry. However, achieving dynamic spatial control of light would be of significant technological relevance for a variety of applications. Currently, spatial control of light is typically achieved through mechanically movable components such as mirrors or lenses, which makes it relatively slow. Even miniaturization concepts, e.g. based on micro-electromechanical systems could only achieve response times in the order of milliseconds[19,20].

For many applications, such as optical environmental mapping, much faster spatial control would be desirable. Optical structures in combination with nonlinear waveguides, which are tuneable through optical nonlinearity, could offer a novel approach to enable ultra-fast spatial control of light with response times down to a few picoseconds[21].

Furthermore, many of the future prospects in quantum technologies will only reach their full potential once effective scaling is achieved. Also in this case, nonlinear optical waveguides are an essential component, as they provide an optical interface capable of addressing individual qubits[22]. Many classical nonlinear materials that enable refractive index modulation e.g. via the Pockels effect, induced by an electric field, often require complex manufacturing methods involving high-vacuum conditions. This includes commonly used single-crystals like lithium niobate. Alternative materials, such as semiconductors or dye-doped polymers are often limited by high absorption, which restricts their use in applications with large propagation lengths, such as waveguides[23]. On the other hand, nonlinear liquids, while showing promising nonlinearity and transparency, are also challenging to integrate with rigid waveguide layer stacks[24].

Therefore, the further development of nonlinear waveguides for advanced sensing and light manipulation essentially has two key aspects. First, the design and arrangement of novel waveguide geometries that exhibit high sensitivity towards changes in the electromagnetic environment. Second, the development of transparent nonlinear optical materials that are compatible with polymer technology.

This thesis will focus on developing waveguides and materials that address these two aspects. For a better understanding of this work, a few fundamentals of electromagnetics will be covered at the beginning of Chapter 2. In addition, an introduction to the fundamentals of optical waveguides including photonic and plasmonic waveguides will be provided. This section will also discuss various types of optical nonlinearity that will be relevant throughout this thesis. Furthermore, optical surface structures in the form of metasurfaces will be introduced, along with common fabrication methods. Chapter 2 concludes with an introduction to the topic of swelling, a fundamental phenomenon used in Chapter 6 to integrate nonlinear liquids into highly transparent polymers.

In Chapter 3, the experimental methods used in this thesis will be explained. First, the fabrication methods will be discussed. These include primarily the light-controlled fabrication of optical metasurfaces via the growth of metal nanoparticles from the liquid phase, as well as the fabrication of PDMS composite materials incorporating nonlinear optical liquids. Additionally, methods for characterizing the fabricated waveguides and materials will be explained.

Chapter 4 focuses on designing and implementing sensitive waveguides based on photonic waveguide effects. The goal is to vary the propagation length of light, which is guided within the waveguide, by tuning the interaction with an optical grating. The diffraction at the grating also enables to change propagation direction and thus provides spatial control. Additionally, the phenomenon of zero diffraction, which was discovered in the course of this research, is discussed from the experimental perspective. In this context, extensive simulation studies will be performed in addition to experimental contrast measurements.

Chapter 5 will focus on plasmonic waveguides. The goal is to achieve an adaptation of the optical structure to the specific light source by using light-induced fabrication of plasmonic metasurfaces. It will be investigated whether using the identical fabrication and probing environment enables achieving high sensitivity and could eliminate the need for post-process alignments. Furthermore, it will be demonstrated that this method also makes phenomena such as plasmon hybridization more easily accessible in practise. The metasurfaces will be investigated in reciprocal space as well as attenuated total reflection measurements are performed to investigate the sensing performance.

Chapter 6 focuses on nonlinear optical materials, with an emphasis on nonlinear liquids, which are initially integrated into PDMS through a swelling process. The swelling behaviour of various material combinations is analysed. For a selected material, the thermal nonlinearity and its associated timescales are further investigated. Finally, dielectric elastomer actuators are discussed as an alternative approach for switching the phase of an optical wave.

The thesis concludes with a summary and outlook on future research activities in this field.

Chapter 2

Fundamentals

This chapter starts by introducing Maxwell's equations, which describe the origin and interaction of electric and magnetic fields and serve as the foundation of modern electrodynamics. Following this, an introduction to nonlinear optics (NLO) will be given, covering phenomena such as the Pockels effect, the optical Kerr effect, and nonlinear absorption phenomena. Nonlinear optics can be seen as a bridge between optics and electronics, as NLO phenomena enable the control of light via refractive index changes in response to an external electric field. To harness NLO effects more effectively, it can be advantageous to confine light within small volumes, thereby increasing local electric field intensity. Among the many design options, slab waveguides are among the most common optical resonator designs, functioning as optical resonators that guide light within a thin layer. Even stronger light-matter interactions can be achieved using plasmonic waveguide structures that incorporate metals. Central to these waveguide configurations are modern nanopatterning techniques, which allow for the precise fabrication of complex optical structures. A brief introduction to these topics will also be provided in this chapter. Finally, the chapter will conclude with a discussion of metasurfaces, disorder engineering, and the concept of swelling of soft polymers.

2.1. Maxwell‘s and Wave Equations

The wave equations in the form of the Helmholtz equation form the foundation for electrodynamics, describing the interplay between electric and magnetic fields and their propagation both in free-space and in matter. In addition to the four fundamental Maxwell equations, two material equations provide a framework for a general understanding and description of electromagnetic phenomena.

The Maxwell equations in the differential form are[25]:

1) Gauss's Law

$$\vec{\nabla} \cdot \vec{D} = \rho_{ext} \tag{2.1}$$

2) Gauss's Law of Magnetism

$$\vec{\nabla} \cdot \vec{B} = 0 \tag{2.2}$$

3) Faraday's Law of Induction

$$\vec{\nabla} \times \vec{E} = -\frac{\partial \vec{B}}{\partial t} \tag{2.3}$$

4) Ampere's Law

$$\vec{\nabla} \times \vec{H} = \vec{J}_{ext} + \frac{\partial \vec{D}}{\partial t} \tag{2.4}$$

The Maxwell equations link the four vector fields $\vec{D}$ (electric flux density), $\vec{B}$ (magnetic flux density), $\vec{E}$ (electric field vector), and $\vec{H}$ (magnetic field vector), where ∇ is the Nabla-operator.

$$\vec{\nabla} = \begin{pmatrix} \partial/\partial x \\ \partial/\partial y \\ \partial/\partial z \end{pmatrix}$$

External stimuli of the electric and magnetic field are an external charge carrier density ρ_{ext}, and an external electric current density $\vec{J}_{ext}$.

While 2.1 and 2.2 show that electric charges are the source of electric fields and that magnetic fields have no intrinsic sources, 2.3 and 2.4 describe that a temporal change in either field can induce the other. This interdependence eventually forms the foundation for propagating electromagnetic waves. Furthermore, the electric flux density $\vec{D}$ and the electric field vector $\vec{E}$ as well as the magnetic flux density $\vec{B}$ and the magnetic field vector $\vec{H}$ are linked by the vacuum permittivity ε_0 and the vacuum permeability μ_0.

$$\vec{D} = \varepsilon_0 \vec{E}$$

$$\vec{B} = \mu_0 \vec{H}$$

Both quantities, ε_0 and μ_0, are physical constants with the $\varepsilon_0 \approx 8.854 \cdot 10^{-12}\ \mathrm{F/m}$ and $\mu_0 \approx 1.256 \cdot 10^{-6}\ \mathrm{H/m}$.

In vacuum, and thus in the absence of any external charges or currents (ρ_{ext} , $\vec{J}_{ext} = 0$), the Maxwell equations can be used to derive the vacuum wave equation.

$$\Delta\vec{E} - \frac{1}{c_0^2}\frac{\partial^2\vec{E}}{\partial t^2} = 0 \tag{2.5}$$

with $c_0 = \frac{1}{\sqrt{\varepsilon_0\mu_0}} \approx 3 \cdot 10^8\ \mathrm{m/s}$ being the vacuum speed of light and Δ being the Laplace operator in Cartesian coordinates. The wave equation for the magnetic field can be derived in the same manner.

$$\Delta = \vec{\nabla}^2 = \frac{\partial^2}{\partial x^2} + \frac{\partial^2}{\partial y^2} + \frac{\partial^2}{\partial z^2}$$

To describe the behaviour of electromagnetic fields in the presence of matter, two material equations enable to link the fields and the properties of the ambient material. For the electric field quantities, the material equation can be expressed as follows:

$$\vec{D} = \varepsilon_0\vec{E} + \vec{P} = \varepsilon_0\vec{E} + \varepsilon_0\chi\vec{E} = (1+\chi)\varepsilon_0\vec{E} = \varepsilon_r\varepsilon_0\vec{E} \tag{2.6}$$

The polarization $\vec{P}$ is related to the electric field vector $\vec{E}$ through the dielectric susceptibility $\vec{P} = \varepsilon_0\chi\vec{E}$, and $\varepsilon_r = 1 + \chi$ is the relative permittivity of the material, which quantifies to what extend a material can be polarized in response to an electric field. For most materials as well as for moderate electric field strengths, the polarization changes linearly with the electric field. However, there are cases in which higher order dependencies can become relevant. Such cases will be discussed in section 2.2.

In general, the dielectric susceptibility χ as well as the relative permittivity ε_r are second-rank tensor quantities, and thus can also describe materials with dielectric properties that depend on the orientation of the electric field within the medium. Such media are then referred to as anisotropic. Typically, many crystalline materials such as $BaTiO_3$ (barium titanate), or KPT (potassium titanyl phosphate), but also polymers such as polystyrene, show anisotropy in their dielectric (and thus also optical) properties[26–28]. However, in the more common and simpler case of isotropic media—where the material properties are the same in all spatial

directions or light is polarized along specific crystal axes—both χ and ε_r can be considered scalars.

In analogy, a material equation can be expressed for the magnetic field taking into account that certain material can magnetize in response to a magnetic field. Hence, the material equation includes a magnetization term $\vec{M} = \chi_m \vec{H}$, with the relative permeability $\mu_r = 1 + \chi_m$. In this thesis, as it is common in optics, only non-magnetic materials are considered. This assumption enables to set μ_r to 1, which simplifies the link between the magnetic flux density $\vec{B}$ and the magnetic field vector $\vec{H}$ to $\vec{B} = \mu_0 \vec{H}$.

By introducing the material equations into the Maxwell equations, the wave equation for an insulating, non-magnetic, and isotropic medium can be derived as

$$\Delta \vec{E} - \frac{\varepsilon_r}{c_0^2} \frac{\partial^2 \vec{E}}{\partial t^2} = 0 \tag{2.7}$$

This wave equation enables to describe all linear electromagnetic phenomena, including refraction, scattering, and diffraction.

In optics, the refractive index $n = \sqrt{\varepsilon_r}$ is often used to describe interactions between electromagnetic fields and matter at optical frequencies. The refractive index is a fundamental parameter because it directly influences how light propagates through a material. Additionally, these quantities are generally complex quantities $\underline{n} = n + j\kappa = \sqrt{\underline{\varepsilon_r}} = \sqrt{1 + \underline{\chi}}$. The imaginary part accounts for the damping or amplification of electromagnetic waves within a medium due to absorption or gain, while the real part determines the velocity of the wave. For instance, the speed of light c within a medium is given by $c = c_0/n$. This relationship indicates that light propagates more slowly in a medium with a refractive index larger than 1 compared to its speed in a vacuum. In this thesis, often only the real part of the refractive index is considered, unless otherwise noted at specific positions.

In optics, it is furthermore convenient to assume time-harmonic fields of the form

$$\vec{E}(\vec{r}, t) = \vec{E}_0(\vec{r}) e^{-i\omega t} \tag{2.8}$$

Here, $\vec{E}_0$ is the amplitude vector and ω is the angular frequency $\omega = 2\pi f$ with frequency f. This assumption of time-harmonic fields is particularly useful to describe monochromatic electromagnetic waves, such as laser radiation often considered in this thesis.

By inserting equation 1.8 in the wave equation 1.7 yields

$$\Delta\vec{E} + k_0^2 \varepsilon_r \vec{E} = 0, \tag{2.9}$$

which is known as the Helmholtz equation with the vacuum wave number, or optical momentum, $k_0 = \omega/c_0 = 2\pi/\lambda_0$. The fundamental advantage of this transformation of the general wave equation into the form of the Helmholtz equation lies in the separation of time and spatial dependence.

Mathematically the simplest solution for the Helmholtz equation is a plane wave of the form

$$\vec{E}(\vec{r}, t) = \vec{E}_0 e^{j(\vec{k}_0\vec{r} - \omega t + \varphi_0)} \tag{2.10}$$

Here, E_0 is the amplitude of the electric field, $\vec{k}_0$ is the vacuum wave vector pointing in the propagation direction of the wave, and φ_0 is the phase constant that sets the initial phase of the wave. Throughout this thesis, the optical momentum and the phase of electromagnetic waves, along with their manipulation, play a crucial role in the presented waveguide systems.

2.2. Nonlinear Optics

The field of nonlinear optics (NLO) deals with phenomena that arise when the optical properties of a material are altered by the presence of an electric field. These changes in the optical properties of a material (e.g., the refractive index) occur for both electrostatic fields (DC fields) as well as for alternating electric fields up to optical frequencies. On the one hand this enables to control light (e.g. its phase) by an electrical signal, which provides a link between electronics and photonics and is thereby of significant technological relevance[29]. On the other hand, nonlinear optical effects provide the ability of photons to influence the propagation of other photons, or even influence the propagating behaviour of themselves, when interacting with a nonlinear material. The related NLO effects include self-phase modulation and cross-phase modulation, both of which occur at optical frequencies[21]. In self-phase modulation, a photon modifies its own phase as it propagates through the nonlinear medium, while in cross-phase modulation, photons in one wave affect the phase of photons

in another co-propagating wave, enabling control over light by light[21]. These effects are utilized in a variety of applications such as ultrafast all-optical pulse shaping, optical communication, and the generation of new frequencies.

Typically, for ultrafast all-optical effects, only laser light is intense enough to induce nonlinear effects in most materials, because the nonlinear polarizability of most materials is comparatively small. Unless otherwise noted, the explanations in this section are based on [21].

The field of nonlinear optics is often considered to have begun with the discovery of second-harmonic generation by Franken et al. in 1961[29], shortly after the first demonstration of the laser in 1960. Nonlinear optical phenomena are termed "nonlinear" because they occur when the response of a material system to an applied optical field is not directly proportional to the field strength.

While in linear optics, the material response is characterized by the first-order dielectric susceptibility $\chi^{(1)}$, and thus determines the refractive index n of the material and governs light propagation, in nonlinear optics, the relationship between the material response and the electromagnetic field becomes more complex.

The polarization $\vec{P}$ of the material does no longer depend linearly on the electric field vector $\vec{E}$, but also has higher order dependencies. It can therefore be described as a power series of the following form[21].

$$\vec{P} = \varepsilon_0(\chi^{(1)}\vec{E} + \chi^{(2)}\vec{E}^2 + \chi^{(3)}\vec{E}^3 + \cdots) \tag{2.11}$$

While $\chi^{(1)}$ describes the linear component of the susceptibility, $\chi^{(2)}$ and $\chi^{(3)}$ are the second- and third- order nonlinear susceptibilities, respectively. The unit of the individual contributions to the susceptibility is given by $\left[\chi^{(n)}\right] = \mathrm{m}^{\mathrm{n}-1}/\mathrm{V}^{\mathrm{n}-1}$. Thus, while the components of $\chi^{(1)}$ are dimensionless, $\chi^{(2)}$ and $\chi^{(3)}$ have the units $\mathrm{m/V}$ and $\mathrm{m}^2/\mathrm{V}^2$, respectively. At high electric fields, these higher-order terms of the susceptibility can cause a variety of nonlinear optical (NLO) effects that do not occur in linear optics at moderate electric fields. In the following, the most important nonlinear optical effects used in this thesis will be briefly introduced.

3.2.3. The Pockels Effect

The Pockels effect (also known as the linear electro-optic effect) is a second-order nonlinear optical phenomenon ($\chi^{(2)}$), where the refractive index of a material changes linearly with an applied electric (DC) field. The effect generally occurs in materials with a nonzero second-order susceptibility. For symmetry reasons, $\chi^{(2)}$ as well as all even components of the susceptibility are zero in materials that possess inversion symmetry. Thus, the Pockels effect is typically found in non-centrosymmetric materials such as many crystals, that lack inversion symmetry[21].

Today, the Pockels effect has a wide range of applications in optical and photonic devices. For instance, Pockels cells are used to control the polarization state of light in laser systems for tasks such as light modulation, Q-switching, and pulse picking[21]. Additionally, in telecommunications, the Pockels effect is used for ultra-fast electro-optic modulators to encode information onto light beams by modulating their phase or amplitude[30]. Prominent examples of materials showing a Pockels effect (hereinafter termed as Pockels materials) include lithium niobate ($LiNbO_3$), potassium dihydrogen phosphate (KDP), and barium titanate ($BaTiO_3$), which are also optically anisotropic and thus show birefringence[21]. Birefringence often occurs along a specific axis of a crystal, typically termed the z-axis or c-axis, and as a result, such a crystal is referred to as uniaxial. This means the crystal has one optical axis where the refractive index differs from the other two perpendicular directions, leading to the separation of light into two distinct polarization components as it passes through the material. Consequently, the linear refraction properties can be represented by an index ellipsoid (see **Figure 2.1**).

If the electric field vector of an electromagnetic wave is oriented in z-direction, the light-matter interaction is governed by the extraordinary refractive index n_e. The ordinary refractive index n_o governs light matter interaction for an electric field vector in the x-y plane. This symmetry means, that for an electromagnetic wave propagating in z-direction, the index would be independent from the polarization state of that wave, and thus the polarization state would be maintained after the interaction. More generally, the polarization state of an electromagnetic wave is altered when the initial polarization includes both a z-component

and components in the x or y directions. This combination causes the wave components to experience a relative phase shift and thus a change in the polarization state of the wave.

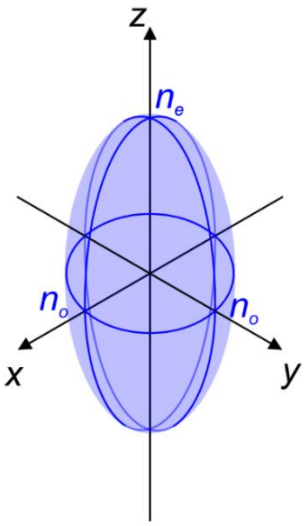

Figure 2.1*: The index ellipsoid of a uniaxial anisotropic optical material. The optical axis (c-axis) is oriented in z-direction. Adapted from* [31].

If such a birefringent crystal shown in Figure 1 also exhibits a Pockels effect, the index ellipsoid can be deformed by an external electric field, for instance via two electrodes attached to the crystal as used in Pockels cells. **Figure 2.2** shows cross-sections of an index ellipsoid of a Pockels material. Figures 2.2a and 2.2b show cross-sections of the index ellipsoid in absence of any external electric field. However, when an electric field is applied, this index ellipsoid is deformed. In this example, a field is applied along the z-axis. Importantly, the electric field affects not only n_e, but also n_o due to the tensor properties of $\chi^{(2)}$ (see Figure 2.2c,d).

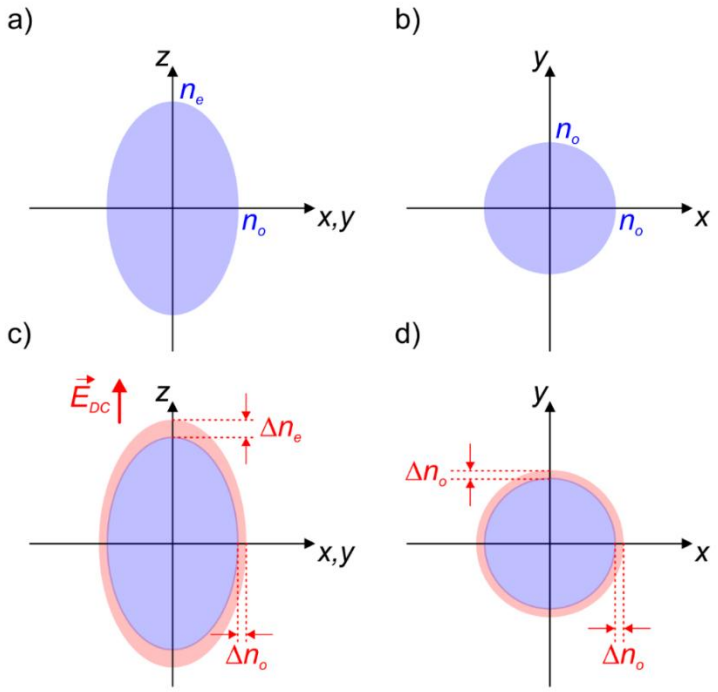

Figure 2.2: *The influence of an external electric (DC) field on the index ellipsoid of a Pockels material. a),b) 2D cross-sections of the index ellipsoid of a uniaxial Pockels material in absence of an external electric field; c),d) corresponding 2D cross-sections with an applied electric field along the optical axis.*

In the present case the changes of n_e and n_o can be expressed as follows:

$$\Delta n_e = \frac{1}{2} n_e^3 r_{33} E_{DC} \tag{2.12}$$

$$\Delta n_o = \frac{1}{2} n_o^3 r_{13} E_{DC} \tag{2.13}$$

Here, r_{33} and r_{13} are the Pockels coefficients of the material. A detailed derivation of this description and the corresponding nomenclature can be found in relevant textbooks. The unit of these coefficients is typically pm/V. For instance a lithium tantalate crystal, which will be used in the experiments shown in Chapter 4, has Pockels coefficients of $r_{33} = 30\ \mathrm{pm/V}$ and $r_{13} = 8.4\ \mathrm{pm/V}$. A more detailed derivation of equations 2.12 and 2.13, can be found in the literature.[21] Other NLO phenomena based on $\chi^{(2)}$ include sum and difference frequency generation, second harmonic generation, and optical parametric generation. In particular the latter has gained increasing importance in recent times, especially with regard to the generation of entangled photon pairs for quantum technologies.

3.2.4. The Optical Kerr Effect

In analogy, third-order effects refer to those, who are caused by the third-order nonlinear susceptibility $\chi^{(3)}$. One of these third-order effects is the intensity dependent refractive index. In contrast to the Pockels effect, here the refractive index change is no longer proportional to the electric field strength E, but to the intensity $I \propto E^2$. The index change can therefore be expressed as

$$\Delta n = n_2 I \tag{2.14}$$

The nonlinear refractive index n_2 can have a variety of physical origins. If the change in refractive index is driven by rapid processes such as electronic distortion, molecular vibrations, molecular redistribution, or molecular reorientation, it is referred to as the optical Kerr effect (OKE). Typically, these effects happen on an ultrafast timescale on the order of femtoseconds (fs) to picoseconds (ps), but are relatively small[21]. However, thermal expansion of the material can also result in an intensity dependent refractive index. For instance, when light heats a material via absorption, the material undergoes thermal expansion, leading to a change in its refractive index as a function of the density. These thermal effects typically occur over time scales ranging from microseconds (µs) to several milliseconds (ms)[21]. However, they can be orders of magnitude larger compared to the OKE. Thus, since the OKE typically requires high light intensities to become significant—usually on the order of hundreds of MW/cm² or more — pulsed lasers are commonly used to probe and harness the OKE.

Due to the varying time scales of the individual contributions (OKE, thermal expansion, etc.), laser parameters such as the pulse width and the repetition rate play an important role for the overall nonlinear response of the NLO material. In addition, thermal nonlinearity generally exhibits a negative n_2, because of the typically decreasing refractive index upon material expansion. In experiment, a negative n_2 causes the material to act as a self-defocusing element[21]. The OKE however often provides a positive n_2, meaning these contributions can counterbalance or even completely cancel each other out.

In analogy to the thermal nonlinearity, a material with a positive n_2 can act as a self-focussing element. This phenomenon of a self-(de)focussing is the basis of the commonly used z-scan method, which will be used in this thesis as well.

From the material perspective, the optical Kerr effect is observed in a wide range of materials, including gases, liquids, and solids. The magnitude of the Kerr effect, characterized by the nonlinear refractive index coefficient, thereby varies significantly among different materials. In the following, some of the most common materials that exhibit the optical Kerr effect and are widely used in practical applications will be introduced.

Among solids, glasses and crystals are the most commonly used materials showing an OKE. Silica glass, widely used in optical fibres, exhibits a noticeable OKE that is crucial for the operation of high-speed optical communication systems. The nonlinear refractive index of silica glass also enables the generation of optical solitons in fibre optics, which are key to optical data transmission over long distances without signal degradation. However, the OKE coefficients are typically low, e.g. for silica around $n_2 = 2.5 \cdot 10^{-20}\,\mathrm{m}^2/\mathrm{W}$.[32]

Liquids, particularly organic solvents like carbon disulfide (CS2), exhibit a particularly strong OKE.[33] Carbon disulfide is known for its relatively large nonlinear refractive index, making it a popular choice in nonlinear optical experiments, but has some disadvantages in application because of its toxicity.[34] Other liquids such as water, benzene, and nitrobenzene also display the OKE.[35–37] However, in general all liquids face a technological disadvantage, because their simultaneous implementation in optical systems together with solids e.g. in optical waveguide structures is typically challenging.

Also, thermal nonlinearities have been studies in a variety of material systems. Among others, there are recent reports concerning the thermal-induced nonlinear refractive index in materials including organic solvents,[38] nanoparticles,[39] metamaterials,[40] and 2D materials[41], which are promising for low threshold optical limiting, optical switching, signal processing, and sensing applications.

3.2.5. Two-Photon Absorption

The third nonlinear optical phenomenon that occurred during the experiments for this thesis is the effect of multi-photon absorption, particularly two-photon absorption (2PA). Two-photon absorption is a process where two photons are absorbed simultaneously by a material, exciting an electron from a lower energy state to a higher energy state. This process is significant in materials with a suitable bandgap, such as semiconductors and certain organic molecules. **Figure 2.3** shows the processes of fundamental absorption as well as 2PA in an exemplary energy diagram.

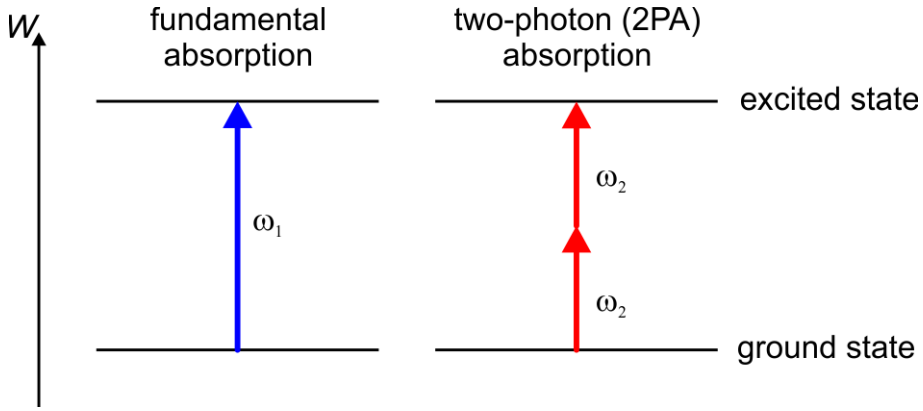

***Figure 2.3**: An exemplary energy diagram for the visualization of fundamental and two-photon absorption. Adapted from* [21].

In the case of fundamental absorption (case 1), the energy of a single (e.g. blue) photon with ω_1 must match the energy difference between the ground state and the excited state for being absorbed. In contrast, during two-photon absorption (case 2), the combined energy of both (e.g. red) photons with $\omega_2 = 1/2\omega_1$ must equal this energy difference. This process of two photons combining their energy to be absorbed depends on the intensity of the light with

$$\sigma = \sigma^{(2)} I, \tag{2.15}$$

where σ is the absorption cross-section of the material, and $\sigma^{(2)}$ is the two-photon absorption coefficient. Typically, two-photon (or even higher orders of nonlinear absorption) become significant at very high intensities of light, e.g. under pulsed laser illumination.

2.3. Optical Slab Waveguides

Optical slab waveguides consist of a transparent, high-refractive-index core, in which light is guided through total internal reflection at both boundaries of the waveguide core as well as an adjacent cladding layer. Thereby the refractive index of the core n_c has to be higher than the index of the cladding n_0. For the total internal reflection, the incidence angle of light at the boundaries of the waveguide has to be larger than the critical angle $\theta > \theta_c = \arcsin(n_0/n_c)$, which can be derived from Snell's law of refraction. If the two boundaries are in close proximity to each other and under certain phase matching conditions, the reflected electromagnetic waves can interfere constructively and form standing waves normal to the boundaries. In optical waveguides, these standing wave solutions are termed modes. The following sketch shows the basic geometry along with a refractive index profile of an optical slab waveguide.

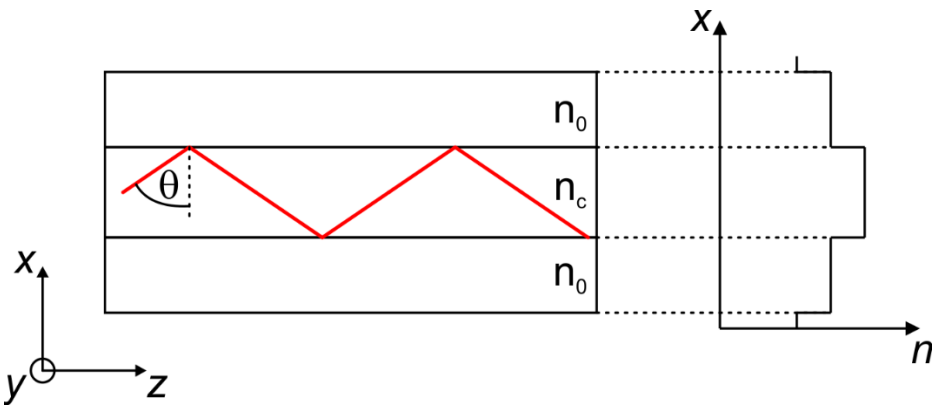

***Figure 2.4**: Sketch of an optical slab waveguide and corresponding refractive index profile.*

Considering plane-wave propagation as described by Equation 2.10 in z-direction in the exemplary slab waveguide (see **Figure 2.4**) and substituting the plane-wave approach into the Maxwell equation yields the following set of electromagnetic field components, with β being the propagation constant.

$$\frac{\partial E_z}{\partial y} + j\beta E_y = -j\omega\mu_0 H_x \tag{2.16}$$

$$-j\beta E_x - \frac{\partial E_z}{\partial x} = -j\omega\mu_0 H_y \tag{2.17}$$

$$\frac{\partial E_y}{\partial x} - \frac{\partial E_x}{\partial y} = -j\omega\mu_0 H_z \tag{2.18}$$

$$\frac{\partial H_y}{\partial y} + j\beta H_y = j\omega\varepsilon_0 n^2 E_x \tag{2.19}$$

$$-j\beta H_x - \frac{\partial H_z}{\partial x} = j\omega\varepsilon_0 n^2 E_y \tag{2.20}$$

$$\frac{\partial H_y}{\partial x} - \frac{\partial H_x}{\partial y} = j\omega\varepsilon_0 n^2 E_z \tag{2.21}$$

Using these electromagnetic field components, two independent types of modes can be obtained, which are termed TE (transversal electric) and TM (transversal magnetic) modes. A detailed derivation can be found in the literature. In both cases, a wave equation can be derived that has sinusoidal solutions inside the core of the waveguide and exponential decay characteristics in in the cladding. For instance in the case of TE modes, the electric field profile is shown in the following **Figure 2.5.**

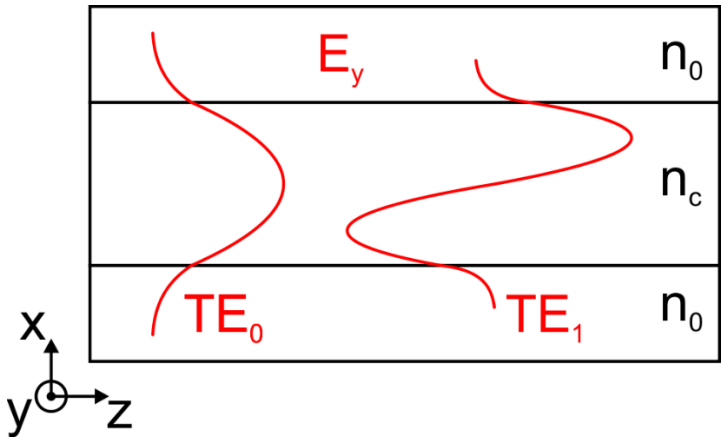

***Figure 2.5**: Sketch of electric field profiles of the fundamental TE_0 and the TE_1 mode.*

Mode solutions exist for different internal angles leading to distinct field profiles for each mode. These profiles differ particularly in the number of nodes (points where the field strength crosses zero, resulting in zero intensity at the node positions). In Figure 2.5, the fundamental mode is shown, which does not have nodes and is therefore called the TE_0 mode. The next higher-order mode has one node and is thus referred to as the TE_1 mode. Analogous mode solutions can be derived for the TM case. It will be shown later in this thesis, that the nodes with their intensity minimum can play a unique functional role in optical waveguides.

2.4. Fundamentals of Plasmonics

In the previous sections, only conditions were considered, in which no free charge carriers were involved in the interaction of light with matter. However, this assumption no longer holds when describing the interaction of light with conductive materials. For instance, in metals, an electromagnetic field can trigger collective oscillations of the free electrons, a phenomenon known as plasmons. Thus, plasmonics is the field of studying these oscillations and their interaction with electromagnetic waves targeting applications in bio-imaging, sensing, wave-front shaping, but also optical communication and quantum technologies.

Volume plasmons are collective charge carrier oscillations in electrically conductive materials, such as metals or semiconductors. The plasma model enables to describe the interaction of light with noble metals over a wide spectral range, often up to visible frequencies.[42] In the plasma model the free electrons in such materials are described as a free electron gas of high electron density, which oscillates in response to electromagnetic fields.[42,43] The motion of the electrons creates a density fluctuation within the electron gas. The quantum of this density fluctuation is called plasmon with an energy of $W_p = \hbar\sqrt{Ne^2/\varepsilon_0 m_e}$.[43] While the Coulomb force drives these oscillations, loss mechanisms such as charge carrier collisions dampen them.[42] Therefore, the oscillation of the electrons in the free electron gas can be described by the following differential equation.

$$m_e\ddot{\vec{x}} + m_e\gamma\dot{\vec{x}} = -e\vec{E} \tag{2.22}$$

with m_e as the mass of the electrons and $\gamma = 1/\tau_p$ being their collision frequency and τ_p the plasma relaxation time.

In the next step, by assuming a time-harmonic dependence of the electric field vector in the form $\vec{E} = \vec{E}_0 e^{-j\omega t}$, and considering the number density of electrons N, macroscopic polarization as well as material equations (see section 2.1), the complex dielectric function $\underline{\varepsilon}(\omega)$ of the free electron gas can derived[42].

$$\varepsilon(\omega) = 1 - \frac{\omega_p^2}{\omega^2 + j\gamma\omega} \tag{2.23}$$

The parameter $\omega_p = \sqrt{\frac{Ne^2}{\varepsilon_0 m_e}}$ is the plasma frequency of the free electron gas. The plasma frequency is defined as the frequency at which the real part of the dielectric function of the electron gas equals zero. For frequencies $\omega < \omega_p$ and neglectable losses ($\gamma \to 0$), the complex dielectric function of the electron gas can be simplified to

$$\varepsilon(\omega) = 1 - \frac{\omega_p^2}{\omega^2} \tag{2.24}$$

Together with the general formalism for the dispersion relation of transverse waves, the following dispersion relation $\omega(k)$ for volume plasmons can be derived.

$$\omega(k) = \sqrt{\omega_p^2 + k^2 c^2} \tag{2.25}$$

The plasma frequency determines whether light is predominantly reflected or transmitted through the metal. When the wave's frequency is lower than the plasma frequency, the metal reflects the electromagnetic radiation efficiently. Conversely, radiation with frequencies higher than the plasma frequency is transmitted through the metal.

Surface plasmon polaritons (SPPs) exist, in contrast to volume plasmons, at the interface between a metal and a dielectric. Unlike conventional waveguides, such as optical slab waveguides, SPPs require only a single material interface where the real part of the permittivities of the two materials have opposite signs[43]. This condition is typically fulfilled for a metal dielectric interface in the visible and near-infrared spectral region, where $Re(\varepsilon_m) < 0, \text{and } Re(\varepsilon_d) > 0$. The propagation of SPPs along the interface is governed by the dispersion relation, given by

$$k_{SPP} = k_0 \sqrt{\frac{\varepsilon_m \varepsilon_d}{\varepsilon_m + \varepsilon_d}}, \tag{2.26}$$

where k_{SPP} is the wave vector of the SPP, and k_0 is the wave vector in free space. Since $k_{SPP} > 0$, the direct excitation of SPPs via light from free-space is not possible, and a coupling mechanism, such as a prism or a grating coupler, is required. An important characteristic of surface plasmons is their finite propagation length, limited by Ohmic and radiative losses[43]. The damping is primarily caused by ε_m. The effective propagation length $L_{prop,SPP} = 1/2\text{Im}(k_{SPP})$.[43] In metals like gold and silver, the damping in the visible range is relatively low, making them preferred materials for plasmonic applications[42].

2.5. Optical Metasurfaces and Nanostructuring

Optical metasurfaces are artificial two-dimensional nanostructures consisting of structural elements of sub-wavelength size and spacing, which are commonly known as meta-atoms[44]. Depending on the chemical composition, size, shape, orientation, and spatial arrangement of these meta-atoms, metasurfaces can be designed to interact with light in a way that enables precise phase, amplitude, and polarization control of incident waves[42]. On the one hand, metasurfaces can therefore function as compact, lightweight, and sustainable substitutes for conventional optical elements.

On the other hand, this remarkable versatility allows for creating material properties, which do not appear among natural materials, such as near-zero permittivity, and negative refraction[45]. Consequently, optical metasurfaces have far-reaching potential for a wide set of applications, particularly in the fields of wavefront shaping[46], sensing[47], holography[48,49], but also energy harvesting[50], augmented and virtual reality[3,51,52], biomedical applications[53–55], and quantum technologies[56–58]. In the field of energy harvesting, metasurfaces offer the potential to significantly enhance the efficiency of photovoltaic devices, contributing to advancements in sustainable energy devices. In augmented and virtual reality, these metasurfaces play a crucial role in the development of lightweight and high-performance optics for immersive user experiences. Biomedical applications benefit from metasurfaces in imaging, and sensing, where their unique optical properties enhance resolution and sensitivity, impacting areas such as fluorescence microscopy and label-free sensing.

The fabrication of optical metasurfaces is often technologically challenging due to the nano-scale feature size and spacing of the meta-atoms. Thus, advanced top-down nanofabrication techniques such as electron beam lithography[59–62], or focused ion beam milling[60,63,64] are often required, which can be expensive, time-consuming and often lack scalability. In this scope, bottom-up methods have emerged as promising alternatives. The bottom-up fabrication of optical metasurfaces refers to a manufacturing approach in which the meta-atoms are assembled or grown from smaller building blocks. For instance, one method is colloidal self-assembly[65], where nanoparticles suspended in a liquid spontaneously organize into nanostructures according to some ordered or disordered pattern. Another common approach is the chemical synthesis of nanoparticles, such as wet chemical methods[66] or

electrochemical deposition[67], which enables the creation of metasurfaces by locally controlled growth of the meta-atoms. Among others, these bottom-up approaches particularly benefit from the scalability, ease of fabrication, and compatibility with other materials and processes in nanophotonics. However, challenges may persist in achieving uniformity and reproducibility over larger areas, as well as in gaining extensive control over the structural parameters of the nanostructure.

A promising strategy to meet these challenges is to introduce an external stimulus to gain dynamic control over the growth of the nanostructures. For instance, a photochemical process could serve as such a stimulus, where the growth of the meta-atoms depends on specific light-matter interaction properties, such as an energy transfer via the excitation of an optical resonance. By manipulating parameters such as the intensity, wavelength or polarization of light, precise control over the size, shape and assembly of the nanoparticles can be achieved. In this context, plasmon-mediated synthesis of metal nanoparticles stands out as one promising method. This approach utilizes the strong interaction efficiency of light with surface plasmons as an initiator for a chemical reaction, leading to the creation of noble metal nanoparticles and their assemblies[68–75]. Since this technique has entered the scientific stage[76], many researchers have studied and further developed this approach for applications such as Raman scattering[77–79]. However, the microscopic mechanisms behind these processes, especially their complex and dynamic interplay, are still not fully understood[75].

2.6. Engineered Disorder

For a long time, order and disorder have been considered strict opposites in optics, where order (e.g. the order of structural elements building a nanostructure) is considered the goal state. Disorder, on the other hand was some undesired effect caused for instance from fabrication imperfections. Nowadays, however, disorder is no longer seen as inherently undesirable. In fact, a state that lies between perfect order and complete randomness, which is called engineered disorder, can even have advantages over a perfectly ordered structure.[80]

One example of this is the use of nanostructures to improve the efficiency of light coupling into solar cells. The nanostructure (or metasurface) is designed to scatter or diffract the light at an angle within the solar cell so that it undergoes total internal reflection, thereby

increasing the probability of light absorption. However, potential drawbacks of using ordered structures are that the light is diffracted into a specific lateral direction, and diffraction artifacts can arise, potentially impairing the functionality of the metasurface. This is where a structure with engineered disorder can have advantages. By using engineered disorder, it is possible not only to achieve nearly isotropic scattering of light in all lateral directions but also to eliminate diffraction artifacts. Recent reports in the literature have already shown promising results in this regard.[81,82]

To investigate the properties of a disorder-engineered structure, the analysis of microscopic images in reciprocal space (k-space) can be particularly useful. In addition to the widely used two-dimensional Fourier transformation, which is also used for analysing surface morphologies in general, there are metrics specifically developed for disorder-engineered structures. One such metric is the so-called structure factor $S(k)$, which only takes into account the mass centers of individual structural elements, ignoring other properties including their size and shape.[80] In cases where the packing density, such as in an arrangement of nanoparticles, becomes very high and it becomes difficult to determine the mass centers of individual particles, the spectral density $\chi_s(k)$ is another common metric.[83]

The structure factor $S(k)$ and the spectral density $\chi_s(k)$ can be derived as follows[80,83]

$$S(k) = \frac{1}{N}|\mathcal{F}(M_0)|^2, \tag{2.27}$$

where N is the number of particles, M_0 is a binary matrix representing the centre location of particles, and $\mathcal{F}$ is the two-dimensional Fourier transform.

In addition, the spectral density $\chi_s(k)$ can generally be expressed as[84]:

$$\chi_s(k) = \frac{1}{V}\langle\left|\Im^{(i)}(k)\right|^2\rangle, \tag{2.28}$$

where *V* is the volume of the observation box, and $\Im^{(i)}$ is the phase indicator function, which e.g. distinguishes the two phases of a monodisperse particle structure (particle material and spacing material).

In the past decade, one class of engineered-disorder, known as disordered hyperuniformity (DHU), has gained particular attention. Since the first theoretical literature report of DHU back in 2003[83], DHU has developed from a theoretical curiosity to a technologically relevant phenomenon in a variety of material systems. Until today, DHU has been shown both in natural (e.g. the distribution of galaxies in the universe) and artificial systems[80,85]. In order to identify hyperuniformity, the abovementioned metrics have to fulfil the following in the case of the structure factor.[83]

$$\lim_{k \to 0} S(k) = 0 \tag{2.29}$$

The strongest form of DHU, stealthy DHU, where the structure factor is even zero for $0 < k \leq K$. The same rule applies for the case of the spectral density.

In application, the isotropic nature of DHU structures has enabled the first successful implementation of isotropic photonic band gaps (PBGs) in a photonic crystal, which shows DHU.[86,87] Moreover, DHU has gained significant attention in various optical applications, including light management in solar cells[88], solid-state lighting[89], surface-enhanced Raman spectroscopy (SERS)[90], and customized light scatterers[91].

However, and despite their unique properties, the widespread application of DHU structures remains hindered by the complexity of their design and challenging fabrication. Although DHU structures are well-suited for bottom-up fabrication methods due to their high tolerance for structural defects[92], top-down and hybrid techniques have remained the state-of-the-art fabrication methods.[93,94]

2.7. Swelling Effect of Soft Matter

Swelling in soft matter, such as polymers, gels, and elastomers, is a phenomenon where a solvent can be incorporated into the host material, causing them to expand in volume.[95] This process is particularly relevant in a wide range of scientific and industrial applications, including biotechnology, microfluidics, and soft robotics. One example for such a host material that shows swelling when it gets into contact with certain solvents is polydimethylsiloxane (PDMS), a widely used silicone based elastomer. PDMS is valued for its flexibility, biocompatibility, and ease of fabrication, making it a popular choice e.g. in stretchable electronics for biomedical applications. When exposed to certain solvents or

environmental conditions, PDMS can soak up the solvent similar to a sponge. A process known as swelling. This swelling leads to an increase in volume of the composite material. The swelling behavior of PDMS is influenced by several factors, including the chemical compatibility of the solvent with the polymer, the cross-linking density of the material, and the environmental conditions such as temperature and pressure.

Chapter 3

Experimental Methods

3.1. Fabrication Methods

3.1.1. Plasmonic Waveguide Structures

For the preparation of the SPP waveguide samples, sapphire substrates (Al_2O_3) with a thickness of 500 μm are used. An ultrathin chromium film ($t_{Cr} = 1.5$ nm) was first deposited on the sapphire substrate to serve as an adhesion layer, followed by a silver film, both applied via thermal evaporation. The deposition rate is 0.2 Å/s and 0.5 Å/s for chromium and silver, respectively. For silver films thinner than 30 nm, the deposition rate is reduced to 0.1 - 0.2 Å/s to minimize surface roughness. In general, the thickness of the silver film covers a range of several tens of nanometers, depending on the particular experimental ($t_{Ag} = 20 - 60$ nm). Subsequently, a 15 nm thick poly(methyl methacrylate) (PMMA) film was spin-coated on top of the silver. The solvent was evaporated in a vacuum chamber for 10 minutes. The PMMA layer acts as a buffer, facilitating nanoparticle formation on the PMMA surface rather than continuous silver film growth during the process. All film thicknesses were measured using a profilometer (Dektak 3ST). Silver nanoparticles (AgNPs) were then grown from solution using the electroless deposition (ELD) technique. The use of this ELD method has undergone quite extensive development in the research conducted at the LGOE, which is briefly describe below.

Silver exhibits strong plasmonic interaction properties and the highest electrical and thermal conductivity among all metals[42]. Due to the distinctive optical properties of AgNPs, the work in this field has primarily focused on exploring methods to control the morphology of silver nanoparticles and their 2D assemblies, aiming to enlarge their potential for a diverse range of applications. At first, in 2014 the research group at the LGOE has studied the impact of moisture and white light illumination on the morphology of AgNP assemblies and their adhesion to a polymer surface[96].

The AgNPs were fabricated using thermal evaporation of silver. A dependency between the exposure dose and the coalescence of AgNPs on PDMS was discovered. Based on these experiences, our group has started to incorporate such AgNP assemblies in more complex stack geometries. For instance, positioning an array of silver nanoparticles (AgNPs) in close proximity to a planar silver film. This promotes the coupling of different plasmonic modes to form gap plasmons, which can be used for highly efficient absorbers[97]. AgNP assemblies can also be used for enhancing the efficiency of organic solar cells, when used as semi-transparent electrode material[98,99].

Due to these unique properties, in recent years the Chair of Large Area Optoelectronics (LGOE) has conducted research on developing innovative methods for fabricating silver nanoparticles and metasurfaces. The related developments will be summarized in the following. Since 2017, the research in this field has then been focused on the light-controlled fabrication of AgNP based metasurfaces with tailored optical functionalities. These functionalities are governed by a distinct type of pattern known as engineered disorder (see chapter 2.7). Instead of thermal evaporation of silver, the group at the LGOE started to conduct experiments based on the wet chemical synthesis of AgNPs. The preparation of the ELD solution for plasmon-induced growth of AgNPs is based on the mirror reaction described by Saito et al.[100] This reaction involves the reduction of silver ions by glucose in a mixture containing ammonia, silver nitrate, and aqueous glucose.

In first experiments, a PDMS substrate locally exposed to UV light was brought into contact with the ELD solution. Thereby, AgNPs grew at room temperature in the illuminated areas only. Further investigations have revealed that in addition to surface pretreatments, the morphology can also be controlled by light illumination of the solution during the growth of the AgNPs. The same principle also applies for monochromatic light. Casting the ELD solution on a non-treated glass substrate and illuminating a certain substrate position with a visible laser, a deposition of AgNPs in this very spot only was observed[101]. The reason behind this phenomenon is that the adhesion of existing AgNPs can be increased by light illumination[96] and that such an increase of adhesion energetically favors further growth of particles inside the solution[102]. Combining these effects allows for establishing a light-sensitive deposition of AgNPs. Within the illuminated area, the AgNPs distribution is not entirely random.

In fact, many parameters of the illumination conditions could be found in the reciprocal space, including wavelength, incident angle, and polarization. This phenomenon could be explained theoretically assuming that the AgNPs are placed at local intensity hotspots with high accuracy below 20 nm[101]. This assumption has been experimentally proven by demonstrating the growth of AgNPs on a thin film optical waveguide, where the illumination was realized by the evanescent field of a propagating photonic waveguide mode[103]. This hybrid photonic-plasmonic device shows an enhanced interaction between the AgNPs and the waveguide mode, which can be applied for efficient waveguide (de-)coupling.

3.1.2. Photonic Waveguide Structures

A 4-inch lithium tantalate ($LiTaO_3$) wafer with a thickness of 500 µm was pretreated using excimer irradiation (λ = 172 nm) at a dose of approximately 25 J/m². The purpose of this treatment was to increase the wafer's surface energy, thereby improving the wetting properties of the polymer solution. Following this pretreatment, the wafer was coated with a 1 µm-thick layer of Ormocore using spin coating. The coating solution consisted of propylene glycol methyl ether acetate (PGMEA) and Ormocore. Afterward, the coated wafer underwent a vacuum treatment ($p \approx 1 \times 10^{-4}$ mbar for 10 minutes) before being cut into two halves. Each half was then UV-cured separately. The first half received a full UV cure (λ = 385 nm) with a dose of approximately 2 J/m², while the second half was cured with only 10% of this dose. The reduced UV dose was intended to increase the viscosity, thereby reducing dewetting of the Ormocore layer. A silver grating was then transfer-printed onto the surface of the fully cured half. To facilitate this, standard sinusoidal gratings with periods of Λ = 278 nm and 555 nm were replicated in polydimethylsiloxane (PDMS). The PDMS replica was subsequently coated with silver (Ag) using a deposition angle of 50 degrees (thermal evaporation). The gratings with a period of Λ = 278 nm had an amplitude of 40 nm. To avoid the formation of a continuous silver film, the film thickness was limited to 30 nm. This silver film was then successfully transferred onto the wafer. Finally, the two halves of the wafer were laminated together using a laboratory press (p = 50 bar) and simultaneously UV-cured (λ = 365 nm) with a dose of approximately 2 J/m². This process resulted in the formation of a symmetric stack with the structure: $LiTaO_3$ / Ormocore / grating / Ormocore / $LiTaO_3$.

3.1.3. Nonlinear PDMS composite samples

A two-component silicone elastomer (Mavom Sylgard 184), consisting of a precursor and a curing agent, was used to prepare the PDMS films. The components were mixed in a 10:1 ratio and manually stirred. Annealing was performed in a vacuum chamber for 30 minutes. The optically transparent mixture was then poured into a Teflon mold (30 mm x 30 mm) to the desired film thickness. A glass slide placed at the bottom of the mold ensured a smooth interface, reducing light scattering during optical experiments. The PDMS was cured at 80°C for 60 minutes. After curing, the film was cut into four equal-sized samples. One sample was used as a reference for optical measurements, while the other three were reserved for further processing. To incorporate organic solvents into the PDMS matrix, the samples were immersed in three different solvents: nitrobenzene (NB), 2,6-lutidine (LT), and toluene (TL). After a swelling period of 3 hours, the samples were removed from the solvent baths, and the degree of swelling was quantified by measuring the weight change before and after immersion. For optical measurements, the swollen samples were placed between two quartz slides using a Teflon frame for mechanical stability.

3.2. Characterization Methods

3.2.1. The Z-scan technique

Since its first report in 1989, the z-scan technique is a commonly used experimental method in nonlinear optics for the characterization of third-order nonlinear optical properties of transparent materials.[104,105] One of the advantages of this method is its high sensitivity, which allows it to detect even small nonlinearities. In particular, self-(de)focusing described by the nonlinear refractive index n_2 as well as multi-photon absorption (or saturable absorption) described by the nonlinear absorption coefficient β can be measured.[21] The basic principle of the z-scan technique is the translation of a sample along the propagation axis of a laser beam (z-axis). The laser beam is focused using a lens, which leads to a variable illumination intensity of the sample depending on the distance to the focal point. As the sample moves along the z-axis, the intensity of light transmitted through the sample is measured as a function of the position z.

Figure 3.1 shows a sketch of the optical setup, which was used in the experiments for this thesis. As laser source, a solid-state pulsed laser (frequency-doubled Nd:YAG) with a pulse width of around 330 ps and a wavelength of 532 nm was used. The repetition rate RR can be set from single shot up to 1 kHz. The manufacturer of the laser system is Teem Photonics. The initial laser power and the beam diameter were adjusted using a variable neutral density filter (VF_1) and an iris (I_1) with variable diameter. The laser power is referenced using a beam splitter cube (BS) and photodiode-based optical power meter D_1. The main beam then passes through a focussing lens (L_2, $f = 20$ cm) and is thereby focused to a fixed position Z_0. The transmitted light was collected using another focussing lens (L_3, $f = 15$ cm) and then detected by photodetector D_2. By measuring the transmitted power while moving the sample along the z-axis, one can generally extract both n_2 and β.

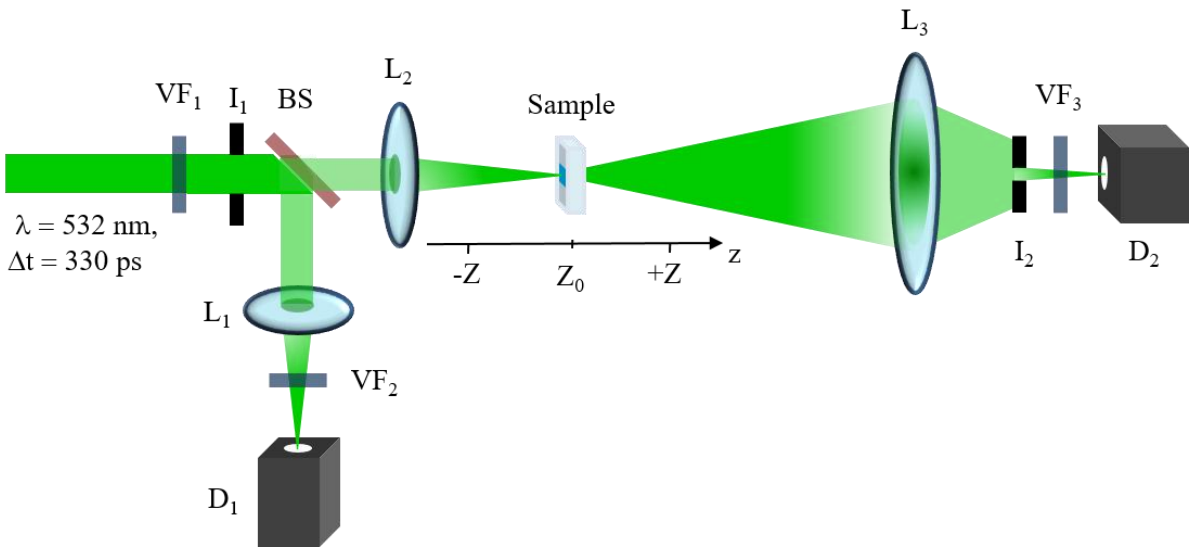

***Figure 3.1**: A sketch of the z-scan setup used for the experiments shown in chapter 6.*

The Z-scan experiment is typically performed in two distinct configurations: the closed-aperture (CA) and open-aperture (OA) configuration. Each of the configurations provide insight into different aspects of the material's nonlinear behaviour. In the CA configuration, an iris (or aperture) is placed in front of the detector enabling only the central part of the transmitted beam to pass through. In the CA configuration, the setup is sensitive to changes in the phase of the light, which occur due to the nonlinear refractive index n_2 of the material. As the sample moves through the focus of the laser beam, the beam may experience self-focusing or self-defocusing effects due to the changing illumination intensity.

These effects can influence the divergence of the laser beam, which is detected as variations in the intensity of light passing through the aperture. Moving the sample from position $-Z$ to Z, the resulting transmittance curve typically exhibits a characteristic peak followed by a valley (or vice versa), depending on the sign of the nonlinear refractive index (see **Figure 3.2**). In the OA configuration, on the other hand, the aperture is entirely opened so that all transmitted light is collected by the detector. This configuration is primarily used to measure the nonlinear absorption coefficient (β) of the material. Nonlinear absorption processes, such as two-photon absorption or saturable absorption, manifest as changes in the transmittance of the sample as it passes through the focal region of the beam. For instance, in the case of two-photon absorption, the Z-scan curve typically shows a dip in transmittance when the sample reaches position Z_0, while saturable absorption would result in a peak. Because the CA scan is influenced by nonlinear refraction and absoption effects, the relation CA/OA has to be considered in order to determine n_2.

In the setup used for this thesis, the additional variable iris I_2 enables to perform both open-aperture (OA) as well as closed-aperture (CA) Z-scan experiments without changes in the beam path or adjustments of other optical components. Furthermore, the linear transmittance of the iris I_2 was set to $S = 1$ and $S = 0.4$ for OA and CA Z-scan measurements, respectively. Photodiode power sensors (S151C, Thorlabs) were used as photodetectors. The translation of the sample along the z-axis was done by a linear stage and a stepper motor. By fitting the experimental data to appropriate theoretical models, the nonlinear absorption coefficient (β) can be accurately determined.

The nonlinear optical indices of the samples were determined by fitting the experimental data with the theoretical model. By considering a Gaussian beam excitation in the low irradiance limit (small beam distortion) the normalized transmittance in a CA Z-scan measurement for thick samples (sample thickness $L > z_R$) is given by[105]

$$T(z) = 1 + \Delta\emptyset F(x, l), \tag{3.1}$$

$$\text{where } F(x, l) = \frac{1}{4}\ln\left(\frac{\left[\left(x+\frac{l}{2}\right)^2+1\right]\left[\left(x-\frac{l}{2}\right)^2+9\right]}{\left[\left(x-\frac{l}{2}\right)^2+1\right]\left[\left(x+\frac{l}{2}\right)^2+9\right]}\right). \tag{3.2}$$

Here, $x = \frac{z}{z_R}$ and $l = \frac{L}{z_R}$, where L is the sample thickness, $z_R (= \frac{\pi\omega_0^2}{\lambda})$ is the Rayleigh length with ω_0 and λ are the beam waist radius at the focal plane focus and the vacuum wavelength, respectively. $\Delta\emptyset = n_2 k_0 I_0 L_{eff}$ is the on-axis phase shift caused by nonlinear refraction. Here, n_2 is the third order nonlinear refractive index, $k_0 = \frac{2\pi}{\lambda}$ the wave vector, I_0 the irradiance, and $L_{eff} = \frac{1-\exp(-\alpha L)}{\alpha}$ is the effective path length with α being the absorption coefficient. If the sample is sufficiently thin ($L \leq z_R$), the transmittance converges to the thin sample approximation to which the experimental data are fitted:

$$T(z) = 1 + \frac{4x\Delta\emptyset}{(x^2+1)(x^2+9)} \tag{3.3}$$

In practice, samples with nonlinear optical properties yield the following typical characteristics in the Z-scan measurements. Figure 3.2 show typical Z-scan curves for a sample

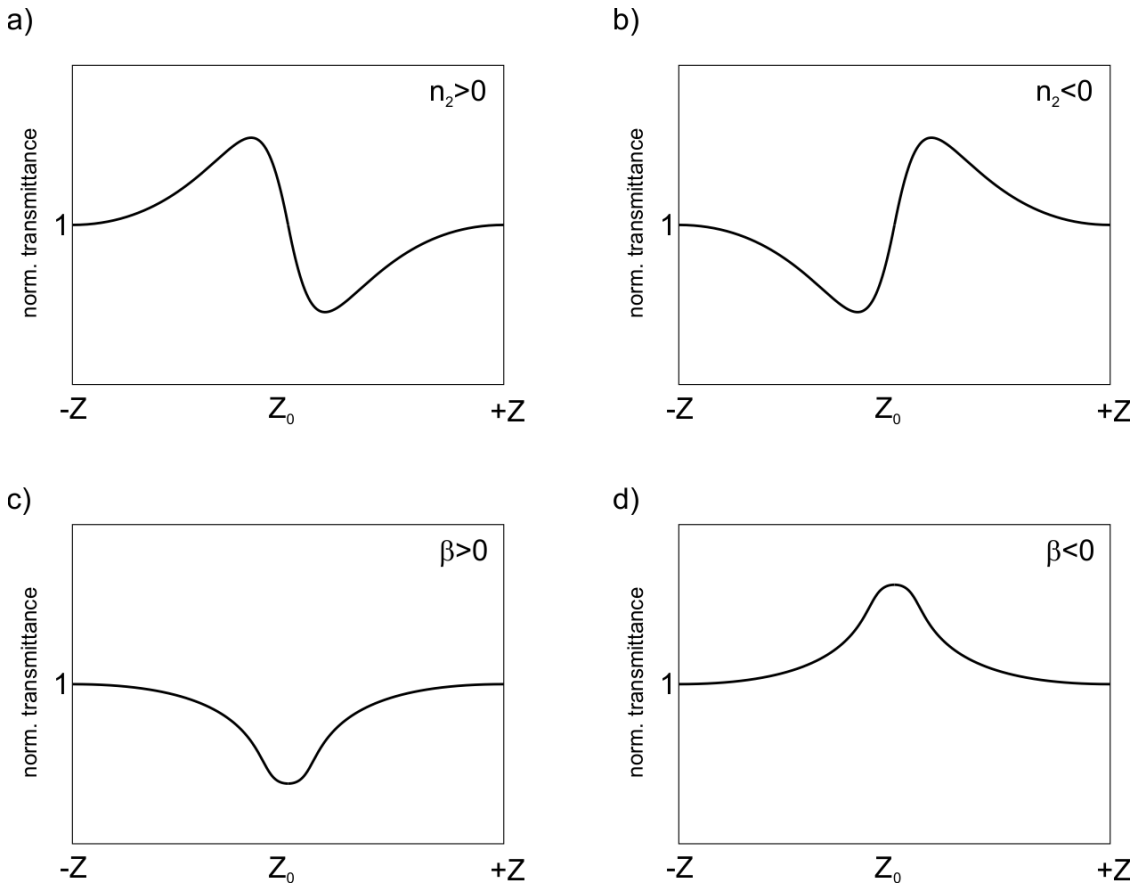

***Figure 3.2**. Typical results from Z-scan measurements on samples with different nonlinear optical properties. a),b) typical CA Z-scan profiles for samples that show self-focussing ($n_2 > 0$) and self-defocussing ($n_2 < 0$), respectively; c),d) typical OA Z-scan profiles for samples that show multi-photon absorption (e.g. 2PA, $\beta > 0$) and saturable absorption ($\beta < 0$).*

Further, we derived the real part of the third-order nonlinear susceptibility $\mathrm{Re}\,(\chi^{(3)})$ by the following equation[21]:

$$\mathrm{Re}\,(\chi^{(3)}) = \frac{4}{3} n_0^2 \varepsilon_0 c_0 n_2 \tag{3.4}$$

Here, n_0 is the linear refractive index, ε_0 is the electric field constant, and c_0 is the vacuum speed of light. For the composite materials, a weighted mean of the refractive index was calculated according to the different mass ratios of each composite material (effective medium approximation).

3.2.2. The Attenuated Total Reflection (ATR) technique

The Attenuated Total Reflection (ATR) method is a technique used to analyze the optical properties of thin films and surfaces, which is not only applicable in plasmonics but also commonly used in infrared spectroscopy. In an ATR setup, a light beam propagates through a prism with high refractive index, where it undergoes total internal reflection at the interface between the prism and the adjacent medium (e.g. the sample). The total internal refelction creates an evanescent wave propagating along this interface. The penetration depth into the adjacent medium is only a few hundred nanometres or even less. Under certain conditions, the evanescent wave can couple to surface plasmons, e.g. if a thin metal film is coated on the prism. As explained in section 2.3, surface plasmon polaritons have a higher momentum for a given frequency, which renders them difficult to be excited using photons. Since surface plasmons are surface waves, which propagate along the metal-dielectric interface, it is the lateral momentum of an incident light wave, which has to match the momentum of the surface plasmons. However, a common method to compensate this mismatch in lateral momentum is based on providing additional momentum for the photons using a prism of high refractive index. The prism increases the momentum of the photons by a factor corresponding to the refractive index of the prism. By varying the propagation angle θ, the lateral momentum of the photons can be adjusted according to $k_{\parallel} = n_p k_0 \sin\theta$., where n_p is the refractive index of the prism, k_0 is the vacuum momentum of the incident photons. In addition to glass ($n_g = 1.46$), a typical prism material is sapphire, due to its high refractive index ($n_g = 1.76$). In the Kretschmann-Raether configuration, a thin metal film (typically gold

or silver) is then coated on the prism. A light beam with variable propagation angle is the adjusted to show total internal reflection at the prism-metal interface.

Given the low thickness of the metal film (in the order of a few tens of nanometers), the field profile of the evanescent wave can overlap with the SPP field profile, which enables coupling with the surface plasmons at the upper metal-dielectric interface under momentum matching conditions. Momentum matching is fulfilled for

$$k_{\parallel} = n_p k_0 \sin\theta = \frac{\omega}{c_0}\sqrt{\frac{\varepsilon_m \varepsilon_d}{\varepsilon_m + \varepsilon_d}} = k_{SPP}. \tag{3.5}$$

For practical reasons, here the prisms are not directly coated. Instead, substrates made from the same material (e.g. sapphire) are coated with one or multiple thin films. The samples, which are described in Section 3.1 are then placed on top of the prism. An index-matching liquid between the prism and the sample is used to reduce or minimize partial reflections at the prism-sample interface.

An optical setup for the excitation of SPPs using the Kretschmann configuration was implemented. The beam from a laser diode is first collimated using a lens and then mounted in a goniometer setup (see **Figure 3.3**).

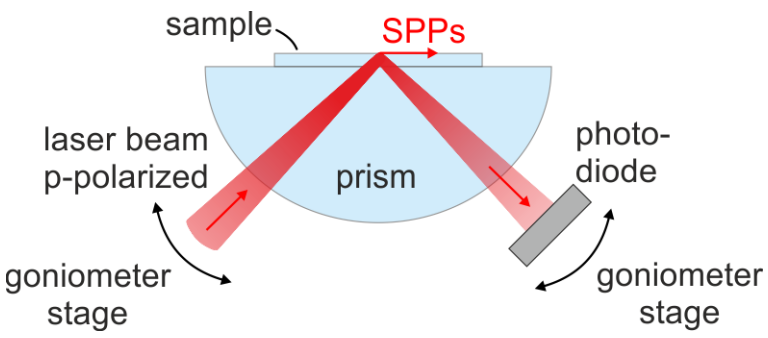

***Figure 3.3**: Sketch of the Kretschmann configuration used for the excitation of SPPs.*

A semi-cylindrical sapphire prism is placed at the rotation centre of the goniometer. A photodetector is positioned on the reflection arm to capture the reflected power. The laser beam is p-polarized using a polarization filter. Additionally, a variable neutral density filter allows for continuous adjustment of the laser power. Resonant excitation conditions can be recognized by a dip in the reflectance over the incident angle, which represents the energy transfer from photons to plasmons. The position of this dip in reflectance of course at a given frequency depends on the refractive indices and thicknesses of all involved layers.[43]

3.2.3. *Michelson Interferometer*

For conducting the experiments discussed in chapter 5, a precise and continuous monitoring of the refractive index of a test analyte is necessary. A very common and highly sensitive method for detecting changes in the refractive index of transparent media is interferometry. There are various implementations of interferometers, with the Mach-Zehnder and Michelson interferometers being among the most commonly used. The Michelson interferometer, in particular, offers the advantage of interacting with the sample medium twice, resulting in a longer interaction length with the sample material.

Therefore in this thesis, a Michelson interferometer, is used to monitor changes in the refractive index of the probe solution during the ATR measurements. **Figure 3.4** shows a sketch of the experimental setup of the Michelson interferometer.

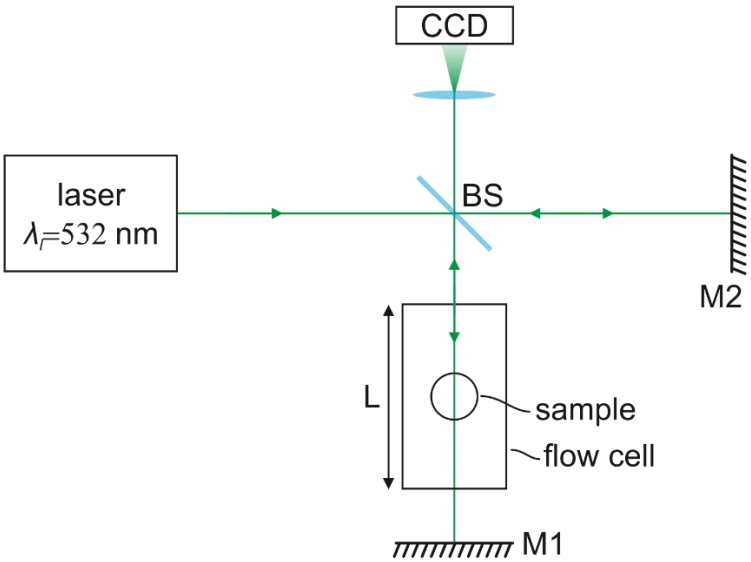

***Figure 3.4**: Michelson interferometer containing a laser diode with a wavelength of 532 nm, a 50:50 beam splitter cube (BS), two silver mirrors (M1, M2) and a CCD camera to record the resulting interferograms.*

For the interferometric measurements, a solid-state laser ($\lambda = 532$ nm) is used as a light source for the interferometer. One beam of the Michelson interferometer (hereinafter referred to as signal beam) penetrates the liquid inside the flow cell with an interaction length of $2\mathrm{L} = 16$ cm (two times the length L of the flow cell). The other arm of the interferometer

serves as reference arm, in which the refractive index is held constant. The interferogram at the output of the interferometer is detected using a CCD sensor.

If the refractive index of the analyte changes, a phase shift $\Delta\varphi_l = 2\pi \cdot \Delta n \cdot \frac{2L}{\lambda_l}$ is generated in the signal beam, where $\Delta\varphi_l$ is the induced phase shift of the signal beam, and Δn is the change in the refractive index of the analyte. This phase shift then leads to a change in the interference conditions at the beam splitter, which can be analysed using the recorded interferogram. A typical interferogram is recorded by the CCD camera is shown in the following **Figure 3.5a.**

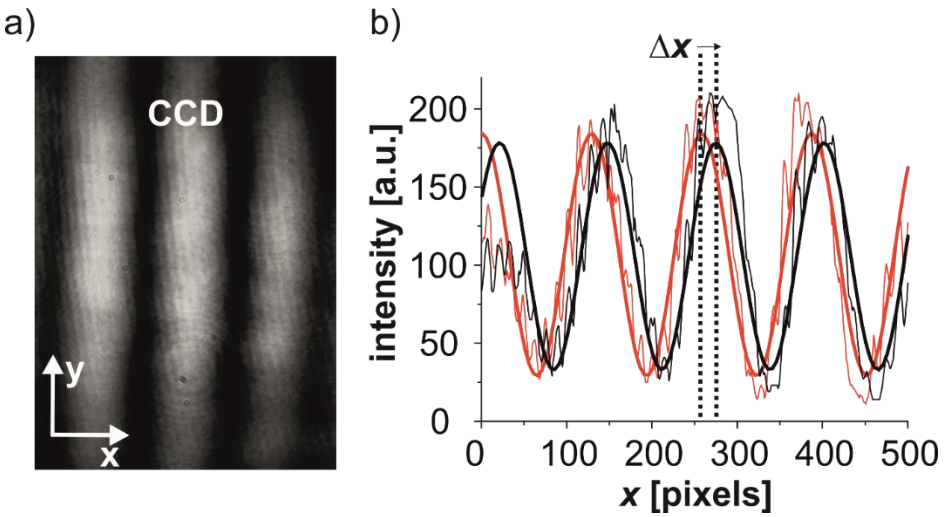

***Figure 3.5**: The detection of phase shifts in the Michelson interferometer. a) a fraction of an interferogram detected by the CCD camera; b) sinusoidal fit to the measured intensity profiles of two interferograms after a phase shift in the signal arm.*

As shown in Figure 3.5b, a phase shift of $\pm\Delta\varphi_l$ in the signal arm results in a shift of the interference fringes in the interferogram. In the present case, the interferogram has been adjusted with respect to the CCD sensor, so that the interference fringes shift in the $\pm x$-direction (see Figure 3.5b). The distance of two intensity maxima in the interference pattern corresponds to a phase shift of $\Delta\varphi_l = 2\pi$. For further analysis, a phase difference must now be assigned a pixel distance in the CCD image. The distance between two maxima in the interferogram cover around 128 pixels in the image. Thus, a phase shift translates to the CCD images as $\Delta x \approx \frac{128\ \text{pixels}}{2\pi}\Delta\varphi_l$. To monitor a refractive index change of the analyte, for each CCD image recorded while changing the refractive index of the analyte, a horizontal cut is

performed. The resulting intensity data is fitted with a sinusoidal function (see Figure 3.5b). The phase change compared to the previous CCD image is then determined. The sum of all phase changes then yields the overall change of the refractive index of the analyte during the measurement.

3.2.4. Laser Beam Divergence Characterization

Since the divergence of the laser plays an important role in the interpretation of the measurement results in chapter 5 (momentum width of the structure rings and wave rings), it is necessary to measure the beam divergence. Therefore, the beam diameter has to be measured both directly after the output aperture of the laser and at a position in some distance. Since the divergence is quite small, the distance to the laser has to be quite large in order to measure a significant change in the beam diameter.

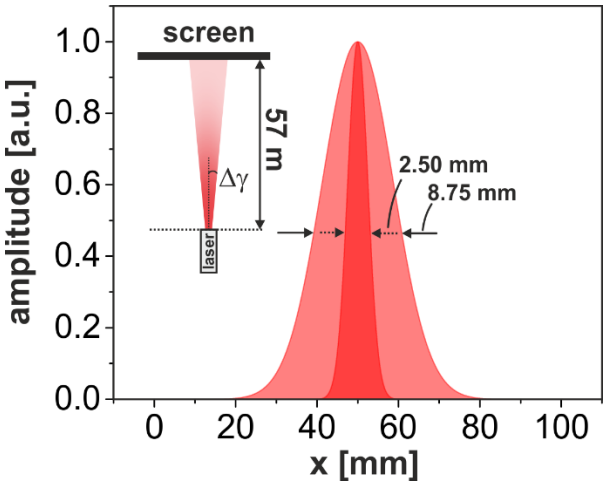

***Figure 3.6**: Principle of measuring the divergence of the laser used in the experiments discussed in Chapter 5.*

Here, a distance of approximately 57 meters from the laser was used, due to practical considerations during the measurement. As boundaries of the beam, the full width at half maximum is used to determine the beam diameter. The measurement principle is shown in the following **Figure 3.6**. The beam diameters are 2.5 mm and 8.75 mm for the two cases. The corresponding beam divergence (half-opening angle) is $\Delta\gamma = 5.5 \cdot 10^{-5}$ rad.

Chapter 4

Sensitive Photonic Waveguide Structures

4.1. TE1-modes as Platform for Sensitive Photonic Waveguides

(The following section is based on journal paper 9 of the publication list.)

The first concept to be discussed in this thesis is the use of a slab waveguide that has a refractive index profile, which is mirror-symmetric with respect to the growth direction. An optical grating, which can be used for coupling light into (and out of) the waveguide, is placed in the symmetry plane of that waveguide, which is then called waveguide grating.

In the past, it has been demonstrated that placing lossy (e.g. scattering or absorbing) layers or structures at the position of the intensity minima of TE modes, which correspond to the nodes of the mode, can be utilized to significantly enhance the propagation length of light inside optical waveguides.[106] In addition, it has been shown that such waveguide gratings offer high sensitivity, as even a slight shift in the node position (e.g. caused by a change in the refractive index of one of the waveguide materials) can result in a considerable change in propagation length.[107] This sensitivity makes node modes promising where precise control over wave propagation is critical, such as in optical sensing or modulation.

In this section, a theoretical analysis of node modes in waveguide gratings will be conducted. For this purpose, simulations using an RCWA (Rigorous Coupled-Wave Analysis) simulation tool, which has been developed at the LGOE and used e.g. to analyse distributed feedback lasers, will be performed.[108–111] In particular, the differences between a node mode (in this case a TE_1 mode) and a mode without nodes, e.g. the fundamental TE_0 mode, will be shown. In addition, the implications of these differences for utilizing node modes in highly sensitive optical applications will be discussed. **Figure 4.1** shows the model of such a waveguide grating used in the RCWA simulations. The waveguide grating consists of an infinitely extended rectangular optical grating with a period Λ, the refractive indices of the two grating materials n_{g1} and n_{g2}, and the duty cycle D.

Furthermore, the grating is sandwiched between two dielectric layers with thicknesses t_{d1} and t_{d2}, as well as refractive indices n_{d1} and n_{d2}. The simulations in this section assume TE polarized plane-wave incidence. This model provides a framework to investigate the effects of refractive index changes on the propagation behaviour, which may enable to maximize sensitivity. In addition to the geometric parameters of the waveguide grating, it is necessary to define symmetry measures for both the refractive indices (RI symmetry) and layer thicknesses (geometric symmetry). Both of these symmetry parameters can thus influence the optical symmetry of the waveguide grating. Therefore, the following symmetry parameters χ_n and χ_{gp} are defined as

$$\chi_n = \frac{n_{d1}}{n_{d2}} \qquad \text{and} \qquad \chi_{gp} = 1 - \frac{|t_{d1} - t_{d2}|}{t_{d1} + t_{d2}}.$$

Thus, the two symmetry parameters represent both refractive index profile "n" and the grating position "gp". A situation of $\chi_n = 1.0$ and $\chi_{gp} = 1.0$ thus indicates perfect symmetry.

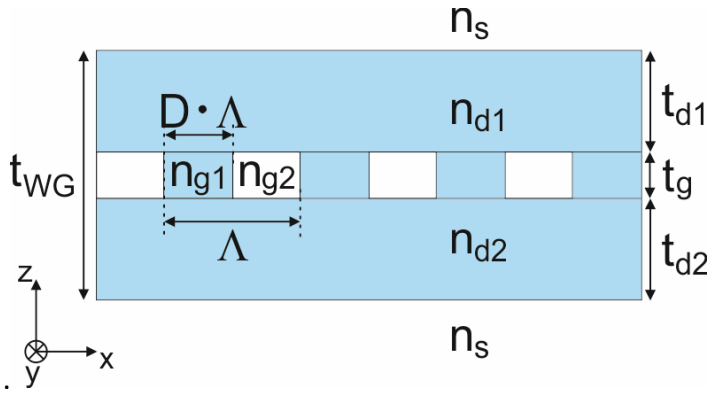

***Figure 4.1**: A symmetric waveguide grating of thickness t_{WG} consisting of an optical grating of thickness t_g sandwiches between two planar dielectric films of thicknesses t_{d1} and t_{d2}. TE polarization is considered in all simulations in this Chapter 4.*

Before starting to discuss the simulation results, the following scenario shall be considered, which provides an intuitive understanding of the mechanism behind the sensitivity of the waveguide grating with respect to optical asymmetry. At first, a node mode is excited via grating coupling from free-space and subsequently propagates inside the waveguide grating. Due to its interaction with the grating, the light is not only in-coupled, but also out-coupled into free space again with a propagation length L_{prop}. When there is no change in the refractive index (symmetric waveguide grating, $n_{d1} = n_{d2}, t_{d1} = t_{d2}$), the propagation length

can be large. However, when a refractive index change $\Delta n = n_{d1} - n_{d2} > 0$ occurs, the propagation length becomes significantly shorter due to the increased interaction with the grating caused by the shift of the node position.

In the next step, to quantify the sensitivity in propagation length, a waveguide grating geometry defined by the parameters shown in Figure 4.1 is used. From a technological perspective, $\chi_{gp} = 0.0$ is the more typical case, where a waveguide layer is deposited on a substrate and subsequently equipped with a surface structure to couple light from the outside at varying angles of incidence, which allows for the excitation of different waveguide modes. The symmetric case, however, is more technologically challenging, but can also have significant advantages as shown throughout this section. More details on the fabrication of symmetric optical slab waveguides are discussed in section 3.2.

4.1.1. Geometry with $n_{g1} = n_{g2}$

The first simulations aim to explain the important role of the TE_1 node mode, along with the impact of the waveguide symmetry. First, a planar “dummy" grating is implemented by setting the condition $n_{g1} = n_{g2}$ for the grating layer. The goal is to determine the overlap of the waveguide modes with this dummy grating layer, and thereby defining the filling factor FF as a measure for the interaction between the mode and the dummy grating layer. The filling factor is defined as the overlap integral of the form

$$FF = \frac{\int_{z_g}^{z_g+t_g} |E_y|^2 dz}{\int_{-\infty}^{\infty} |E_y|^2 dz},$$

whereby z_g and $z_g + t_g$ define the first and second interface of the dummy grating layer with respect to z (growth direction of the waveguide). This filling factor approach has already been used in transfer-matrix simulations, where only planar layers are considered, and it has been found valid at least for classical node modes. For certain phenomena discussed later in this thesis this measure is no longer valid, because it will be shown that in certain cases the propagation length can be infinite despite a finite filling factor. Here, however, the filling factor is used because it provides the reader with an intuitive insight of how the interaction between waveguide modes and a real optical grating can later be influenced. For the simulations, the waveguide grating is defined with the following exemplary parameters: $t_d =$

$0.632\ \lambda$, $t_g = 0.079\ \lambda$, $n_s = 1.0$, $n_{d1} = n_{d2} = 1.5$, and $n_{g1} = n_{g2} = 1.275$. **Figure 4.2** shows the simulation results for the comparison of the two cases $\chi_{gp} = 0$ (see Figures 4.2a and 4.2b) and $\chi_{gp} = 1$ (see Figures 4.2c and 4.2d).

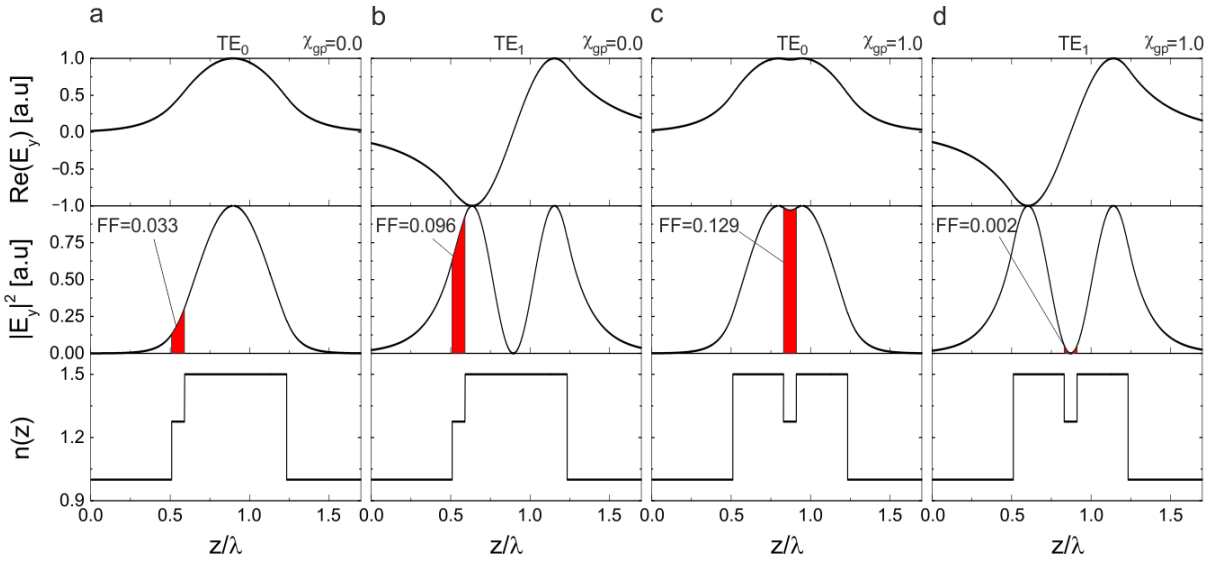

***Figure 4.2**: The distributions of the normalized electric field $Re(E_y)$ and normalized intensity $I \propto |E_y|^2$ as well as the corresponding filling factors (FF) of the mode with the grating layer. a) TE_0 mode at $\chi_{gp} = 0$; b) TE_1 mode at $\chi_{gp} = 0$; c) TE_0 mode at $\chi_{gp} = 1$; d) TE_1 mode at $\chi_{gp} = 1$.*

All field profiles shown in Figure 4.2 are well bound to the waveguide, as there are no loss channels due to the absence of a grating and absorption. As it can be seen in the simulated electric field profiles, the TE_0 mode does not possess nodes, while the TE_1 mode exhibits exactly one node. As it is also displayed in Figure 4.2, this node of the TE_1 mode shows a particularly interesting behaviour regarding the filling factor FF. The position of the node strongly influences the overlap of the electric field with the dummy grating layer and thus how strong the light interacts with that layer. While relatively large values of FF between 0.033 and 0.129 occur for all cases with asymmetry as well as for the TE_0 mode at $\chi_{gp} = 1.0$, a substantially lower filling factor of $FF = 0.002$ for the TE_1 mode and $\chi_{gp} = 1.0$ is obtained. Although due to the missing grating there is no out-coupling of light at this stage, this behaviour gives a first quantitative hint to potential changes in the propagation characteristics of the modes when the dummy is replaced by a real grating.

Furthermore, such a behaviour (sensitivity towards symmetry changes) would also enable a sensitivity of the optical waveguide with respect to changes in the electromagnetic environment of the system.

4.1.2. Geometry with $n_{g1} \neq n_{g2}$ and the variation of symmetry parameters

In the next case, a real optical grating is now introduced with $n_{g1} \neq n_{g2}$, which enables the out-coupling of light into the free space through transfer of lateral momentum provided by the optical grating. As the mode is out-coupled into the free space, the intensity of the propagating mode inside the waveguide grating decreases to $1/e$ of its initial intensity over the following normalized propagation length.

$$\frac{L_{prop}}{\lambda} = \frac{1}{4\pi\, Im(n_{eff})}$$

Thereby, n_{eff} is the effective refractive index of the mode.

For the next simulation, the parameters of the waveguide grating are set as $n_{g1} = 1.0$, $n_{g2} = 1.5$, $D = 0.5$, while otherwise using the same parameters as for the waveguide grating with the dummy grating layer.

Figures 4.3a and 4.3b show the normalized propagation length L_{prop}, and the angular divergence of the out-coupled light $\Delta\Theta$ as a function of the symmetry parameter χ_{gp}, with fixed values of $t_d = 0.632\ \lambda$, $\Lambda = 0.632\ \lambda$, and $t_g = 0.079\ \lambda$. For $\chi_{gp} = 0$, both the TE_0 and TE_1 modes exhibit small propagation lengths $\frac{L_{prop}}{\lambda}$ around 10^2 and large divergence angles $\Delta\Theta$ of the out-coupled light of approximately 0.1°.

Remarkably, for $\chi_{gp} = 1.0$, the TE_1 mode shows a significantly longer propagation length of $\frac{L_{prop}}{\lambda} = 1.2 \cdot 10^5$ and a much smaller divergence angle of only $\Delta\Theta = 0.0001°$.

Figures 4.3c-e present the two-dimensional electric field profiles as well as the electric field intensity distributions, $Re(E_y)$ and $|E_y|^2$, for the TE_0 and TE_1 modes at $\chi_{gp} = 0$, as well as the TE_0 mode at $\chi_{gp} = 1.0$. Compared to the field distributions shown in Figure 4.2, they

show significant spatial distortions, indicating a stronger interaction between the guided modes and radiating waves in free-space caused by the grating. However, a notable difference can be observed in Figure 4.3f, for the TE_1 mode at $\chi_{gp} = 1.0$. In this case, the distortion of the electric field profile caused by the grating is minimal, suggesting a much weaker interaction compared to the other cases shown in Figure 4.3.

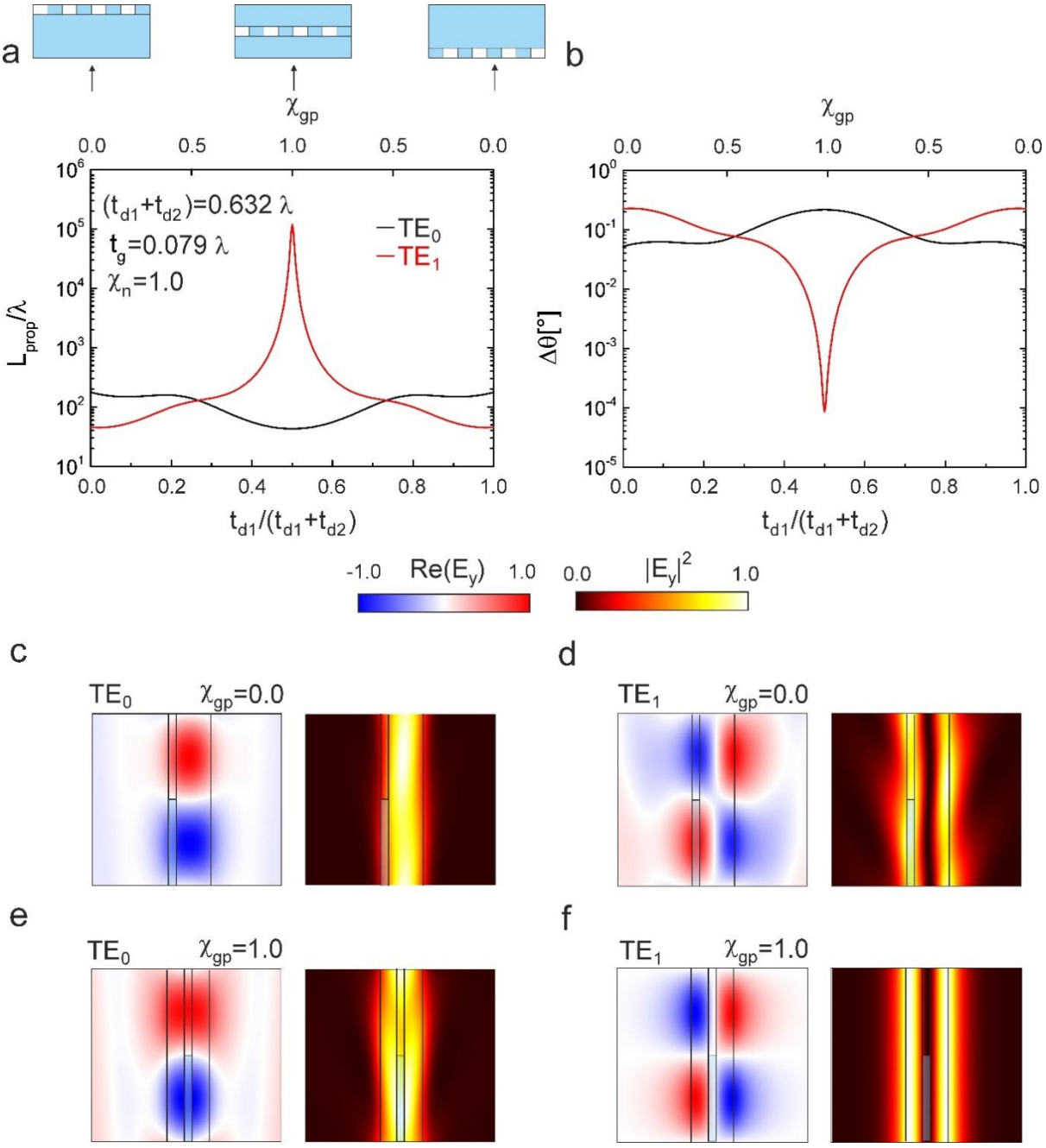

***Figure 4.3**: The variation of the asymmetry parameter χ_{gp} of a waveguide grating with $n_{g1} = 1.0$, $n_{g2} = 1.5$ and $D = 0.5$ under a constant value of $t_{d1} + t_{d2} = t_d = 0.632\ \lambda$. a) The normalized propagation length L_{prop}/λ; b) the divergence angle of the TE_0 mode (black) and*

TE_1 mode (red); c)-f) Normalized electric fields $Re(E_y)$ and field intensities $I \propto |E_y|^2$ of the TE_0 mode and TE_1 mode for $\chi_{gp} = 0.0$ and $\chi_{gp} = 1.0$.

The displayed TE_1 mode appears well confined to the waveguide grating although a loss channel is in principle offered by the grating. From the perspective of sensitive waveguides, it is immediately clear that the TE_1 mode exhibits particularly promising properties in the waveguide grating shown here, because of its pronounced dynamics around the symmetry position.

The distinct characteristic of $\frac{L_{prop}}{\lambda}$, $\Delta\theta$, and the field distributions originates from the small field overlap of the mode with the grating due to the node alignment. In a quantitative manner, the filling factor FF shown in Fig. 4.2 is small. However, FF cannot become exactly zero, because of the small but finite thickness of the grating, which also brings up technological questions for the implementation of an optimized waveguide grating. While the technological questions are discussed later in that section, first, an empirical study on waveguide gratings with $t_g < 0.1\ t_{WG}$ is performed to identify the correlation between the propagation length and the waveguide thickness. This empirical study yields the following correlation between the propagation length and the grating thickness.

$$\frac{L_{prop}}{\lambda} \propto \frac{1}{t_g^p}$$

As shown in **Figure 4.4a**, for the TE_1 mode and $\chi_{gp} = 1.0$, the scaling parameter is $p = 6$, which means that the propagation length of the TE_1 mode scales with t_g^{-6}. In contrast, the propagation length of the TE_0 mode at $\chi_{gp} = 0.0$ and $\chi_{gp} = 1.0$ as well as the TE_1 mode at $\chi_{gp} = 0.0$ all scale with $p = 2$. These different dependencies likely arise because the radiative loss rate α of the grating scales with t_g^2, while the filling factor scales approximately with t_g^3 for the TE_1 mode at $\chi_{gp} = 1.0$, and t_g^1 in the other case. These scaling rules remain valid up to a grating thickness of around $t_g/t_{WG} \approx 0.39$. Figure 4.4a also shows that the TE_1 at $\chi_{gp} = 1.0$ is advantageous as long as the grating is thin compared to the overall thickness, which in turn has to be thick enough to support the TE_1 mode. The latter argument leads to a further investigation, which focuses on the requirements for the waveguide grating thickness t_{WG}.

Figures 4.4c and 4.4d show $\frac{L_{prop}}{\lambda}$ and $\Delta\theta$ as functions of t_{WG}/λ at a fixed $t_g = 0.079\ \lambda$. For the TE_1 mode at $\chi_{gp} = 1.0$, $\frac{L_{prop}}{\lambda}$ is significantly larger than in all other cases, across all values of t_{WG}/λ above the cut-off of the mode. Thus, as long as t_g is small relative to t_{WG} and at the same time t_{WG} is large enough to support the TE_1 mode, the propagation length $\frac{L_{prop}}{\lambda}$ are comparatively large and the divergence angle $\Delta\theta$ are comparatively small across a broad range of grating thicknesses t_g.

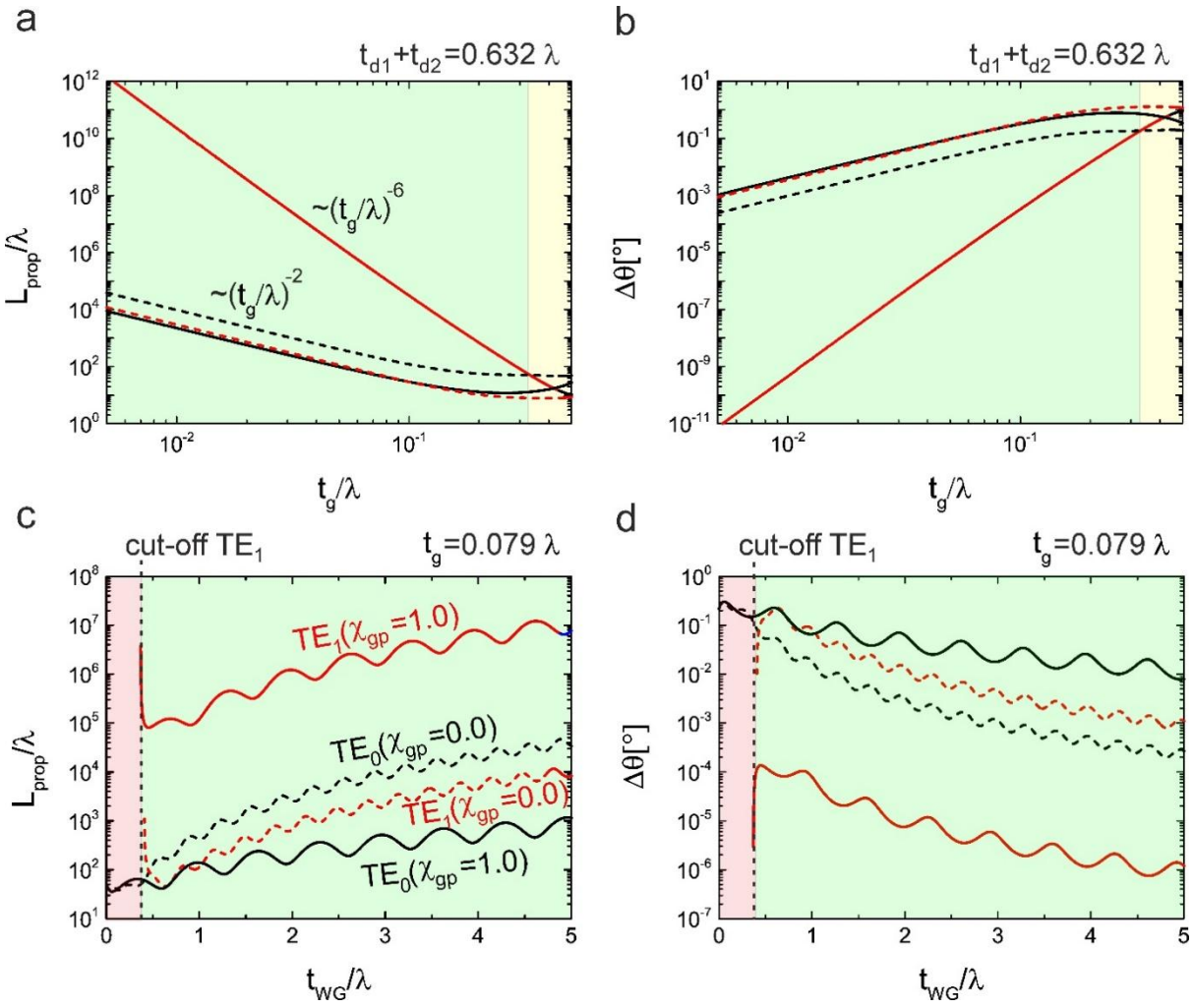

***Figure 4.4**: a) The normalized propagation length L_{prop}/λ; b) the divergence angle of the TE_0 mode (black) and TE_1 mode (red) under variation of the normalized grating thickness t_g/λ for $\chi_{gp} = 0.0$ (dashed lines) and $\chi_{gp} = 1.0$ (solid lines) with a fixed normalized waveguide grating thickness $t_{d1} + t_{d2} = 0.632\ \lambda$; c),d) Corresponding plots under the variation of the normalized waveguide grating thickness t_{WG}/λ with a fixed normalized grating thickness $t_g = 0.079\ \lambda$.*

To emphasize the role of these characteristics in an optical application scenario, it is convenient to compare the absolute propagation lengths of the different modes supported by the waveguide grating. The TE_1 mode at $\chi_{gp} = 1.0$ for a wavelength $\lambda = 632\ \mathrm{nm}$, which is a typical laser wavelength (e.g. of He-Ne gas lasers) often used in optical experiments, and a grating thickness $t_g = 50\ \mathrm{nm}$. For these parameters, the propagation length L_{prop} reaches 7.6 cm. This means that the light can propagate inside the waveguide over macroscopic distances. In contrast, for the TE_0 at $\chi_{gp} = 0.0$, the propagation length is only 110 µm. To match the propagation length of the TE_1 mode at $\chi_{gp} = 1.0$, the grating thickness would need to be reduced to only 0.88 nm, which in practice corresponds to the thickness of only a few atomic layers. For comparison monolayers of common 2D materials such as graphene or molybdenum disulfide (MoS_2) are only 0.34 nm and 0.65 nm in thickness or interlayer distance, respectively.[112,113] Therefore, using the TE_1 mode in a symmetric waveguide grating, in which the node position of the mode and the grating are well aligned enables large propagation lengths, while keeping stack parameters in a technologically feasible range.

While the potential advantages of the TE_1 mode, particularly in relation to technological considerations, have been mentioned, another crucial step in examining this concept is investigating the broadband behaviour of the waveguide grating. In many optical applications, it is desirable not only to operate the system at one specific wavelength but to achieve good performance across a wide spectral range. This is especially important in the context of integrated optical systems, where (different) semiconductor lasers are typically used instead of gas lasers due to their compact size, compatibility with semiconductor technology, and lower costs. Therefore, the broadband propagation properties of both modes (TE_1 and TE_0) will be examined in the following.

Figure 4.5a shows the dispersion relation for the TE_1 mode at $\chi_{gp} = 1.0$ and the TE_0 mode at $\chi_{gp} = 0.0$, with all other geometric parameters held constant compared to the results shown in Figures 4.3 and 4.4. Notably, the TE_1 mode exhibits large propagation lengths $\frac{L_{prop}}{\lambda}$, ranging between 10^4 and 10^6, over a broad spectral range from $\frac{\lambda}{t_{WG}} = 0.9$ and $\frac{\lambda}{t_{WG}} = 2.0$. The reason for this behaviour is the symmetry of the waveguide grating, which forces the node of the TE_1 mode to remain aligned with the central plane of the waveguide grating.

As a result, regardless of the wavelength, a similar situation to that described in Figure 4.3 persists as long as $\frac{\lambda}{t_{WG}}$ remains in a regime below the cut-off for the TE_1 mode. In contrast, the TE_0 mode shows much smaller propagation lengths ranging from $\frac{L_{prop}}{\lambda}$ between 10^2 and 10^3 across all displayed values for $\frac{\lambda}{t_{WG}}$.

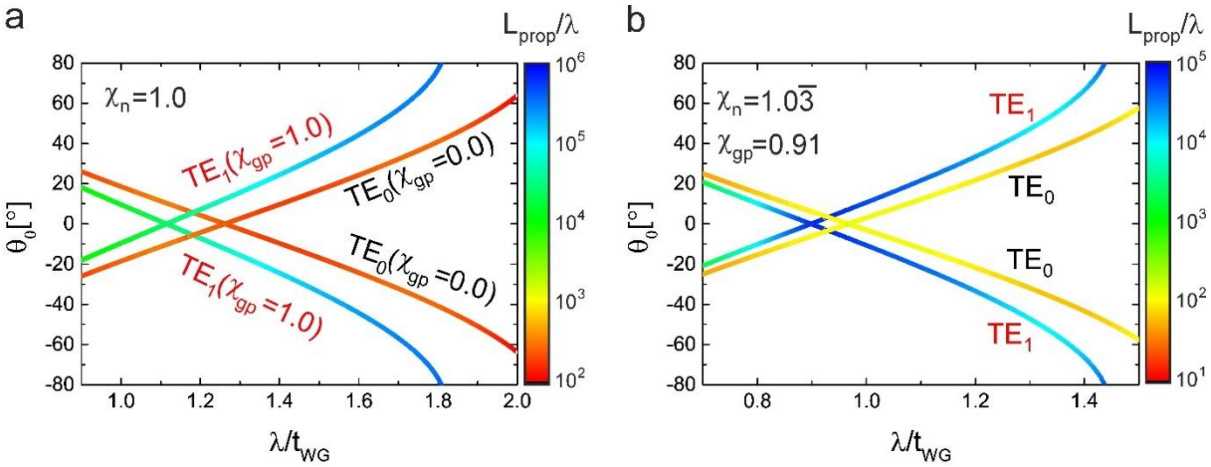

***Figure 4.5**: a) The dispersion relations and propagation lengths of the TE_0 mode for $\chi_{gp} = 0.0$ and the TE_1 mode for $\chi_{gp} = 1.0$ at fixed geometry parameters $\chi_n = 1$, θ_0 is the external out-coupling angle; b) Dispersion relations and propagation lengths for an asymmetric geometry with $\chi_{gp} = 0.91$, $\chi_n = 1.0\overline{3}$ for both the TE_0 mode and TE_1 mode with $\frac{t_g}{t_{d1}+t_{d2}} = 0.045$.*

For an asymmetric geometry ($\chi_{gp} \neq 1.0$ and $\chi_n \neq 1.0$), the TE_1 mode exhibits a maximum propagation length $\frac{L_{prop}}{\lambda}$ of approximately 10^5 at a specific $\frac{\lambda}{t_{WG}} = 0.96$, as shown in Figure 4.5b. Since the waveguide grating stack is no longer mirror symmetric, the node position of the TE_1 mode is not inherently aligned with the grating anymore. However, the node position shifts in growth direction as a function of the wavelength, and thus at a fixed wavelength as a function of the symmetry parameters. The maximum $\frac{L_{prop}}{\lambda}$ is observed when the filling factor (FF) is minimized. From the technological perspective this is a very important finding, as influencing the optical symmetry could enable control over the propagation length, and thus over the coupling behaviour of light into free space. Since a dynamic change in layer thickness (geometric symmetry) does not represent the most intuitive form of influence from a technological standpoint (however a promising implementation for this will be presented at

the end of this thesis), the focus will first be on investigating the effect of RI symmetry χ_n on the mode propagation length. In practice, the refractive index, and also the thickness, of a layer can change based on a variety of effects.

For example, a change in RI or thickness can arise due to the physical adsorption of molecules on the waveguide surface (mainly thickness change), via NLO effects, such as the Pockels or Kerr effect (only refractive index change), or a change in temperature (both RI and thickness change).

4.1.3. Sensitivity to asymmetric refractive index changes

In this last part of the section 4.1, the sensitivity of the waveguide grating to an asymmetric change in the refractive index at $\chi_{gp} = 1.0$ will be investigated. Specifically, this refers to varying n_{d1} while keeping n_{d2} fixed at 1.5. For this study, the grating thickness is set to $t_g = 1.5 \cdot 10^{-3}\lambda$, while all other geometry parameters remain identical to those in Figures 4.3 and 4.4. This configuration enables to assess how sensitive the waveguide grating is to asymmetric refractive index variations.

Two simulation parameters are of interest in order to investigate the sensitivity of the waveguide grating. First, for small changes of the refractive index, the figure of merit

$$FoM(n_{d1}) = \frac{1}{L_{prop}(n_{d1})} \frac{\partial L_{prop}(n_{d1})}{\partial n_{d1}}$$

provides a measure (in this thesis referred to as performance) for the sensitivity. However, for more practical considerations, the refractive index is commonly switched between two distinct values with a difference of Δn. The sensitivity can be defined by

$$S_{\Delta n} = \frac{L_{prop}(n_{d1}+\Delta n)}{L_{prop}(n_{d1})},$$

here for $\Delta n = 1 \cdot 10^{-4}$, as this is a typical value for RI changes caused by the Pockels effect[114,115].

Figure 4.6 shows the propagation length $\frac{L_{prop}}{\lambda}$, the figure of merit (FoM), and the sensitivity $S_{\Delta n}$ as functions of n_{d1} for both the TE_0 and TE_1 modes. Similar to the variation of χ_{gp} discussed in Figures 4.3 to 4.5, the TE_1 mode exhibits remarkably high values of $\frac{L_{prop}}{\lambda}$,

reaching up to 10^{12} when χ_n approaches 1.0. Notably, $\frac{L_{prop}}{\lambda}$ for the TE_1 mode is highly sensitive to changes in n_{d1}, as shown in Figure 4.6a. In contrast, the TE_0 mode shows almost constant propagation lengths of $\frac{L_{prop}}{\lambda}$ around 10^3.

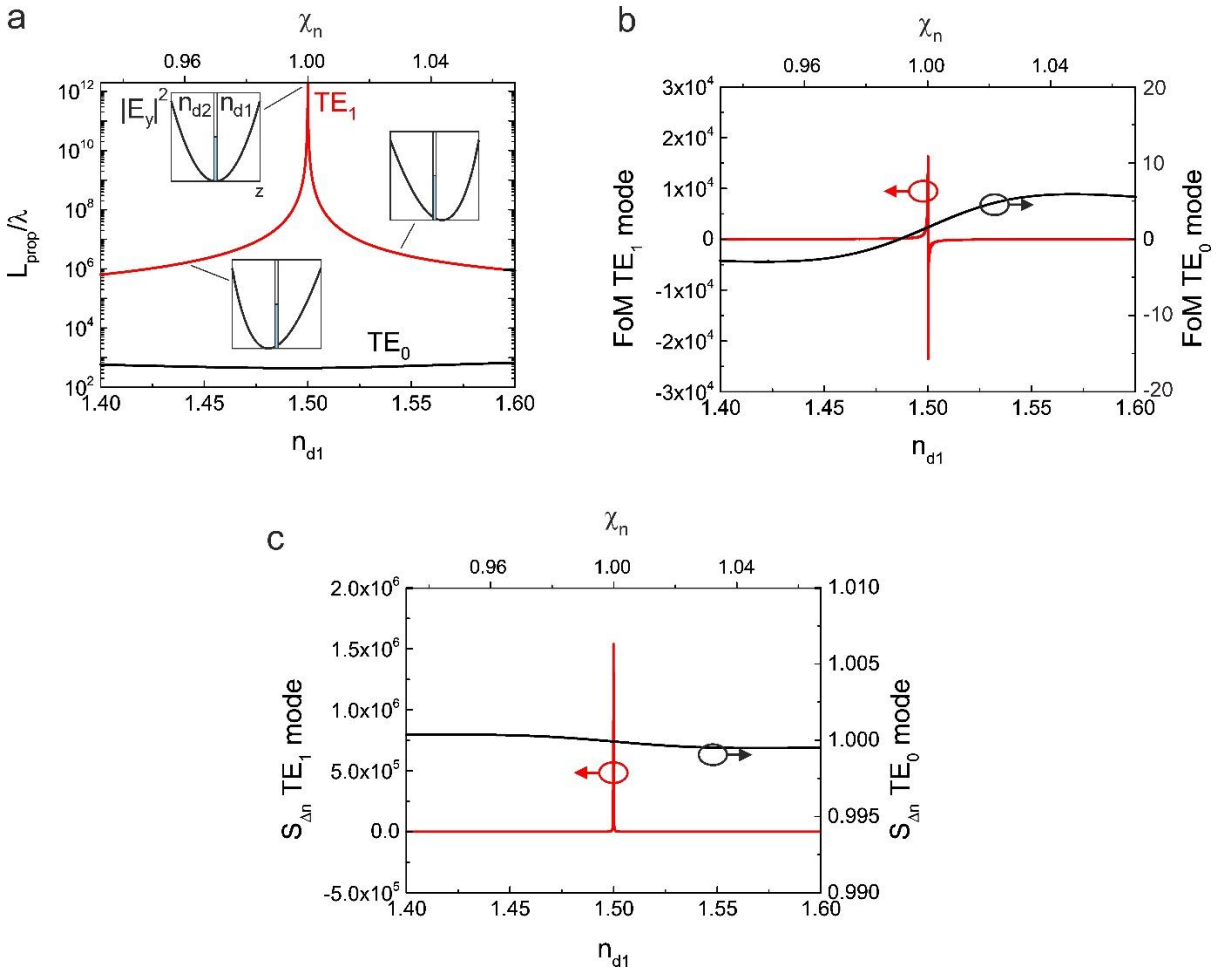

***Figure 4.6**:* Sensitivity to asymmetric refractive index changes. *a) The normalized propagation length; b) Figure of Merit (FoM); c) $S_{\Delta n}$ of a waveguide grating with $t_g = 1.5 \cdot 10^{-3}\ \lambda$ and asymmetric refractive index changes (n_{d1} is varied and n_{d2} is fixed at a value of 1.5).*

The FoM for the TE_1 mode reaches values as high as $2 \cdot 10^4$, while the maximum FoM for the TE_0 mode within the displayed range is only 5.6. This vast difference in FoM is primarily due to the significant decrease in $\frac{L_{prop}}{\lambda}$ when asymmetry is introduced for the TE_1 mode. Regarding the sensitivity $S_{\Delta n}$ displayed in Figure 4.6c, for a refractive index change of$\Delta n = 10^{-4}$, the TE_0 mode shows values of $S_{\Delta n}$ close to 1. However, the TE_1 mode exhibits a peak sensitivity at $\chi_n = 1.0$, reaching a much higher value of approximately $1.5 \cdot 10^6$. The choice of this interval is based on practical reasons. In many Pockels materials, this falls within the

order of magnitude at which the refractive index can be changed before the material's breakdown field strength is reached or saturation effects occur.

In comparison, previous literature reports on propagation length sensitivity to refractive index changes show FoM values around 3 and $S_{\Delta n} \approx 1.005$, which demonstrates the potential of node aligned waveguide gratings for sensitive optical applications. Furthermore, from the results discussed in this section 4.1 it becomes clear that the strong dependence of the light-grating interaction on the symmetry is the main mechanism behind the high sensitivity. Consequently, optimization would require the ability to fully avoid the interaction with the grating in the symmetric case. However, this is not possible using TE_1 in the demonstrated configuration of a waveguide grating, as although the filling factor can be very small but can never completely vanish due to the finite grating thickness and the node being just a singular position. A widely discussed phenomenon in the recent literature that allows for a completely vanishing interaction with the grating are the so-called bound states in the continuum (BICs). BICs have been reported across a variety of physical disciplines, including quantum mechanics[116], acoustic[117], and more recently also in optics[108,118–120].

The principle behind this is essentially the destructive interference of all waves that would radiate into free-space (radiative loss channels), resulting in a mode that is fully bound to the waveguide. Thus, the propagation length of such states is infinite. This is in contrast to the case in 1) in this section, where also fully bound modes can be generated, however in absence of any grating. The BICs exists despite the presence of a grating. Usually these conditions of destructive interference of all loss channels are only fulfilled at singular positions in energy and momentum. Thus, BICs are commonly considered singularities. Taking into account Heisenberg's uncertainty principle, this singular nature renders BICs often difficult to utilize for practical purposes. However, proof-of-principle reports can already be found in the literature including applications such as lasers[121], and sensors[122].

In addition to these promising approaches, the focus of this thesis will be on developing strategies, particularly focussing on ease of fabrication, facile implementation in realistic application scenarios as well as broadband operation, which all seem to be typical obstacles in modern BIC research.

4.2. The Phenomenon of Zero Diffraction and its Opportunities for Broadband Switching of Light

(The following section is based on journal paper 5 of the publication list.)

In the last section, the minimized interaction of a node mode with the grating inside a slab waveguide has been utilized to reduce waveguide losses and to create a sensitive optical waveguide structure. In this next section, the idea is to not only consider symmetric waveguide gratings and illuminate them from one direction with a plane wave. Here, also the illumination conditions shall be mirror symmetric with respect to the symmetry plane of the waveguide grating. Once again, by using RCWA, it will be first investigated in the following section whether such an illumination scenario can be of benefit for sensitive waveguides. The basis for this idea is the following. In a symmetric waveguide, the field profiles of the modes can be interpreted as standing waves created by the interference of plane waves with symmetric incidence on the centre plane of the waveguide. For even (e.g. TE_0) and odd modes (e.g. TE_1) in a symmetric waveguide, these waves exhibit constructive or destructive interference at the centre plane, respectively. Based on this understanding, the symmetric illumination of a stand-alone grating by a pair of plane waves could enable to control the diffraction efficiency by adjusting the relative phase between the waves. In the picture of section 4.1, the node position would shift dependent on the relative phase between the two plane waves forming the mode. Recent papers also report such behaviour in somewhat similar configurations.[123]

To prove this hypothesis, the propagation lengths $L_{prop,TE0}$ and $L_{prop,TE1}$ for the TE_0 and TE_1 modes in a symmetric waveguide grating are investigated. As in the previous section, the propagation length, which describes the distance over which the mode's intensity decays to $1/e$, is derived from the imaginary part of the effective index.

In the first step, in contrast to the waveguides in section 4.1, the cladding layers are removed from the waveguide grating, resulting in a stand-alone grating surrounded by two half-spaces with refractive index of the core material (see Figure 4.7a). Simulations on this rather academic case are performed with symmetric plane wave incidence with varying their relative phase difference including two distinct cases.

In one case, the relative phase between the two plane waves incident on the structure is set to $\Delta\Phi = 0$, which results in constructive interference of the two waves at the grating. In the other case, the relative phase is set to $\Delta\Phi = \pi$, which in turn results in destructive interference at the grating.

By tuning the relative phase $\Delta\Phi$ of the incident beams, the interaction strength of light with the grating can be defined as the contrast C in diffraction efficiency η, since there is no mode to determine a propagation length.

$$C = \frac{\eta_{max}}{\eta_{min}}.$$

The first results displayed in **Figure 4.7** show that this contrast C closely matches the ratio $L_{prop,TE1}/L_{prop,TE0}$ of the propagation lengths for the waveguide grating modes, demonstrating a strong correlation between the phase-tuned diffraction efficiency and the propagation properties of the waveguide modes. Small deviations, which are noticeable in Figure 4.7a may arise due to the different momenta of the TE_0 and TE_1 modes. The contrast observed under symmetric incidence at a stand-alone grating of thickness scales as t_g^{-4}. As a result, achieving high contrast requires a very thin grating. However, decreasing t_g also leads to a decrease in the maximum diffraction efficiency η_{max}, an issue which is closely related to the one discussed in the previous section 4.1, including the technological challenges. Thus, the goal is to balance the trade-off between contrast and efficiency.

Figure 4.7b illustrates the geometry of the stand-alone grating used for the RCWA simulations, alongside the contrast map $C = \eta_{max}/\eta_{min}$ shown in Figure 4.7c. The thickness of the grating has been chosen to be relatively thick ($t_g = 200$ nm) here to account for practical feasibility in terms of technological implementation (compare with the waveguides discussed in the previous Section 4.1). Comparing the waveguide grating under single plane wave incidence with the stand-alone grating under dual plane wave incidence (Figures 4.7a-c) allows for two conclusions.

The first conclusion is related to the drawbacks of the resonator. If present, the waveguide grating acts as an optical resonator, supporting discrete waveguide modes, a fact that

inherently limits the bandwidth. This bandwidth limitation is undesirable for applications requiring broader tuning ranges.

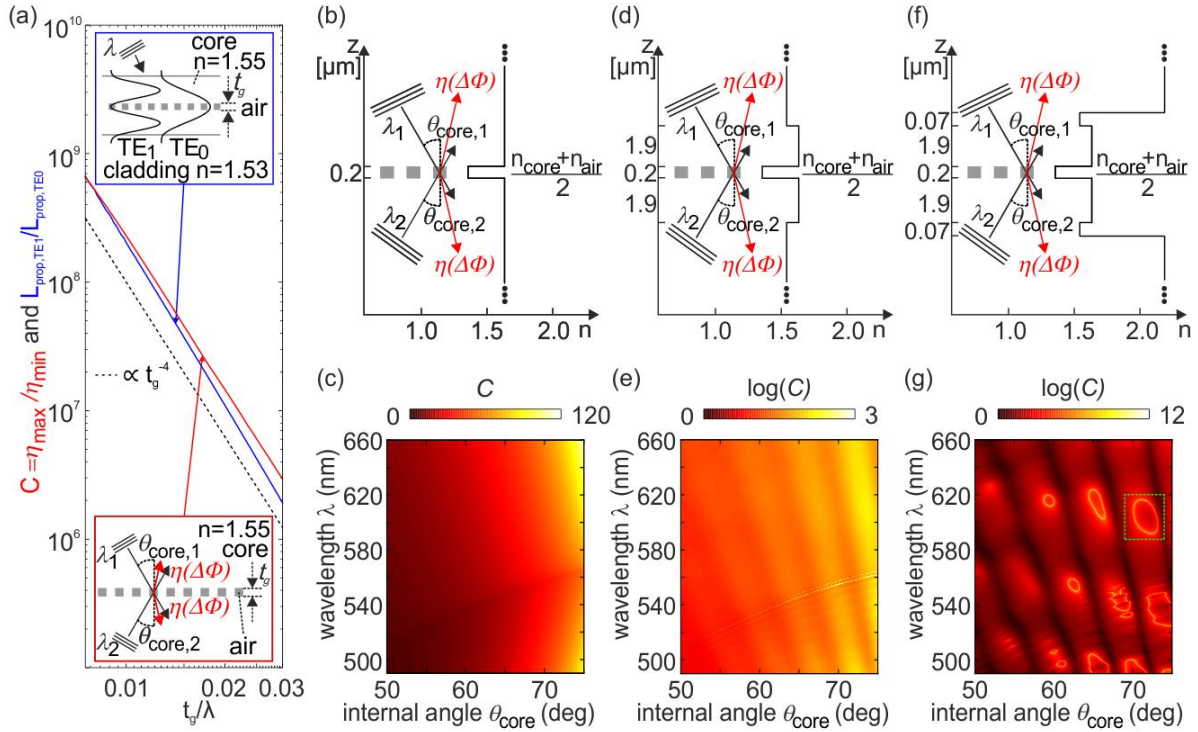

***Figure 4.7**: Simulations of the diffraction of a pair of plane waves at different loss-free structures by RCWA. a) Ratio of the propagation length L_{prop} of TE_0 and TE_1 modes at small grating thickness t_g compared with the contrast $C = \eta_{max}/\eta_{min}$ under symmetric dual plane wave incidence (internal angle $\theta_{core,1} = \theta_{core,2}$, wavelength $\lambda_1 = \lambda_2$) on a stand-alone grating; b) this stand-alone grating at $t_g = 200$ nm; c) contrast map over wavelength and internal angle showing that destructive interference at the grating alone does not enable high contrast; d) waveguide grating with e) contrast map corresponding to the waveguide from d); f) leaky waveguide grating with g) near-elliptical curves of infinite contrast (not observed for a stand-alone grating).*

In contrast, without the cladding layers (Figures 4.7b and 4.7c), there are no internal back reflections, and therefore, no resonator effect. As a result, the diffraction efficiency η can be tuned over a wide range in energies (wavelengths) and momentum (incident angles), without being restricted by resonant conditions.

This allows for more flexible tuning in simpler geometries. However, this optimized switching performance in a stand-alone grating comes with a trade-off. In practice, achieving perfectly symmetric illumination conditions with two light beams is highly challenging.

Therefore, from the practical perspective, the symmetric waveguide grating offers a distinct advantage: it can be excited from just one side. Internal reflections within the waveguide subsequently create symmetric wave patterns that automatically align with the grating, which significantly simplifies the optical setup in an experiment. Exactly this point leads to the second conclusion—the benefit of the waveguide. The internal symmetry facilitated by the waveguide makes it easier to achieve symmetric illumination conditions without the need for complex illumination schemes.

Based on these two conclusions, the two approaches are now combined. Thus a waveguide grating under symmetric illumination by two plane waves is investigated, similar to the setup in Figure 4.7b. The geometry for this configuration is shown in Figure 4.7d. As expected, maximized diffraction occurs at $\Delta\Phi = 0$, while minimized diffraction is found at $\Delta\Phi = \pi$. Compared to the stand-alone grating, the contrast is improved (average contrast of $\bar{C} = 41$ instead of $\bar{C} = 24$) but remains somewhat limited, as shown in Figure 4.7e. The increased contrast is observed only along resonant waveguide modes, which shows the inherent bandwidth limitation of a resonator.

To overcome this limitation, in a third step, the waveguide grating is transformed into a leaky structure (see refractive index profile in Figure 4.7f). In this modified design, the former cladding layers are reduced to thin buffer layers, and a high-index ambient medium is introduced on both sides of the waveguide. This leakiness may enable greater interaction between the waveguide modes and the environment, supporting the levelling of the waves.

As a result, the average contrast is now significantly increased to $\bar{C} = 4.2 \cdot 10^5$ (Figure 4.7g). It should be noted here that the average contrast depends on the resolution of the contrast plot, because of the influence of the infinite contrast along the ellipses. Nevertheless, the average contrast representation illustrates that the approach of introducing leakiness offers advantages including a more efficient and tuneable diffraction performance.

These advantages are promising for overcoming the bandwidth limitations observed in fully confined waveguides. Remarkably, along curves with a near-elliptical shape, the contrast converges to infinity. As shown in Figure 4.7, this phenomenon is not simply the result of standard destructive interference. Achieving infinite contrast requires a leaky waveguide grating.

To further investigate these near-elliptic contrast features, one of them is examined in more detail. **Figure 4.8a** shows the contrast map in the area marked by the green dashed rectangle from Figure 4.7g. Then, a line cut of that near-elliptic feature at $\lambda = 600\ \mathrm{nm}$ is displayed in Figure 4.8b, along with the maximum and minimum diffraction efficiencies η_{max} and η_{min} in Figure 4.8c. At two distinct positions in momentum (on the near-elliptic feature), the minimum diffraction efficiency tends to zero, causing the contrast to theoretically reach infinity. This means that any line cut through the near-elliptical curve will contain two singularities, where the diffraction can be tuned to zero for $\Delta\Phi = \pi$.

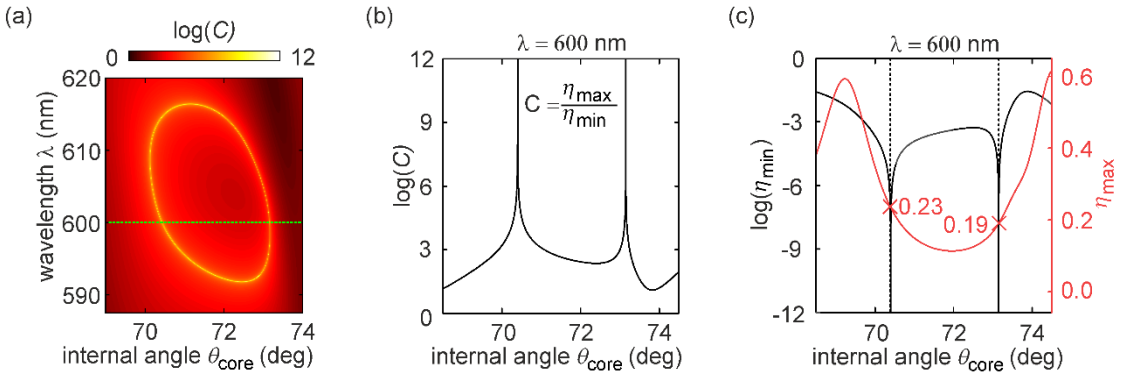

***Figure 4.8**: A near-elliptic curve of infinite contrast. a) Contrast $C = \eta_{max}/\eta_{min}$ of the leaky waveguide structure; b) line cut at $\lambda = 600$ nm (dashed green line in a); c) minimum η_{min} and maximum η_{max} diffraction efficiency.*

Interestingly, at these points of infinite contrast, here the diffraction efficiency can still be relatively large by adjusting the relative phase ($\eta_{max} = 0.23$ and $\eta_{max} = 0.19$ at the two intersections with the near-elliptic curve).

The reason for that behaviour lies in the levelling of the waves within the leaky waveguide grating, which causes a symmetrisation of the scattering matrix representing the waveguide grating.

As a result, the waveguide grating behaves similar to a stand-alone grating, while exploiting the benefits from a waveguide. A detailed mathematical description of these phenomena can be found in the supporting information of journal article 5 of the publication list.

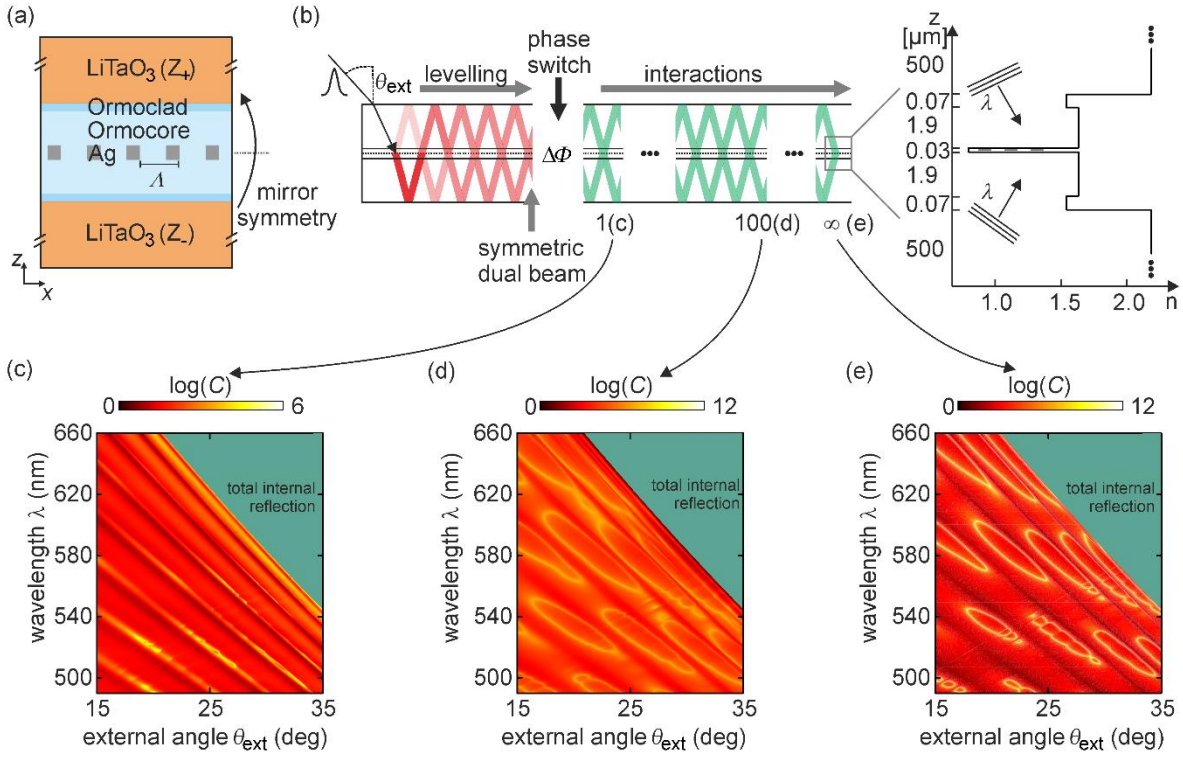

***Figure 4.9**: Simulations of the more realistic experimental conditions using Gaussian beams in a geometry for realizing dual plane wave incidence. a) Mirror-symmetric geometry of the proposed sample with lithium tantalate ($LiTaO_3$) serving as Pockels material to tune the phase and a silver grating in the center of a polymer waveguide grating; b) several interactions with the waveguide grating under single Gaussian beam incidence with external angel θ_{ext}: levelling of amplitudes (red beam), trapping by switching the relative phase to $\Delta\Phi = \pi$ via the Pockels effect and several interactions of the trapped beam (green beam); c) contrast map after one interaction; d) after 100 interactions; e) after an infinite number interactions of the light beams (plane waves) with the garting.*

In the next step, further simulations are intended to describe more realistic conditions for a subsequent experiment, thereby determining the experimental requirements for the practical characterization of the phenomena described above. First, a symmetric waveguide grating is required. In the experiments, an optimal symmetry is achieved using a silver grating fabricated by transfer printing[98].

Therefore a thin silver grating with $t_g = 30\ \mathrm{nm}$ instead of a lossless dielectric grating is used for these simulations. All other parameters are identical to the leaky waveguide structure discussed before.

The next practical challenge is achieving perfectly symmetric dual plane wave incidence. As previously discussed, a symmetric waveguide naturally levels the waves, generating internal symmetric plane waves. To exploit this, we position the leaky symmetric waveguide grating at the centre of an outer nonlinear waveguide (see **Figure 4.9a**). This outer waveguide is composed of two $LiTaO_3$ wafers with equal thicknesses (500 µm). The normal vector of the wafer surface is parallel to the c-axis of the $LiTaO_3$ crystal. This means, as explained in the fundamentals chapter, that by applying an electric field in normal direction to the wafer, the Pockels coefficients r_{13} and r_{33} are addressed. Via the polarization, in this case TE, the effective Pockels coefficient in the experiment is r_{13}. The Pockels coefficient r_{13} of these particular wafers has been measured using a Mach-Zehnder interferometer resulting in $r_{13} = 8.4\ \mathrm{pm/V}$. However, only the Pockels material surrounding the waveguide grating is not sufficient. The orientation of the wafers is opposite with respect to the c-axis (Z+ and Z- parallel to the growth direction). This means that opposite refractive index changes of +Δn and −Δn are created when an external electric field is applied across the entire waveguide stack. This enables to tune the relative phase ΔΦ between 0 and π.

However, under plane wave incidence, the outer nonlinear waveguide would act as a secondary resonator, limiting bandwidth and thus significantly reducing the contrast. To overcome this, the outer waveguide must be excited using a single Gaussian beam with a diameter smaller than the total waveguide thickness. Each Gaussian beam can be viewed as a superposition of plane waves, and by covering a momentum range, the overall switching contrast can be calculated by averaging the plane wave solutions obtained via RCWA.

The beam, which is coupled into the device via diffraction, levels upon multiple interaction with the grating, forming two perfectly symmetric Gaussian beams that intersect at the position of the leaky waveguide grating. Hereinafter, these intersections are referred to as "dots" because of their visual appearance in the far-field, as shown in the experimental results later in this section. Through partial transmission and reflection at the waveguide grating, the beam amplitudes equalize after a few interactions.

Importantly, the beams do not show interference within the outer nonlinear waveguide because the dots are spatially separated. This allows the waveguide to enable levelling without functioning as a resonator.

In the second step, the relative phase of the dual beam is switched by $\Delta\Phi = \pi$ via the Pockels effect, resulting in minimized diffraction. Consequently, the dual beam remains trapped within the waveguide and does not exit by diffraction. This behaviour occurs not only at the first dot but also at all subsequent dots. After the phase switch, the generated dual beam is drawn green instead of red in Figure 4.9b, indicating its confinement to the waveguide.

In the last step, the resulting contrast is investigated when the trapped dual beam is de-trapped by another phase shift of π ($\Delta\Phi = 0$), which maximizes the diffraction efficiency at the waveguide grating. Figure 4.9c shows the contrast map of the de-trapped dual beam at the first dot. Interestingly, this contrast map is strongly influenced by the number of dots that are considered. This phenomenon can be explained by the relationship between spatial and momentum uncertainty. In the radiative state, the beam is localized to only a few dots, leading to a relatively broad range of momentum or angle. Conversely, in the trapped state, the beam is confined between the trapping and detrapping positions, causing the beam's momentum to become more defined with longer propagation, resembling a plane wave (as indicated on the right side of Figure 4.9b). Accordingly, Figure 4.9e has been simulated assuming only two plane waves. Notably, similar near-elliptic regions of infinite contrast are observed, as seen in Figures 4.7g and 4.8, even though a silver grating is used instead of a lossless dielectric grating.

In summary, the device concept shown in Figure 4.9a theoretically enables symmetric dual-plane wave incidence with controlled phase on a leaky symmetric waveguide grating. While plane wave excitation ideally requires infinite lateral dimensions, Figure 4.9 demonstrates the performance of a real device with finite dimensions. The transition from Figure 4.9e to Figures 4.9d and 4.9c illustrates how spatial localization averages the ideal contrast map over a larger momentum range, reducing contrast for the Gaussian dual beam. Remarkably, even when detrapping occurs immediately after trapping (Figure 4.9c), a high contrast of 10^2 to 10^4 is achieved over a wide spectral range, both in terms of energy (wavelength of the Gaussian beam) and momentum (external excitation angle).

The fabricated device, as described in Figure 4.9a, is now shown in **Figure 4.10**. After diffraction into the waveguide, the beam is split by the waveguide grating and levelled to create symmetric dual beam incidence. Figure 4.10 highlights two phase-switching events as explained earlier. To facilitate this, tip electrodes are placed between selected dots at the positions marked by an 'x'. These electrodes control the diffraction efficiency of the Gaussian dual beam. When no diffraction occurs, the dual beam remains guided and trapped within the outer nonlinear waveguide. Conversely, diffracted beams fall at an angle below the critical angle for total internal reflection, allowing them to exit the lithium tantalate. In this way, diffraction enables the dual beam to be de-trapped as it leaves the device.

Figures 4.10a and 4.10b show the switching between the trapped and de-trapped states. The two electrodes are set to the same potential and shift the local phase by $\Delta\Phi$ at each position x. In Figure 4.10b, the dual beam is diffracted at a global phase value of $\Delta\Phi = 0$, making all the dots visible in the far-field and projected onto a diffusive screen. In contrast, Figure 4.10d shows the case where a local phase shift of $\Delta\Phi = \pi$ is applied at both electrode positions marked by 'x'. After the first phase shift, the dual beam is trapped, propagating largely undisturbed through the waveguide despite of the presence of the grating in the ideal case like a BIC. The phase shift at the second electrode then causes de-trapping, resulting in the dual beam being diffracted once again.

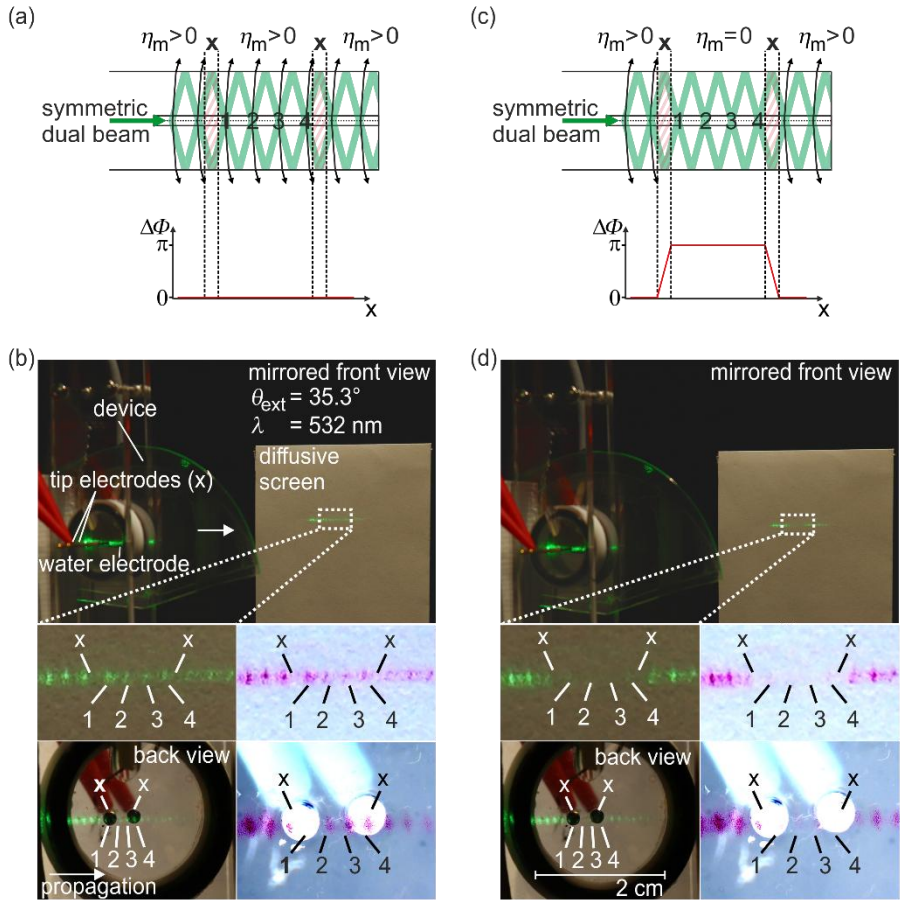

***Figure 4.10**: Experimental realization of the leaky waveguide grating with phase control by a Pockels material. a, b) a global phase value of $\Delta\Phi = 0$ and diffraction at every interaction projected on a diffusive screen (inset); c,d) $\Delta\Phi = \pi$ between both electrode positions, marked by an 'x' and no diffraction between the electrodes (dots 1…4).*

The electric field is applied by two tip electrodes on the one side of the waveguide stack (marked by an x) and a water electrode, which is large compared to the tip electrodes on the other side. First, a single laser beam is in-coupled by a grating, (θ_{ext}=35.5 ° and λ = 532 nm), the symmetric dual beam is then formed inside the waveguide as shown in Figure 4.9b

As a result, the dots appear dark between the electrodes (indicating the light being trapped) but become bright again after the second electrode (indicating the light being de-trapped again). Figure 4.10d demonstrates that even when the Gaussian dual beam is trapped, it continues to transport optical power effectively, showing the potential of this phase-switching mechanism for controlling the geometric path of light within the waveguide.

From a technological perspective, this is certainly a very promising finding, as new ways are being sought in optical interconnection technology to control the geometric properties, such as the propagation direction. The focus in such devices is primarily on very short switching timescales in combination with high switching contrast covering a wide angular range. In many modern implementations, compromises are made, for example, in terms of speed (in mirror-based mechanical systems) or in angular range (in systems based on nonlinear waveguides).

To verify the contrast of the described device, we measured the detrapped power as a function of the globally applied electric field strength using water electrodes (**Figure 4.11a**). These electrodes offer two key advantages: first, they prevent measurement errors caused by scattering from electrode edges, and second, they enable the application of a homogeneous external electric field E perpendicular to the device surface.

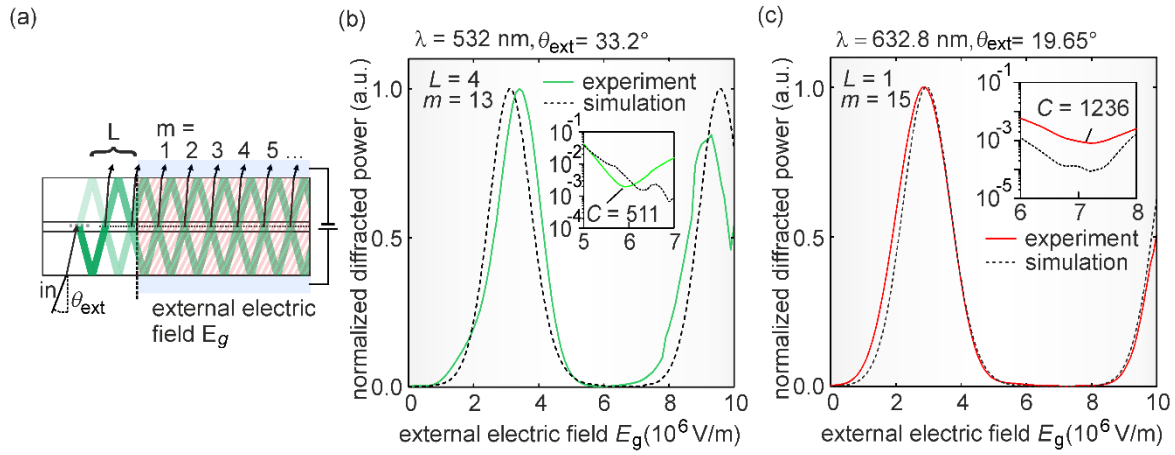

***Figure 4.11**. Experimental results on the high contrast electrical switching of light. a) schematic sketch of the experiment with water electrodes on both sides and global phase control; b,c) normalized measured (solid line) and simulated (dashed line) optical power signal in diffraction direction for red (632.8 nm) and green (532 nm) light.*

Simulations were conducted using finite beam rigorous coupled-wave analysis (FB-RCWA), assuming Gaussian beams with a 500 µm diameter, which matches the laser beam used in the experiments. The simulation considers L dots outside and m dots inside the region of the homogeneous electric field. The contrast at dot m is then calculated and compared with the experimental data.

The schematic setup for high-contrast switching of light is shown in Figure 4.11a. For contrast measurements of the fabricated device, two exemplary continuous wave (cw) lasers: $\lambda = 532\ \mathrm{nm}$ and $\lambda = 632.8\ \mathrm{nm}$ (a Nd:YAG solid state laser and a He-Ne gas laser) are used. The diffracted power could be controlled, achieving a maximum contrast ratio of $C = 511$ for $\lambda = 532\ \mathrm{nm}$ at $L = 4$, and $m = 13$ (see Figure 4.11b), and $C = 1236$ for $\lambda = 632.8\ \mathrm{nm}$ at $L = 1$, and $m = 15$ (Figure 4.11c). The observation of high contrast values despite the small L values suggests that the amplitude levelling occurs across just a few interactions with the waveguide grating. This rapid levelling is a consequence of resonances excited within the waveguide grating.

In addition to applications using continuous-wave (CW) lasers, there is significant interest in using broadband light instead of monochromatic light for several applications. Broadband light sources include not only classical incoherent white light, such as sunlight, but also lasers that produce ultrashort light pulses. Femtosecond laser pulses have a substantial spectral bandwidth of several nanometers. For instance, a 100 fs pulse at 800 nm centre wavelength has a bandwidth of approximately 5 nm, as determined by the time-bandwidth product[124] For extremely short pulses, on the order of just a few femtoseconds (comparable to only a few oscillation periods of the electromagnetic wave), the spectral bandwidth can extend to several tens or even hundreds of nanometers in the visible spectrum, essentially creating some kind of "white" laser light.

The ability to switch such broadband laser pulses fast and with high contrast would open up entirely new technological possibilities for numerous applications. To explore this potential, a series of proof-of-concept experiments that demonstrate the broadband nature of the Zero Diffraction phenomenon have been conducted.

In an initial experiment, a tunable femtosecond laser system was used. This system is based on a titanium-sapphire femtosecond laser with a pulse duration of 140 fs. The spectral width at a wavelength of 800 nm is approximately 10 nm. Using an optical parametric oscillator and frequency-doubling crystals, laser pulses can be generated across a wide range, from the UV region to the mid-infrared. Due to dispersion, the pulse duration in the UV-Vis range is around 200 fs, with a spectral width of approximately 5-10 nm. The experiments here have been conducted across various wavelengths in the visible spectrum, ranging from 480 to 640 nm.

As shown in **Figure 4.12**, interaction spots with the central waveguide grating (dots) are visible, similar to the results observed under cw (continuous wave) illumination. In this experiment, water electrodes were used again. When an electric field is applied, significant changes in the brightness of the dots can be observed, again similar to the experiments with cw lasers. However, there are two important differences.

First, it was observed that the electric field strength required to switch a dot from the state of zero diffraction to maximum coupling decreases as the dot index m increases. In simpler and more practical terms, dots with higher m blink at a higher frequency as the electric field strength increases compared to those with lower m, where here the term blink refers to repeated switching of a dot's optical appearance between a dark state (zero diffraction) and a bright state (maximum out-coupling) as the electric field is increased.

The second difference is that, unlike the experiments with cw illumination, no diffraction is observed. The dots do not result parallel laser beams that can be projected onto a scattering screen. Instead, they seem just to scatter light. One possible reason for this is the decreasing functionality of the waveguide grating as a resonator. Due to the extremely short pulse duration, the pulses have a spatial extension of only about 40-60 micrometers (for 140 fs – 200 fs pulse duration). So the laser pulses may not show maximum self-interference inside the waveguide grating. However, at this stage this explanation could not be verified by additional experiments yet.

In summary, these experiments still confirm that the proposed phenomenon can be observed over a broader range of wavelengths beyond the two cw wavelengths presented above. The experiments demonstrate the ability of the device to switch optical signals with higher spectral bandwidths (5-10 nm) compared to the narrowband cw lasers used previously.

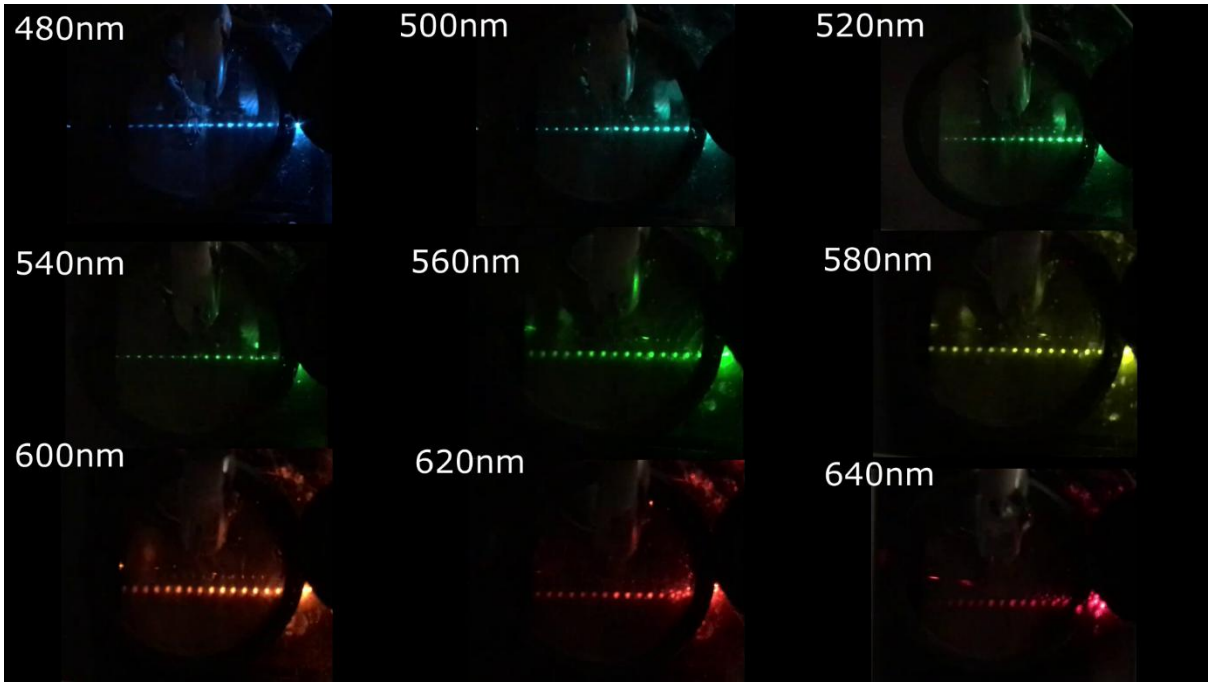

***Figure 4.12**: Experiments on waveguides showing Zero Diffraction using femtosecond laser pulses at various centre wavelengths across the visible spectrum.*

This capability is particularly remarkable when compared to many established phenomena such as BICs, which, due to their singular nature, are inherently unsuitable for switching light of finite spectral bandwidth. Therefore, these findings highlight the versatility and potential of zero diffraction for light switching and modulation technologies. If we continue along the path of increasing bandwidth, it becomes quite clear which type of light source will be tested in the final experiment: a continuous-wave (CW) white light source.

For these experiments, a laser-pumped Xenon plasma white light lamp is used, which has the advantages of its high optical output power and high radiance (power per area and solid angle). Unlike lasers, most white light sources exhibit a small coherence length (typically on the order of a few micrometers), usually making them less suitable for resonant, interference-based optical phenomena. However, in **Figure 4.13**, the zero diffraction waveguide is shown again from a similar perspective as in the previous figure, but now with white light coupled into it.

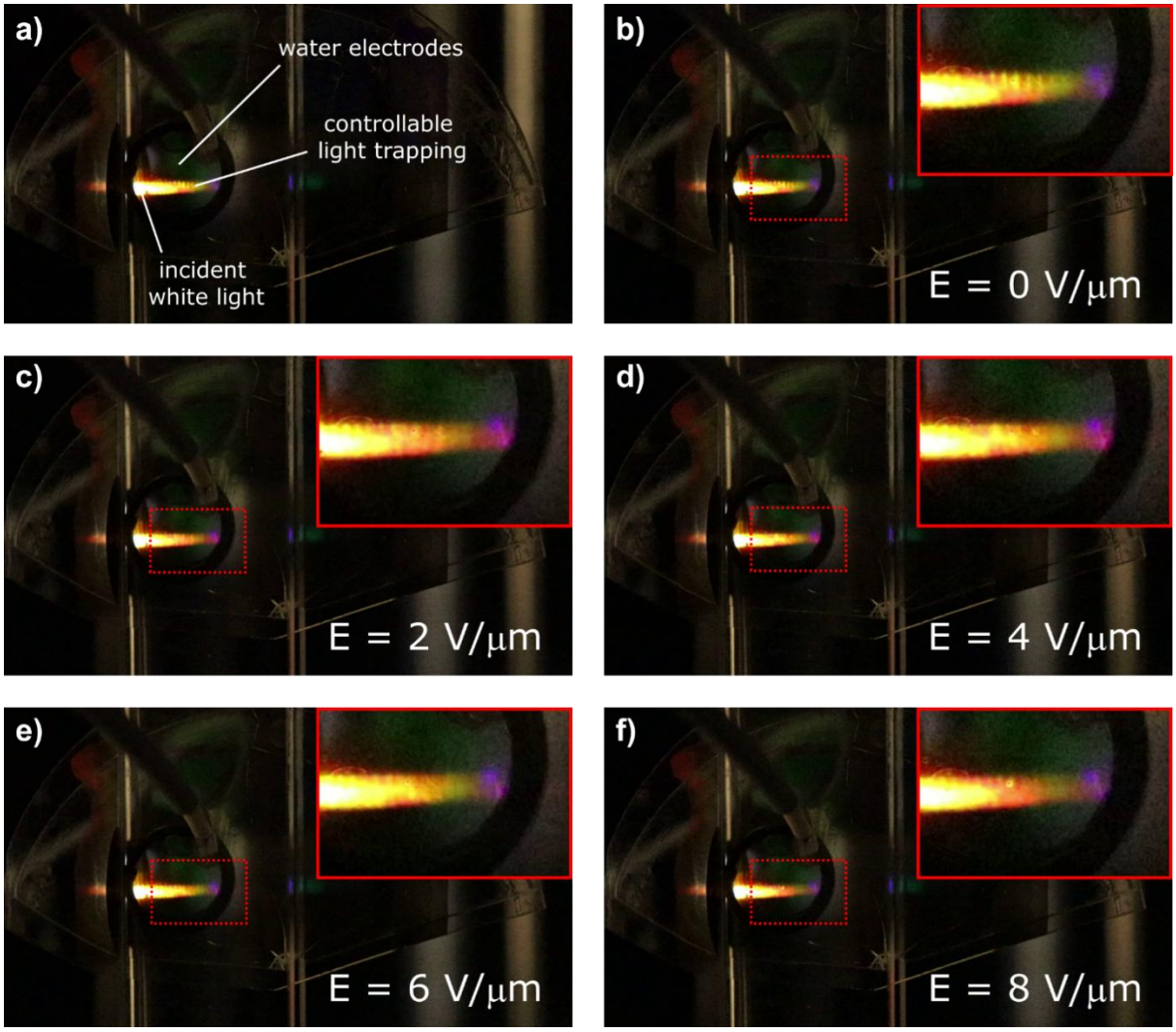

***Figure 4.13**: Experiments on the described waveguide using (incoherent) white light.*

An interesting observation is that while the dots are still visible (though stretched more in the vertical direction due to the beam shape), they seem to blur together, probably due to dispersion. While the scattered light appears white at the beginning (low m), more spectral components of the white light become visible for larger m. At high m, only violet light is scattered, with the remaining spectral components are likely already fully out-coupled. When an electric field is applied to the waveguide, it is observed that the distribution and colour of the scattered light change significantly, especially at high m values (see Figure 4.13c-f). The experiments demonstrate that the propagation properties can be significantly influenced by the applied voltage. This suggests that the waveguide could also be suitable for switching light, such as for trapping and de-trapping. This capability would be particularly exciting for applications in concentrated photovoltaics. A more detailed discussion of this point is provided in Chapter 7.

4.3. Chapter Summary

In summary, this chapter has introduced photonic waveguide structures designed to exhibit highly sensitive interactions between light and an optical structure in response to an external stimulus. Such a stimulus could be, for example, a change in the thickness of one or more waveguide layers, or a change in their refractive index. The goal is to develop optical waveguides for promising applications including sensing, optical modulation and switching, as well as optical interconnects e.g. for quantum technology.

First, the TE_1 node modes and their properties in symmetric waveguide gratings were introduced. In this configuration, it was demonstrated that there are significant advantages in terms of sensitivity compared to other modes (TE_0) and asymmetric waveguide geometries. However, one drawback is the limitation of sensitivity due to the finite thickness of the grating. Optimization can essentially only be achieved by further reducing the grating thickness, which is limited when approaching a single atomic layer. Also, the maximum interaction efficiency will strongly decrease for such ultra-thin gratings.

In the next step, these drawbacks were addressed to develop a concept that introduces an additional symmetry condition (regarding illumination) and, on the other hand, the leakiness of the waveguide grating. As long as the outer waveguide maintains its (total) reflective properties of a waveguide but is thick enough to avoid resonances, this results in a system with several advantages. These advantages lie particularly in using Gaussian beams enabling the (fast) switching of monochromatic laser light, as well as short laser pulses and even incoherent white light using the Pockels effect.

Chapter 5

Sensitive Plasmonic Waveguide Structures

In the previous chapter 4, optical waveguides were introduced whose sensitivity is based on photonic waveguide effects. This also includes waveguides designed for zero diffraction despite the incorporation of silver, because only TE polarization has been used. Thus, plasmonics effects do not contribute. The principle behind these concepts in Chapter 4 is to achieve large propagation lengths (low-loss propagation) of light in the waveguide, which then show high sensitivity to optical symmetry changes of the waveguide. However, due to these large propagation lengths and, in the case of zero diffraction, the requirement to avoid self-interference in the outer waveguide layers, these concepts are in the current stage rather suitable for macroscopic waveguides applications. Although, there are already promising miniaturization approaches by avoiding self-interference also in thin layers.[125]

A very common miniaturization approach lies in the use of plasmonic effects. As introduced in Section 2, plasmons enable strong localization of electromagnetic fields in nanoscale structures and are therefore of high interest in integrated optical applications[42]. This confinement can also lead to a significant local field enhancement by several orders of magnitude[42]. This is particularly beneficial when aiming to utilize NLO effects[43], also with relatively low optical power, which can be found in reports in the literature[126]. Beyond the confinement capabilities, plasmonics often offer significant advantages in terms of the necessary fabrication processes. For instance, a simple surface plasmon resonance (SPR) sensor essentially requires only one thin planar metal layer, when using prism coupling (Kretschmann configuration).[43] However, plasmonics generally has the drawback of high ohmic loss of conducting materials, despite the wide range of commercialized applications, in which these limited propagation lengths can be tolerated[42]. Typical propagation length of a surface plasmon polariton (SPP) at a silver-air interface is just a few tens of micrometers and the sensing performance is often rather limited.[42]

A highly promising approach to solving this problem is the two-dimensional arrangement of plasmonic nanoparticles to create a plasmonic metasurface. In these systems, which are

typically quite complex to fabricate, sharp resonances have been observed across various metasurface designs[127–130].

This section presents the results of plasmonic metasurfaces fabricated via the growth of silver nanoparticles (AgNPs) using a particularly facile method, the electroless deposition (ELD) technique, which has been introduced in chapter 3. The ELD technique will be investigated as a flexible, bottom-up approach for fabricating optical metasurfaces, which can exhibit features of engineered disorder. Therefore, metasurfaces are fabricated under various illumination condition, including the absence of controlled illumination, and their properties are characterized in the context of different fields of application.

5.1. Disordered Hyperuniform Metasurfaces

(The following section is based on journal paper 7 of the publication list.)

In this first section, the focus will be on the properties of metasurfaces fabricated both in the absence of illumination and under photonic excitation (direct illumination with light). In the first step, the ELD solution prepared according to section 3.1.1 is disposed on a glass substrate and the deposition of AgNPs is performed without illumination (in darkness). The deposition procedure is illustrated schematically in **Figure 5.1a**. After drop-casting the ELD solution onto the glass substrate the deposition is performed for a duration 20 minutes. After the deposition, the ELD solution is carefully removed from the surface using a pipette, and subsequently the sample is loaded into a de-ionized (DI) water bath to remove residues of the ELD solution.

After the cleaning step, the resulting metasurface is analyzed using scanning electron microscopy (SEM). A typical SEM image of a metasurface fabricated in darkness is shown in Figure 5.1b. The AgNP distribution shows a high particle density, with an average particle radius of approximately 41 nm, as depicted in the histogram shown in Figure 5.1c.

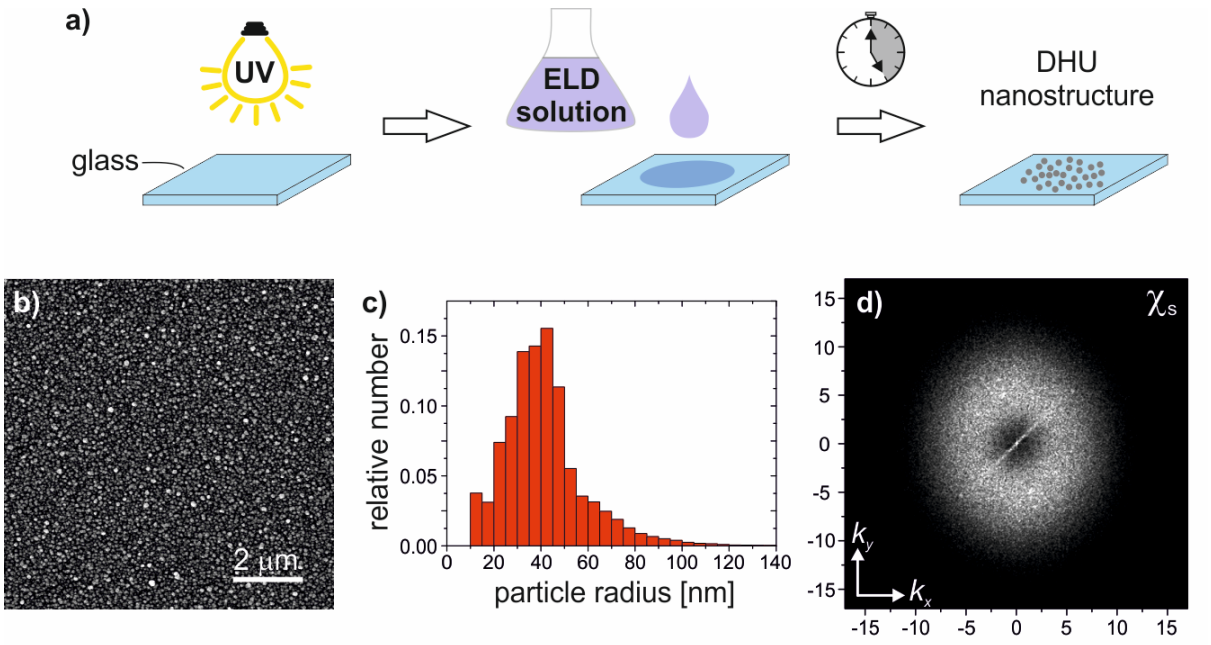

***Figure 5.1**. Overview of the metasurface fabrication process. a) A schematic illustration of the fabrication procedure; b) A typical SEM image of the resulting metasurface; c) Histogram depicting the size distribution of particles; d) k-space representation of the SEM image (here spectral density $\chi_S(k)$) from (b), revealing the disordered hyperuniformity of the particle arrangement (the unit is µm^{-1}).*

Although the particle assembly may appear random in the real-space SEM image, the spectral density, which has been derived from the SEM image (Figure 5.1d), reveals an engineered disorder. The characteristic 'donut' structure (bright region in Figure 5.1d) in the reciprocal space is typical for disordered hyperuniformity (DHU), which is defined by

$$\lim_{k\to 0} \chi_S(k) = 0.$$

While the general Fourier transformation is commonly used to analyse the surface morphology of nanostructures, the spectral density $\chi_S(k)$ provides a more practical tool for evaluating disordered hyperuniformity, following theoretical literature reports on the DHU in two-phase media.[84,131] The characteristic of the metasurface in the reciprocal space plays a crucial role for its optical application. The reason for this is that the reciprocal space properties are directly linked to the scattering behaviour of the metasurface[80]. This results in a spectrally selective scattering characteristic of the metasurface, thus the DHU metasurfaces are used in light management in solar cells[81,82,132].

Since the hyperuniformity metrics (as explained in section 2.6) including the position of the maximum spectral density $\chi_{S,max}$ are of high interest especially in light management applications, their control during the deposition process will be investigated in the following. In conventional bottom-up fabrication techniques, the resulting DHU is primarily governed by material composition and particle size, as is the case with self-assembly from suspensions[94]. However, the fabrication method presented here offers the advantage of in-situ control over the DHU by adjusting the deposition time as shown in the following.

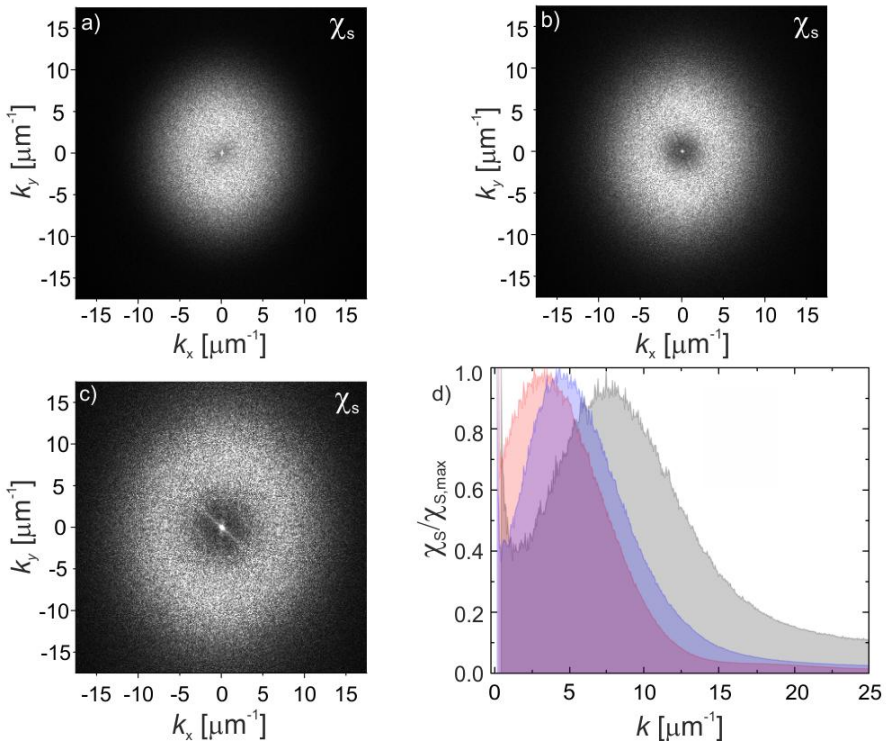

***Figure 5.2**: In-situ control of isotropic DHU during the deposition process. a) Spectral density $\chi_S(k)$ after 10 minutes of deposition; b) after 22 minutes of deposition; c) after 25 minutes of deposition; d) radial averaged and normalized spectral density, illustrating the evolution of DHU as a function of deposition time. This progression highlights the ability to tune the DHU characteristics via the deposition time.*

Figure 5.2 shows the spectral density $\chi_S(k)$ of metasurfaces after 10, 22, and 25 minutes of deposition. The maximum spectral density $\chi_{S,max}$ shifts from 3.3 µm^{-1} (a), to 4.6 µm^{-1} (b), and 7.8 µm^{-1} (c), demonstrating the tunability of the DHU throughout the deposition process. The corresponding degree of hyperuniformity H is 0.62 (a), 0.26 (b), and 0.17 (c), reflecting the improvement of hyperuniformity with deposition time. Figure 5.2d presents the radial

average of the spectral density, further illustrating the shift in $\chi_{S,max}$ as a function of the deposition time. However, the DHU features observed in the reciprocal space are rather broad and lack sharp transitions, which are typically necessary for a sensitive response of the waveguide. Therefore, the next step will be to introduce an additional degree of freedom in the process: the controlled illumination of the ELD solution during AGNP growth.

The metasurfaces are now fabricated under controlled illumination with laser light during the AgNP deposition. The laser illuminates the sample at a perpendicular angle of incidence and is circularly polarized. These conditions were chosen because a previous study found that illumination with linearly polarized light at a non-perpendicular angle leads to anisotropic features in reciprocal space, which are not compatible with the concept of (isotropic) disordered hyperuniformity presented so far[101].

Figure 5.3 shows the resulting metasurfaces using different laser wavelengths. The spectral density plots (Figure 5.3d-f) here display a characteristic 'dark' disk around the origin. It can be observed, that the radii K_i of these disks can be tuned by the laser wavelength and scale as $K_i = 1/\Lambda_i$, where Λ_i is the material wavelength of the laser in the ELD solution, given by $\Lambda_i = \lambda_{0,i}/n_{ELD}$, with $n_{ELD} \approx 1.336$.[133]

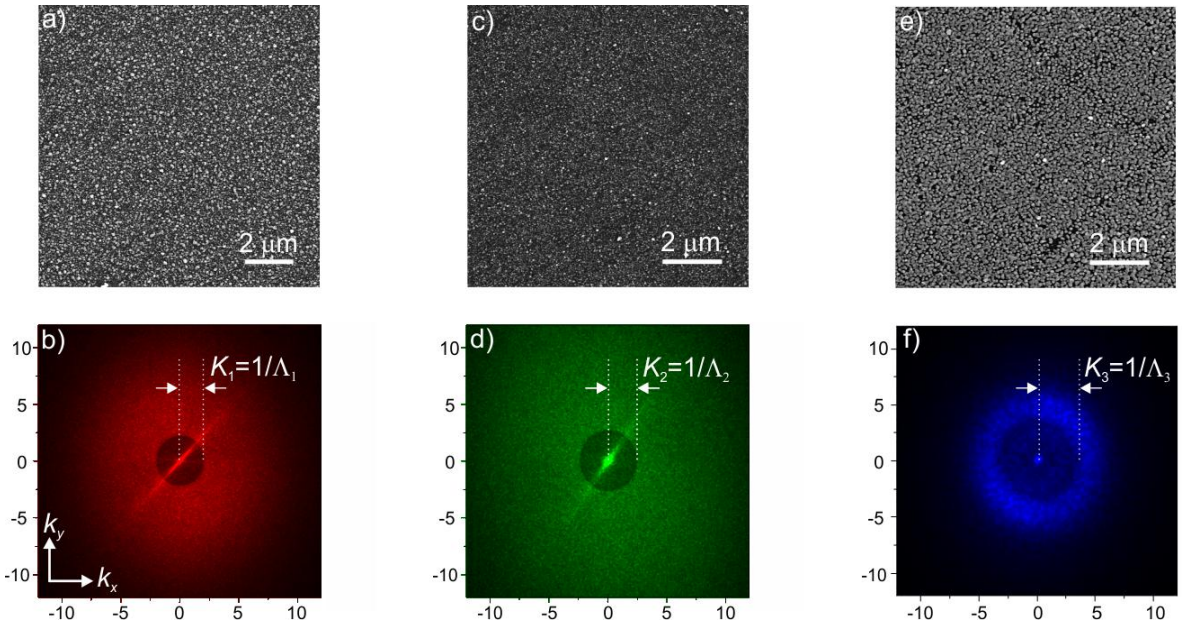

***Figure 5.3**: Stealthy DHU metasurfaces fabricated under incident light with varying wavelengths. a,b) Metasurfaces fabricated under illumination with 660 nm wavelength light;*

c,d) Metasurfaces fabricated under illumination with 532 nm wavelength light; e,f) Metasurfaces fabricated under illumination with 405 nm wavelength light (the unit is µm^{-1}).

In addition to the tunability of the DHU via the laser wavelength, compared to experiments conducted in darkness, the dark disks represent an even stronger form of hyperuniformity—stealthy disordered hyperuniformity. In stealthy DHU, the spectral density not only approaches zero as $k \to 0$, but vanishes within a finite circular region of radius K. The condition for stealthy DHU can be formally expressed as:

$$\chi_S(k) = 0, \qquad 0 < k \leq K$$

While theoretically, stealthy DHU requires the spectral density to be exactly zero within this dark disk, in real experiments, achieving this is challenging due to imperfections, missing structural elements, and finite size effects. Nonetheless, in this experimental work, it is referred to as stealthy DHU, as the spectral density shows a broad minimum.

Stealthy hyperuniformity is particularly valuable in application compared to standard disordered hyperuniformity (DHU) because it provides a sharp transition from high to low scattering probability at a specific wavelength. This characteristic makes stealthy DHU not only relevant for optical filters and light management but also promising for implementing highly sensitive optical devices as intended in this thesis, using the ELD technique,.

One observable feature in the spectral density is a bright, thin line crossing the centre of Figures 5.3b, 5.3d, and 5.3f, where the stealthy DHU condition is not fulfilled. Similar effects were observed in experiments conducted in darkness (see Figure 5.1 and 5.2), indicating that this phenomenon does not depend on the illumination properties. It could be found that this artefact in the k-space correlates with the direction in which samples were removed from the water bath. The effect also seems less pronounced for higher adhesion of AgNPs, such as those deposited under blue light. Therefore, this artefact can be attributed to the sample un-loading step. Previous research has shown that the morphology of AgNPs with low adhesion can be influenced by humidity and water.[96]

To further explore the opportunities provided by the light controlled growth of silver nanoparticles for metasurfaces, in the next step, the focus will be on another type of engineered disorder. So far, only metasurfaces with isotropic properties in reciprocal space

have been demonstrated. However, there also exists another types of DHU, which is known as anisotropic disordered hyperuniformity. This form of DHU, which has been described theoretically before, exhibits DHU in only one specific lateral direction, while in the perpendicular direction, DHU is absent[134,135]. In an earlier work, it was demonstrated that features in reciprocal space, produced through light-controlled growth, can be shifted by varying the incidence angle of light.[101] This is because the Fourier transformation generates signals at both positive and negative spatial frequencies, leading to the appearance of two features symmetric with respect to the plane of incidence for non-perpendicular incidence angles.

To achieve such conditions, a surface wave is now used as an incident wave – in particular surface plasmon polaritons (SPPs). The experimental setup for SPP excitation, as shown in **Figure 5.4a**, is implemented based on a Kretschmann configuration (prism coupling). First, the glass substrates are coated with a silver film of about 45 nm thickness. Then, the samples are mounted on top of the prism. A p-polarized laser is used to excited SPPs, showing a field overlap with the ELD solution, which enables coupling between SPPs and localized plasmons of the AgNPs during the growth. A more detailed description of the experimental conditions can be found in section 3.3.

Figure 5.4b displays a typical SEM image of the resulting metasurface. The spectral density shown in Figure 5.4c shows two dark disks, each of them similar to the results presented earlier in this section, but now symmetrically shifted along the k_x-axis. This shift, along with the radius K_{SPP} of the disks, is now determined by the SPP wavelength, where:

$$K_{SPP} = \frac{1}{\lambda_{SPP}}$$

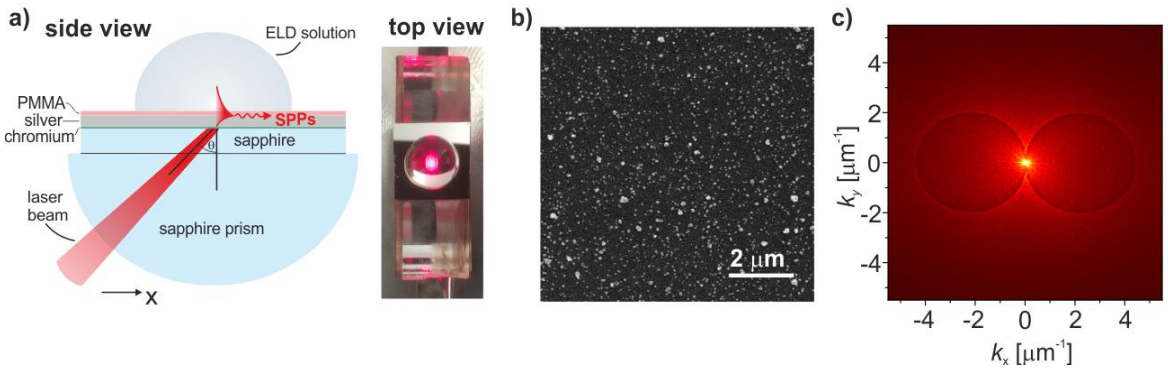

***Figure 5.4**: Light-controlled growth of metasurfaces via SPP excitation, resulting in anisotropic stealthy DHU. a) A schematic of the experimental setup (side view) and a photograph illustrating the top view. This configuration utilizes the Kretschmann setup to excite surface plasmon polaritons (SPPs) at the silver/PMMA interface; b) A representative SEM image of the fabricated metasurface; c) The corresponding spectral density, revealing anisotropic features induced by SPP excitation. The spectral density displays two dark disks symmetrically shifted along the k_x-axis, characteristic of anisotropic stealthy DHU.*

It can thus be concluded that metasurfaces can exhibit DHU when manufactured using the ELD method without controlled illumination. However, it has been demonstrated that controlled illumination provides additional control, enabling the creation of "stealthy" DHU. Moreover, the radius K of the dark disk in the reciprocal space, which significantly influences the scattering properties of the metasurface, can be precisely adjusted by the wavelength of the light used. In the final part, an experimental realization of anisotropic DHU was presented, showing that controlled illumination can be achieved not only with direct light illumination but also through other electromagnetic waves, such as surface plasmon polaritons (SPPs).

5.2. Disorder Engineering for Robust Optical Sensors

(The following section is based on journal paper 8 of the publication list.)

The goal of this section is to build on the findings from the previous section, demonstrating that light-induced growth of AgNPs can create metasurfaces with spectrally sharp features in the reciprocal space, and to translate this insight into a proof-of-concept realization of an optical sensor. The metasurfaces will therefore be fabricated in a similar way like for the samples showing anisotropic DHU. However, one essential concept remains to be added to process of implementation: utilizing the identical electromagnetic environment for both the fabrication of the metasurface and its subsequent use. In practice, the idea is to fabricate the metasurface under controlled illumination conditions with a specific light source and subsequently utilize the very same light source for probing it as an optical sensing device. Thus, after fabrication, the sample remains mounted in the setup without any further alignments to the arrangement. The difference from previous experiments in terms of experimental parameters lies in the deposition time, which has been reduced to approximately 5 minutes in the experiments shown here.To implement this concept in an

experiment, SPP waveguide samples have been fabricated using the method described in Section 3.2. The thickness of the silver film was chosen at $t_{Ag} = 54\ \mathrm{nm}$. SPP excitation along the Ag/PMMA interface is achieved using a Kretschmann configuration with a diode laser (λ = 660 nm, $P_0 = 70\ \mathrm{mW}$) and a semi-cylindrical sapphire prism (**see Figure 5.5**).

The laser beam is first p-polarized using a linear polarizer, and the incident angle is carefully adjusted to match the SPP resonance conditions, ensuring maximum photon-to-SPP coupling. Here, these resonance conditions were found under an incident angle of $\Theta_{in} = 54°$ for a laser wavelength of $\lambda_0 = 660\ \mathrm{nm}$. In addition, the sample was covered by a flow cell to continuously exchange the test analyte.

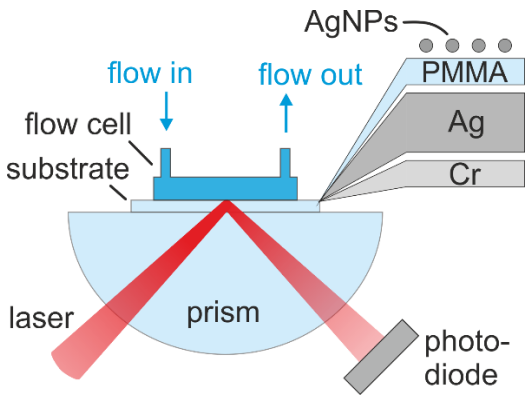

***Figure 5.5**: Sketch of the ATR configuration, which is used for the excitation of SPPs with an additional flow cell in order to change the RI of the analyte. The setup enables identical fabrication and probing conditions.*

To initiate the nanoparticle deposition, a water-based electroless deposition (ELD) solution is drop-cast onto the PMMA surface at the location of maximum optical power density ($I_{max} \approx 0.2\ \mathrm{W/cm^2}$). Throughout the deposition process, the reflected optical power is continuously monitored with a photodiode-based optical power meter (Thorlabs S151C). The flow cell contains two optical windows, so that the setup can be combined with the Michelson-interferometer described in Section 3.5 and thus the change of the refractive index can be monitored.

A simplified picture of the formation process of the metasurface can be drawn as follows. Initially, surface plasmon polaritons (SPPs) are scattered by surface imperfections of the planar films or randomly grown AgNPs. The scattered waves then interfere, and thus generate localized spots of enhanced electromagnetic field intensity. At these locations (highlighted as

red ellipses on the sample's surface in **Figure 5.6**), the growth rate of AgNPs is increased due to the energy delivered to the growing particles via absorption.

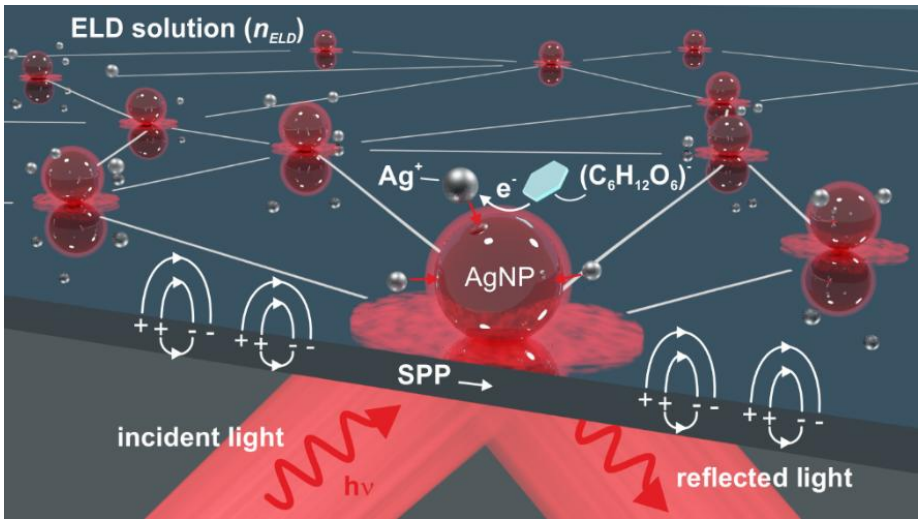

***Figure 5.6**: Graphical sketch of the simplified principle of plasmon-induced disorder-engineering.*

Although, the growth mechanism of the metasurfaces is not yet fully understood, it can be sketched by nucleation theory. According to this theory, AgNPs can spontaneously nucleate at random positions on the sample surface. However, at first these nanoparticles are thermodynamically unstable until they reach a critical radius. In the subcritical phase, particles compete with each other, and some may dissolve, as it is energetically favorable for silver atoms to leave small subcritical particles. However, for particles with sizes exceeding approximately 1 nm, localized surface plasmon (LSP) excitation becomes possible. These LSPs can efficiently absorb light and thus energy can be transferred to the particles, promoting further growth towards an overcritical size. Additionally, LSP excitation can enhance particle adhesion to the surface, reducing the critical particle size locally.

While AgNPs can also statistically grow to a stable size, positions with efficient LSP excitation—corresponding to local intensity hotspots—are energetically favoured for their growth. In the present setup, LSP excitation is facilitated by SPPs. Phenomena such as gap plasmons, which exhibit strong field enhancement within the dielectric spacer between silver particles and a silver film, may contribute to the energy exchange between LSPs and SPPs, thereby influencing the growth dynamics of the nanoparticles[97].

Returning to the simplified picture, once a nanoparticle exceeds the critical size, it becomes a highly efficient scatterer of electromagnetic waves (both photons and SPPs), resulting in the formation of localized intensity hotspots. This illustrates the capacity of this method for real-time nanostructuring (depicted by white lines between AgNPs, indicating the formation of some kind of network) to adapt to the electromagnetic environment, characterized by a specific refractive index (RI) and SPP wavelength, as well as the particular wave-fronts of a well-aligned light source.

After the deposition process, the ELD solution is carefully removed from the surface of the sample. The flow cell is initially filled with deionized (DI) water, setting the refractive index of the analyte solution at approximately $n_w = 1.333$ at the start of the experiment. Ethanol (n = 1.36) is then gradually added to the water from an external mixing container. This mixture offers several advantages: first, ethanol can be mixed with water in any ratio, which is crucial because the formation of an emulsion would significantly complicate interferometric measurements due to wave-front disturbances. Additionally, ethanol is transparent and has a refractive index very close to that of water. This allows for fine adjustments in the refractive index, enabling the precise characterization of subtle optical features.

The resulting reflectance data of the sample is presented in **Figure 5.7**. Starting at n_w, the reflectance follows a SPP resonance curve. At the specific position corresponding to the RI of the ELD solution, a sharp, narrow peak in reflectance is observed. At this position, the reflectance increases from approximately 44% to 52% (see Figure 5.7).

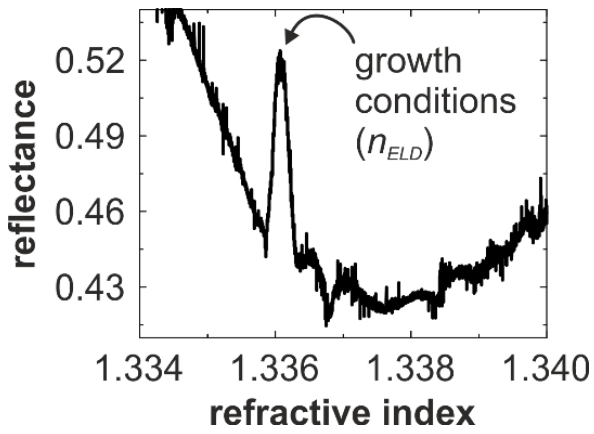

***Figure 5.7**: The measured reflectance curve dependent on the RI of the analyte mixture (water/ethanol mixture) after the AgNP deposition, which shows the resulting structural feature (@$n = n_{ELD}$) within the SPP resonance curve.*

Analyzing the interferometer data results in a full width at half maximum (FWHM) of the feature of $\Delta n \approx 3 \cdot 10^{-4}$. Remarkably, this FWHM is about two orders of magnitude narrower than the theoretical width of a typical SPP resonance. To link this width of the feature to a performance measure for an optical sensor, it is common to use a Figure of Merit*, which evaluates a change in a certain measurement quantity (e.g. reflection) over a measurement parameter (here the refractive index) in relation to a certain value of that quantity. Mathematically, the FoM* can be expressed as:

$$\mathrm{FoM}^* = \frac{1}{P}\left|\frac{\partial P}{\partial n_{analyte}}\right|,$$

where P is some measured optical power signal (here the reflected laser power) at a fixed wavelength λ_0, $n_{analyte}$ is the refractive index of the analyte mixture surrounding the metasurface, and $\partial P/\partial n_{analyte}$ is the change of the measured power with respect to a change in $\partial n_{analyte}$.

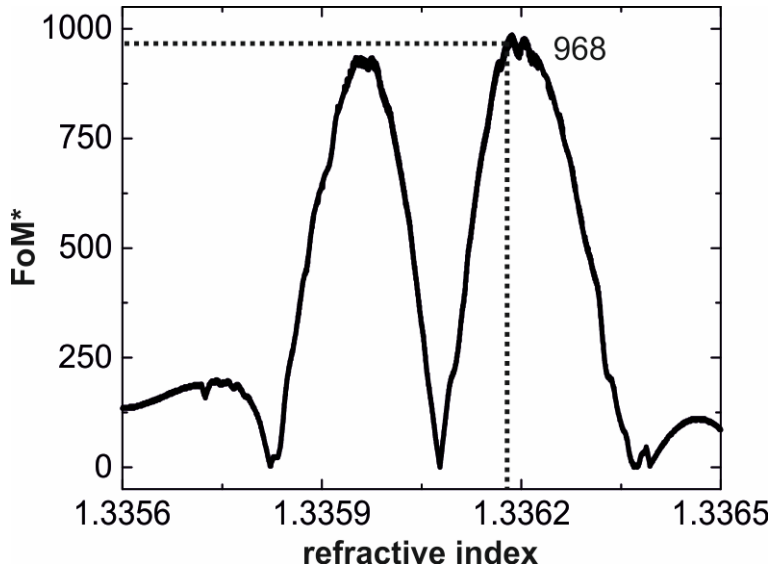

***Figure 5.8**: The FoM* of the optical sensor versus the refractive index of a test analyte.*

With a maximum FoM* of 968 (**Figure 5.8**), the self-optimized optical sensor achieves performance comparable to more sophisticated plasmonic sensors reported in the literature, while utilizing a much simpler fabrication method compared to techniques like e-beam lithography.

To explore the origin of this sharp feature, further investigations were conducted, starting with characterizations of the shape and spatial distribution of the AgNPs using scanning electron microscopy (SEM). **Figures 5.9** show typical scanning electron micrographs of the grown metasurfaces and AgNPs. In this case as well, the spatial distribution of the AgNPs appears random in the real-space images. However, the Fourier-transformed electron micrograph (FTEM), which is a powerful tool to investigate the morphology of nanostructures, reveals a more complex pattern that shows features of engineered disorder of the AgNPs. Because the deposition time is decreased, the resulting metasurfaces does no longer show features of DHU. In fact, in the FTEM (Figure 5.9c), two distinct dark rings, hereinafter referred to as "structure rings," are observed. These structure rings touch each other at the origin (x^{-1}, $y^{-1} = 0$).

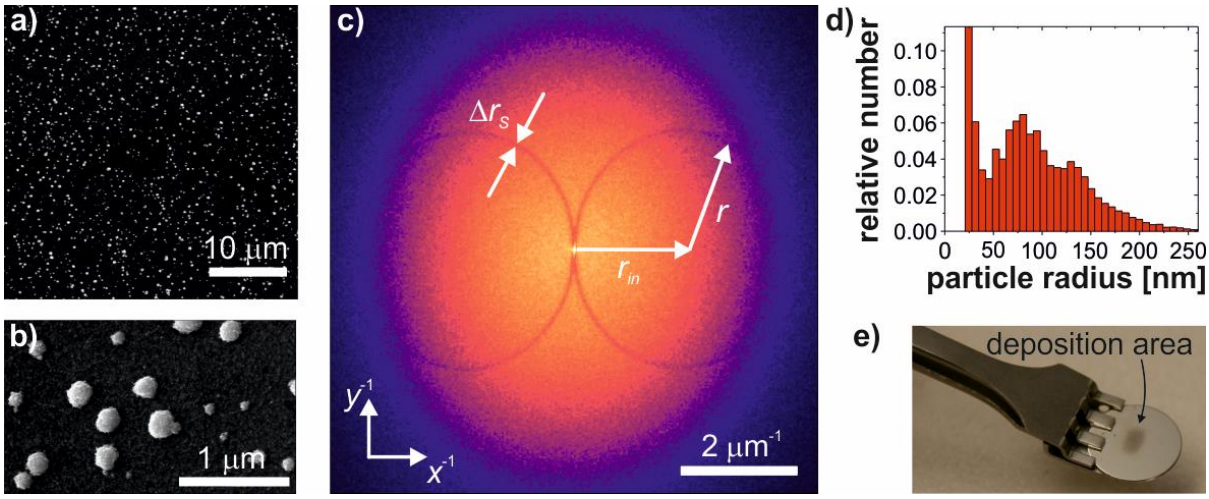

***Figure 5.9**: Characterization of the Nanostructure. a) Scanning electron micrograph showing the overall nanostructure in real space; b) High-magnification electron micrograph revealing the detailed nanoscopic features of the structural elements; c) Fourier-transformed electron micrograph displaying two distinct dark rings in k-space, referred to as "structure rings"; d) Histogram of the relative number of nanoparticles as a function of their radii; e) Optical image of the sample after the deposition of AgNPs, highlighting the visible changes post-fabrication.*

Similar but less pronounced features have been reported in a previous work under photonic excitation on a plane glass substrate without the use of SPPs[101]. In those cases, it was found that such an experiment results in a mirror-symmetric shift (r_{in}) of two rings in the reciprocal space along the x^{-1}-axis. This shift r_{in} corresponds to the in-plane wave number of the incident electromagnetic wave. Furthermore, the radius of the rings (r) refers to the scattered waves. However, in all experiments involving surface plasmon polariton (SPP) excitation, the structure rings consistently touch at the origin, with the condition

$$r_{in} = r = 1/\lambda_{SPP}$$

This indicates that SPPs dominate the distribution of AgNPs during their growth. Notably, no photonic features are observed in the FTEMs. The particle radius covers a relatively broad range with an average particle radius of 92 nm (Figure 5.9d). Furthermore, Figure 5.9e presents an optical image of the sample after AgNP deposition. At the centre of the sample, an elliptical region with a greyish scattering is visible, marking the deposition area of the metasurface. In contrast, the surrounding area retains its mirror-like appearance as before the AgNP deposition.

Next, the link between the features in the k-space and the optical response of the metasurface are discussed. Considering the structure rings, information about all electromagnetic wave involved is permanently stored in the metasurface via the spatial distribution of AgNPs. The dark structure rings observed in the FTEM suggest a reduced scattering probability when excited with the same SPP wavelength that was used during the fabrication procedure. In our configuration, this reduced forward scattering into free space results in enhanced back reflection under the same growth conditions.

If the refractive index (RI) deviates from the growth conditions, and thus the SPP wavelength shifts, the dark structure rings in the FTEM remain unchanged. However, the changed conditions can be represented again by rings in k-space, hereinafter termed as "wave rings". The radii of these thereby scale linearly with the RI of the analyte mixture. Then, the optical reflection can be modeled by an overlap function of the structure rings and the wave rings.

To simulate the overlap function of the structure and the wave rings, the amplitude profile of the rings $w(r)$ is modeled by a Gaussian distribution

$$w(r) = \frac{1}{\sigma\sqrt{2\pi}} \cdot e^{-\frac{1}{2}\left(\frac{r-r_{SPP}}{\sigma}\right)^2},$$

where σ is the standard deviation ($\sigma = FWHM \,/\, 2\sqrt{2ln2} \approx FWHM \,/\, 2.355$), extracted from the laser divergence ($FWHM_W = \Delta r_W$) and the corrected width of the structure rings from the FTEM ($FWHM_{S,C} = \Delta r_{S,C}$). In **Figure 5.10a**, the width of the wave rings was artificially increased (Δr_W^*) for a suitable visualization of the model.

For the calculation of the overlap function, the values for $\Delta r_{S,C}$ and Δr_W were taken.

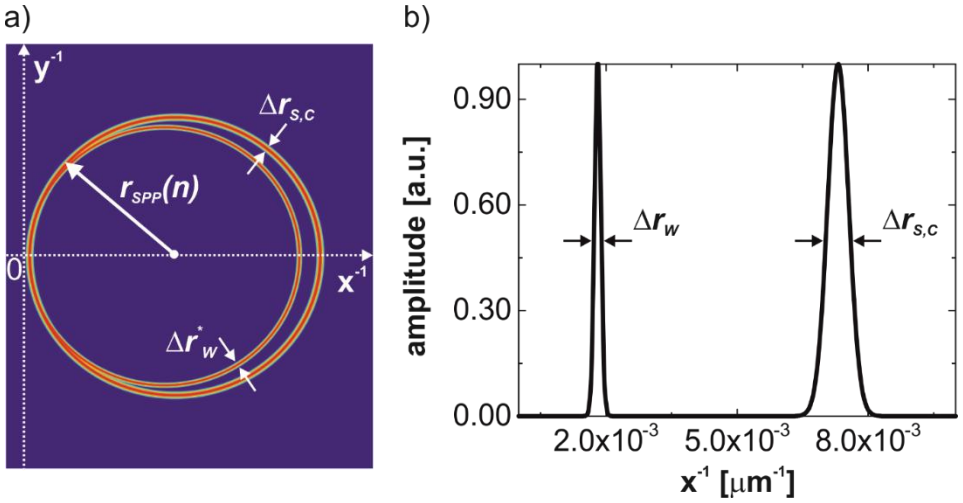

***Figure 5.10**: Model for the calculation the overlap function, a) modeled structure rings and wave rings; b) amplitude profiles of the two rings.*

One structure ring is modeled and shifted along the x^{-1}-axis to the center coordinates (x_S^{-1}; y_S^{-1}):

$$\begin{cases} x_S^{-1} = r_{SPP}|_{n=n_{ELD}} + \frac{\Delta r_S}{2} \\ y_S^{-1} = 0 \end{cases}.$$

For every value of n, the radius of the structure ring stays fixed at $r_{SPP}|_{n=n_{ELD}}$.

One wave ring in the reciprocal space is modeled with the radius r_{SPP} and the center coordinates (x_{SPP}^{-1}; y_{SPP}^{-1}):

$$\begin{cases} x_{SPP}^{-1}(n) = r_{SPP}(n) + \frac{\Delta r_W}{2} \\ y_{SPP}^{-1} = 0 \end{cases}.$$

The simplification of using only one structure ring and one wave ring can be done as both the structure rings and wave rings are mirror symmetric with respect to the y^{-1}-axis. The radius of the wave ring is varied dependent on n following the function $r_{SPP}(n)$. In this way, the

wave ring 'scans' the structure ring. At every refractive index from $n_w = 1.333$ to $n_F = 1.339$ with a step size of $2 \cdot 10^{-5}$, the overlap between the wave and the structure ring is calculated. For this calculation, we define a fine-coarse grid in the reciprocal space. Each cell of the grid has a size of $5.2 \cdot 10^{-5} \cdot 5.2 \cdot 10^{-5}$ µm^{-2}. Then, for each cell with the center coordinates x_i^{-1}, y_j^{-1}, we calculate the amplitude values $a_{ij}$and b_{ij} of the structure ring and wave ring, respectively. This procedure defines two matrices:

$$A = \begin{bmatrix} a_{11} & \cdots & a_{1m} \\ \vdots & \ddots & \vdots \\ a_{m1} & \cdots & a_{mm} \end{bmatrix}; \; B = \begin{bmatrix} b_{11} & \cdots & b_{1m} \\ \vdots & \ddots & \vdots \\ b_{m1} & \cdots & b_{mm} \end{bmatrix}$$

Then, the overlap *S* of the structure and the wave ring is calculated as a sum of all elements $c_{i,j}$ of the matrix *C*:

$$C = A \circ B = \begin{bmatrix} a_{11}b_{11} & \cdots & a_{1m}b_{1m} \\ \vdots & \ddots & \vdots \\ a_{m1}b_{m1} & \cdots & a_{mm}b_{mm} \end{bmatrix}$$

$$S = \sum_{i=1}^{m} \sum_{j=1}^{m} c_{i,j}.$$

Afterwards, we normalized the resulting overlap function to the maximum value of *S* (maximum overlap). The resulting peak in the overlap function has a width (FWHM) of $\Delta n_s \approx 2.9 \cdot 10^{-4}$.

Therefore, as the RI changes, the new wave rings no longer perfectly align with the structure rings. Consequently, scattering increases compared to the original growth conditions, the reflection is reduced. To calculate the overlap function, the widths of the wave rings (for the wave rings also as a function of the refractive index) and the structure rings in reciprocal space need to be determined.

In turn, the width of the wave rings is primarily governed by the laser beam's divergence. The measured laser divergence corresponds to a momentum width of the wave rings of approximately $\Delta r_w \approx 1.72 \cdot 10^{-4}$ µm^{-1} (FWHM).

For the structure rings, it is not sufficient to just measure the width of the structure rings from the FTEMs directly. The reason for this is that according to Heisenberg's uncertainty principle, the resolution of features in reciprocal space is constrained by the size of the observation window in real space (momentum-space uncertainty). Considering our experiment, the

observation window in the scanning electron microscope is much smaller compared to the area of the metasurface, which is illuminated during the optical experiment. Since it is technically not feasible to record an image in the SEM of the size of the entire illuminated area while still being able to distinguish individual particles, it is necessary to find a correction formalism to determine the actual width of the structure rings.

Based on the uncertainty principle, the measured structure ring widths should theoretically scale with $1/d$, where d is the edge length of a square-shaped observation window. To verify this assumption, the full width at half maximum (FWHM) of the structure ring width (Δr_s) was measured for observation windows ranging from 92 × 92 µm² to 148 × 148 µm². This was achieved by subdividing a single SEM image, with an area of 148 × 148 µm², into smaller sections. In **Figure 5.11**, the corresponding values for Δr_s depending on d are displayed.

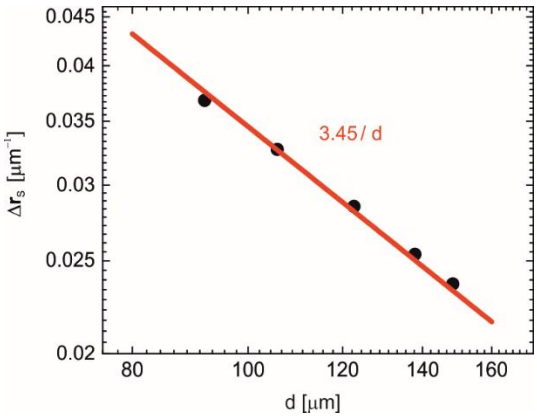

***Figure 5.11**: The measured structure ring widths fitted by a function B/d with B as fitting parameter displayed in a double logarithmic scale.*

The data reveals that the structure ring widths become narrower as d increases, approximately following the relation $\Delta r_s = 3.45/d$ (indicated by the red line in Figure 5.11). Therefore, to determine the corrected structure ring width $\Delta r_{s,c}$, the length D corresponding to the entire area A illuminated by the laser, is defined as $D = \sqrt{A}$. For an illumination area of $A \approx 33.4$ mm², the corresponding corrected width of the structure ring is $\Delta r_{s,c} = \frac{3.45}{\sqrt{A}} \approx 5.97 \cdot 10^{-4}$ µm².

Figure 5.12 shows the comparison between the measured reflectance curve (Figure 5.12a) and a simulated curves (Figure 5.12b) of the overlap function (red) and the underlying SPP resonance (black).

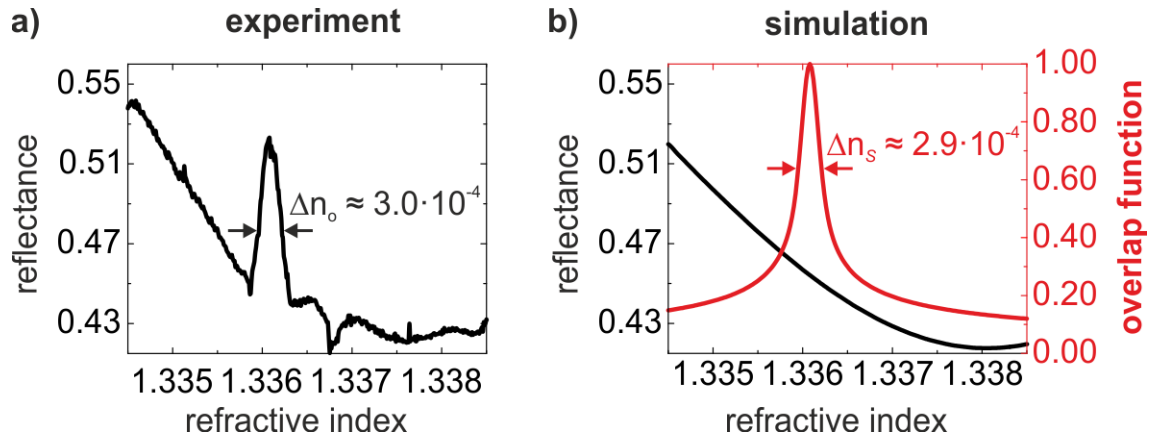

***Figure 5.12**: A comparison of experiment and simulation to understand the mechanism behind the sensitivity to changes in the electromagnetic environment of the metasurface. a) Reflectance measurements of the sample as a function of the RI, closely aligned with the growth conditions; b) The resulting overlap function (red curve) showing a pronounced peak at the RI corresponding to the growth conditions, along with the underlying fitted SPP resonance (black curve).*

As shown before, the measured reflectance exhibits a distinct feature at the refractive index (RI) corresponding to the growth conditions of the structure. The experimental curve is shown again for better visual guidance for the reader when comparing with the simulation. To model the SPP resonance curve after the deposition of AgNPs, the additional losses introduced by the metasurface have to be considered. To account for this, a lossy effective medium layer on top of the PMMA film was introduced (see **Figure 5.13**).

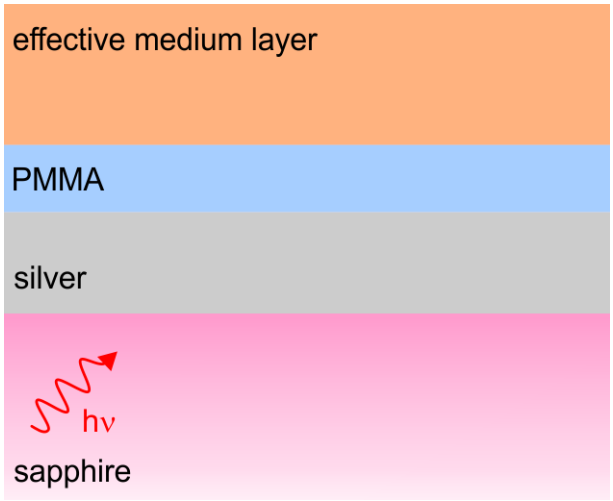

***Figure 5.13**: Stack used for the RCWA simulations with an additional 200 nm thick effective medium layer on top of the PMMA to simulate scattering loss of the metasurface by absorption loss of the effective medium layer.*

The complex refractive index of the effective medium layer $\underline{n_{el}}$ was then fitted to the experimental data, resulting in $\underline{n_{el}} = 1.3381 + i \cdot 0.0051$. A fit based on a pure SPP resonance, treating the structure as an effective homogeneous layer, is shown in Figure 5.12b (black curve), alongside the overlap function (red curve). The origin of this fitted SPP characteristic is shown in **Figure 5.14**.

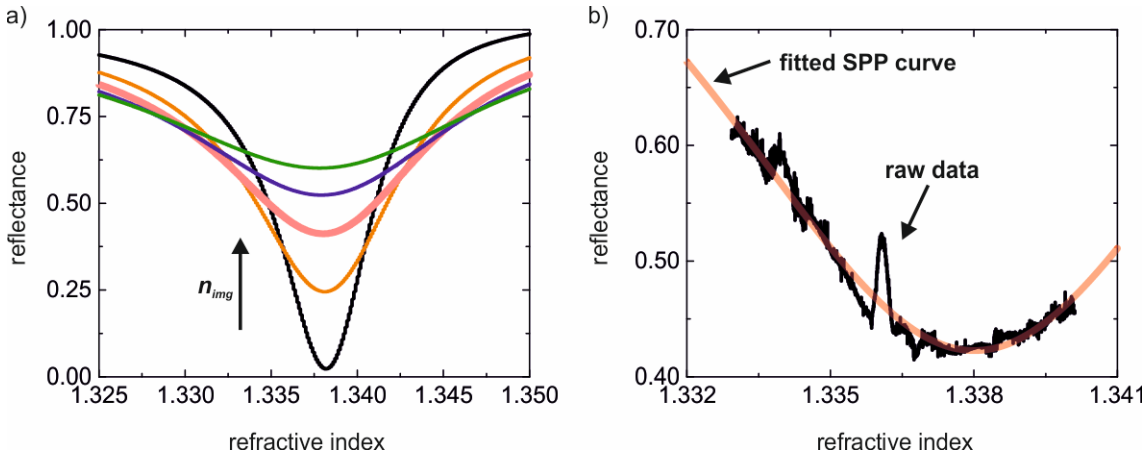

Figure 5.14: Fit of the SPP resonance curve. *a) reflectance for different imaginary part n_{img} of the effective layer; b) fit to the experimental data.*

In summary, the width of the peak observed at the growth conditions is determined to be $\Delta n_s \approx 2.9 \cdot 10^{-4}$ (FWHM). Together, these two components—the SPP resonance fit and the overlap function—are concluded to describe the overall optical response of the metasurface. A key aspect in the discussion of sensor performance is the link between high *sensitivity* to the target events (a "good" feature of a sensor) and the low *tolerance* for misalignments between the sensing structure and the light source (a "bad" feature of a sensor). The principle underlying this discussion is that designing an optical sensor with extremely high sensitivity (such as a very narrow spectral feature) inherently reduces its tolerance for misalignments and fabrication imperfections. For instance in the case of the sensors presented in this chapter. It has been observed during the experiments that even minor mechanical misalignments following the deposition process caused the loss of the structure's functionality. In practice, this means that the sharp spectral feature could not be

observed anymore. To assess the tolerance for such misalignments, the overlap function between the structure rings and the wave rings was calculated again while varying the incident angle of the probing light in both the azimuthal and polar directions. **Figure 5.15** illustrates the tolerance of the maximum overlap between the structure and wave rings in response to angular misalignments as well as changes in the wavelength of the light source.

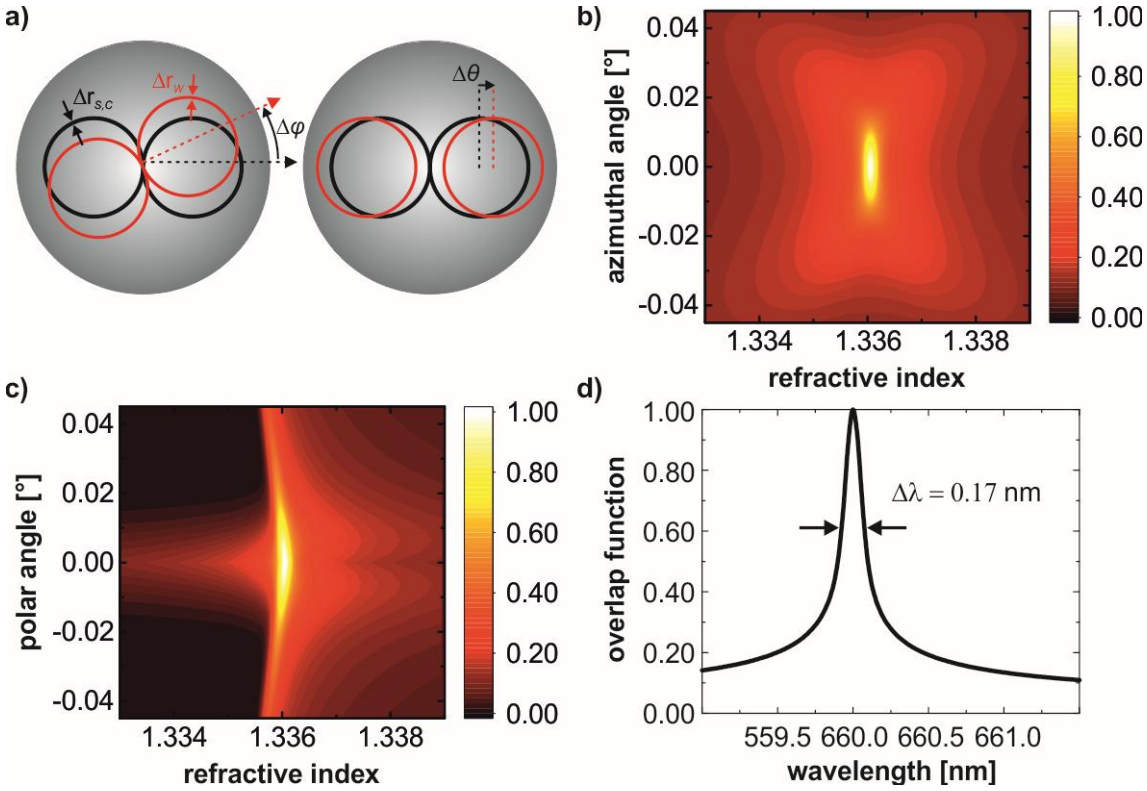

***Figure 5.15**: Tolerance to mechanical misalignments and sensitivity to changes in probing wavelength. a) Illustration of the principle used to derive the overlap function in relation to mechanical misalignments in the azimuthal and polar angles; b), c) Impact of azimuthal angle ($\Delta\varphi$) and polar angle ($\Delta\theta$) variations on the overlap function between the structure and wave rings; d) Overlap function as a function of the incident wavelength (λ), demonstrating sensitivity to changes in probing wavelength.*

The simulation results in Figure 5.15 show that the overlap between the structure and wave rings (defining the sharp resonance feature) exhibits a low tolerance to mechanical misalignments in both the azimuthal and polar angles. In detail, the maximum overlap decreases by approximately 50% for a misalignment of $\Delta\varphi = 0.012°$ in the azimuthal direction and $\Delta\theta = 0.024°$ in the polar direction. However, achieving high sensitivity to refractive index (RI) changes requires a significant overlap between the structure and wave

rings. In separate fabrication and probing scenarios, this necessitates extremely precise alignment in the order of 0.01°. Such precision is highly challenging especially for compact or even integrated optical systems and in practice rather restricted to experiments in the laboratory. However, in the context of this thesis, the exceptionally low tolerance for misalignments of the disorder-engineered metasurface sensors highlights the advantage of instantaneous alignment during metasurface fabrication. This inherent alignment eliminates the need for precise post-process alignment steps, which makes it compatible also with integrated optical devices and systems. In addition, Figure 5.15d highlights the spectral sensitivity and thus again also the tolerance for mismatches in the wavelength of the light source. It is important to note that characterizing this phenomenon spectrally requires a sampling light source that closely matches the one used during sample preparation, particularly in terms of coherence and radiance. However, even with monochromatic probing, the metasurface can address a wide range of refractive indices (RI). For instance, spatial variations in the effective refractive index of the SPP mode during growth can induce corresponding shifts in the observed features, depending on the position on the sample. These variations may result from a refractive index gradient in the ELD solution or even electro-optic effects in a nonlinear material near the surface.

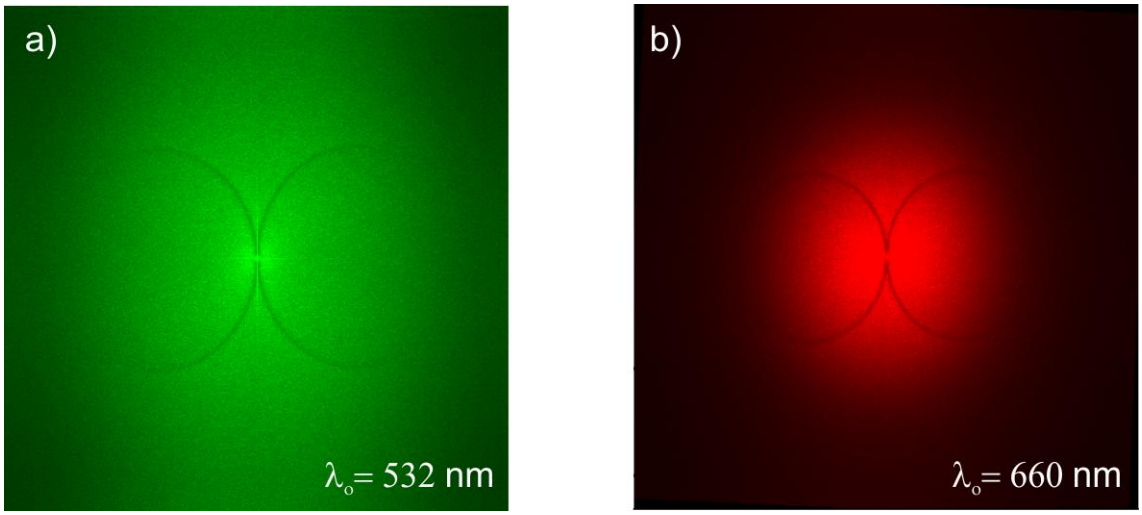

***Figure 5.16**: FTEMs of metasurfaces fabricated with two different laser wavelengths.*

Similarly to the experiments described in the previous section, structure rings can also be generated using different wavelengths. The radii and horizontal shifts change in response to changes in wavelength, eventually forming structure rings that touch at the y^{-1}-axis (**see Figure 5.16**).

5.3. Harnessing Short-Range Surface Plasmons via Disorder-Engineered Metasurfaces

(The following section is based on journal paper 6 of the publication list.)

In the previous section, it was shown that depositing AgNPs under controlled illumination conditions can create an optical metasurface containing sharp spectral features, which can be utilized in an optical sensor. It appears that the propagating surface plasmons (SPPs) interact with localized surface plasmons (LSPs) supported by the AgNPs, which provide an optical response as an ensemble. The fact that the structure rings, which primarily define the functionality of the structure, appear dark in the FTEM suggests that under these conditions, there is a suppressed interaction between propagating and localized plasmons under growth conditions. As described in the fundamentals chapter, plasmonic states typically exhibit relatively short propagation lengths (or lifetimes). This is primarily due to significant losses caused by ohmic losses or scattering. A shorter propagation length generally leads to broader resonance curves. It is therefore remarkable that, despite considering the high loss of the plasmons, it is possible to generate such a sharp spectral resonance feature. Thus, from the findings of the previous section, it can be concluded that the sharpness of the spectral features is no longer determined by the propagation lengths of the individual resonances. Instead, as demonstrated, it is governed by the size of the coherently illuminated area. Building on this, it is promising to explore phenomena that may exhibit higher losses—typically limiting their conventional applications—but offer other advantages that could be beneficial for sensitive waveguides.

As introduced in the fundamentals chapter, reducing the thickness of the silver layer can lead to the hybridization of the two plasmon modes at the interfaces of the metal film. As described, these hybridized states are commonly referred to as short-range and long-range plasmon polaritons, due to their respective shorter and longer propagation lengths. Due to their strong field enhancement and short wavelengths, short-range surface plasmon polaritons (SR-SPPs) have been utilized in various applications such as sensing,[136] focusing,[137,138] and high-resolution microscopy.[139]. Recently, the formation of hybrid bound states in the continuum (BICs) has also been explored when SR-SPPs are coupled to photonic waveguide modes.[108] Despite their potential, SR-SPPs have garnered less attention compared

to long-range SPPs (LR-SPPs)[140]. One reason for this is that SR-SPPs, due to their high momentum, are challenging to excite using photons. In this section, the influence of the hybridization of the two SPP modes propagating along the two interfaces of the silver film will be examined with the goal to utilize hybrid plasmons for the fabrication of the metasurfaces.

For the sake of completeness, first a comparatively thick silver film ($t_{Ag} = 56$ nm) on a sapphire substrate is mounted on the ATR setup (see **Figure 5.17**). The laser is then aligned with respect to the SPP resonance conditions ($\Theta_{in} = 54°$ @ $\lambda_0 = 660$ nm). The AgNP deposition is conducted according the description in the previous section. A typical scanning electron micrograph and the corresponding FTEM are shown in Figure 5.17b,c. Here, both r_{in} and r_s can be attributed to the SPP_a mode propagating along the silver/PMMA interface that can interact with the metasurface as $r_{in} = r_s = 2.14\ \mu m^{-1} = {}^{1}/_{\lambda_{SPPa}}$. The corresponding effective index of the SPP_a mode is given by $n_{SPPa} = {}^{\lambda_0}/_{\lambda_{SPPa}} = 1.41$. Features of the SPP_b mode propagating along the prism/silver interface are not observed in this experiment. As the electromagnetic field decays rapidly inside the silver film, it does not interact with the metasurface because of the thick silver film. However, in the next step the thickness of the silver film t_{Ag} be reduced down to a thickness where both SPP modes show a significant field overlap inside the silver film causing hybridization.

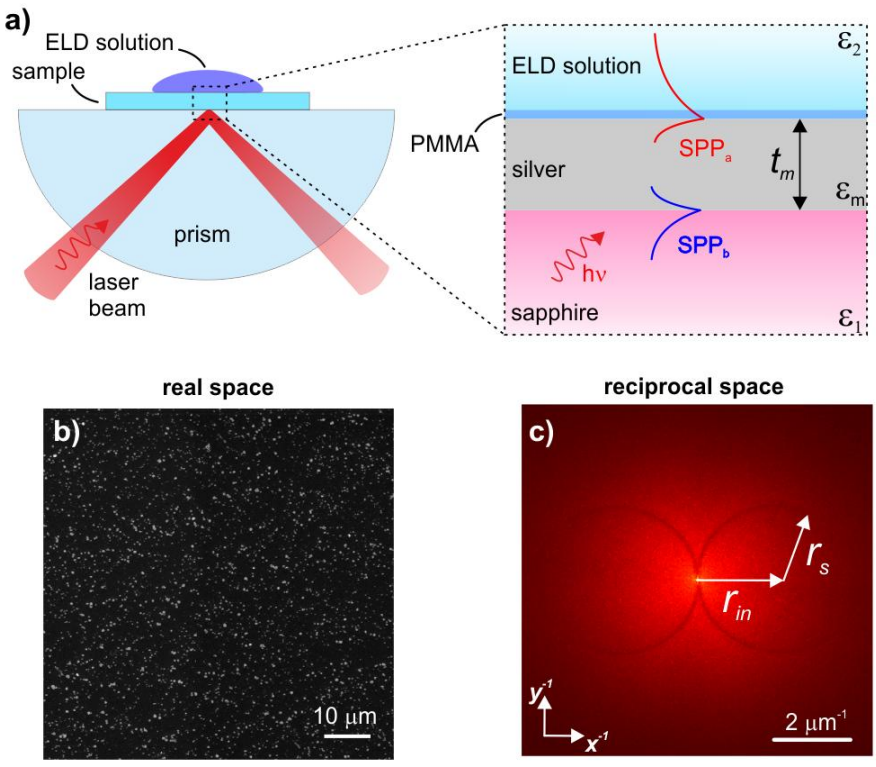

***Figure 5.17**: Experimental setup and SEM analysis of disorder-engineered metasurfaces on thick silver films ($t_{Ag} = 56\,nm$). a) Schematic of the experimental setup used in the experiments, along with the stack geometry (inset). The diagram highlights the two plasmon modes propagating at the upper and lower interfaces of the silver film (SPP_a and SPP_b); b) A typical SEM image of the fabricated metasurfaces; c) Fourier-transform of the SEM image, revealing the engineered disorder of the metasurfaces. The white arrows indicate the horizontal shift (r_{in}) and the radius (r_s) of the structure rings.*

In the first experiment, the thickness of the silver film is reduce to $t_{Ag} = 25$ nm. The resulting layer stack, along with qualitative one-dimensional field profiles of the long-range (LR SPP, red) and short-range (SR SPP, blue) SPP modes, is shown in **Figure 5.18a**.

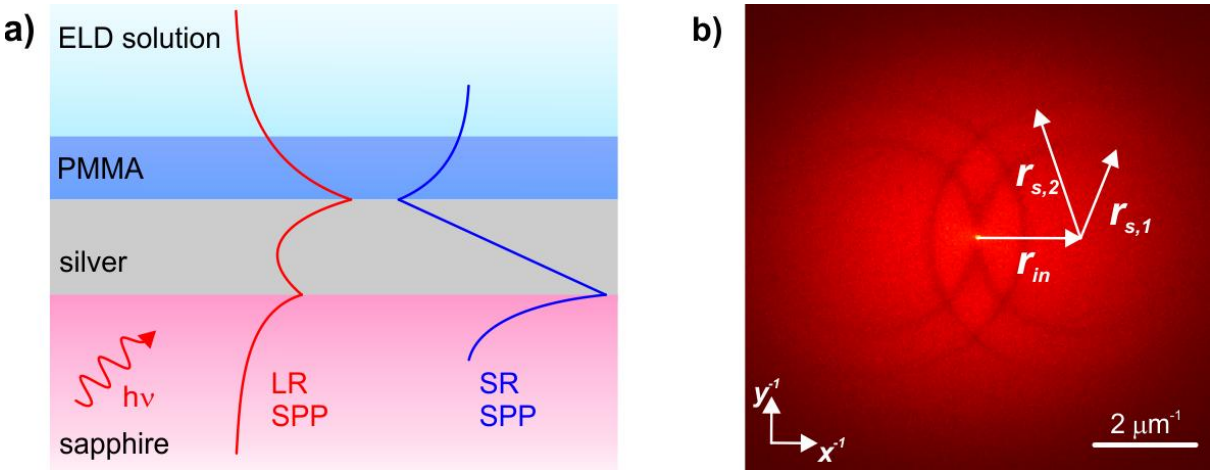

***Figure 5.18**: Disorder-engineered metasurfaces deposited on thin silver films ($t_{Ag} = 25$ nm). a) Schematic of the layer stack used in the experiments, featuring qualitative field profiles of long-range SPPs (LR-SPPs, red) and short-range SPPs (SR-SPPs, blue); b) Typical FTEM of the metasurfaces fabricated on thin silver films, showing the presence of a set of two structure ring pairs.*

Remarkably, in this experiment four structure rings (two structure ring pairs) instead of only two structure rings are observed in the FTEM (Figure 5.18b). The inner structure rings once again touch at $x^{-1} = y^{-1} = 0$, which suggests that these are linked to the waves initially excited by the laser. Upon analysis, both the radii and the horizontal shift of the inner rings could be linked to the long-range SPP (LR-SPP) mode, with $r_{in} = r_{s,1} = 2.16\,\mu m^{-1} = 1/\lambda_{LR}$ and a corresponding effective index of 1.42. Since a sapphire prism with a refractive index of

1.76 is used in the Kretschmann configuration, it is possible to excite the LR-SPP mode directly with the laser.

However, the radii of the outer structure rings are larger than the horizontal shift $r_{s,2} > r_{in}$, resulting in two intersections of these structure rings along the y^{-1} axis. These outer rings correspond to the short-range SPP (SR-SPP) mode, with $r_{s,2} = 3.18\ \mu\mathrm{m}^{-1} = 1/\lambda_{SR}$. It can therefore be assumed that, in addition to the long-range SPPs, which are directly excited by the laser, the short-range SPPs are also involved in the growth process of the AgNPs.

The horizontal shift of the ring centres (r_{in}), representing the incident plane wave, is identical for both pairs of rings, while the ring radii, corresponding to the scattered spherical wave, differ. This indicates that in the Kretschmann configuration, only the LR-SPP can be directly excited. However, the metasurface provides the necessary momentum to also excite SR-SPPs, effectively mediating the coupling between LR-SPPs and SR-SPPs. This experimental observation confirms that features associated with the high-index SR-SPP mode $n_{SR\ SPP} = 2.1$ can be successfully integrated into the resulting metasurface. This high effective index of the SR-SPP clearly shows, that a direct excitation with the sapphire prism is not possible.

To further investigate the properties of the SR-SPP mode, a two-dimensional field distribution and the corresponding field intensity distribution of the SR-SPP mode have been simulated and are shown in **Figure 5.19**. The simulation is conducted using rigorous coupled wave analysis (RCWA). For the RCWA simulations, a refractive index of the ELD solution of $n_{ELD} = 1.336$ (as measured before in section 5.2 using Michelson interferometry) is assumed.

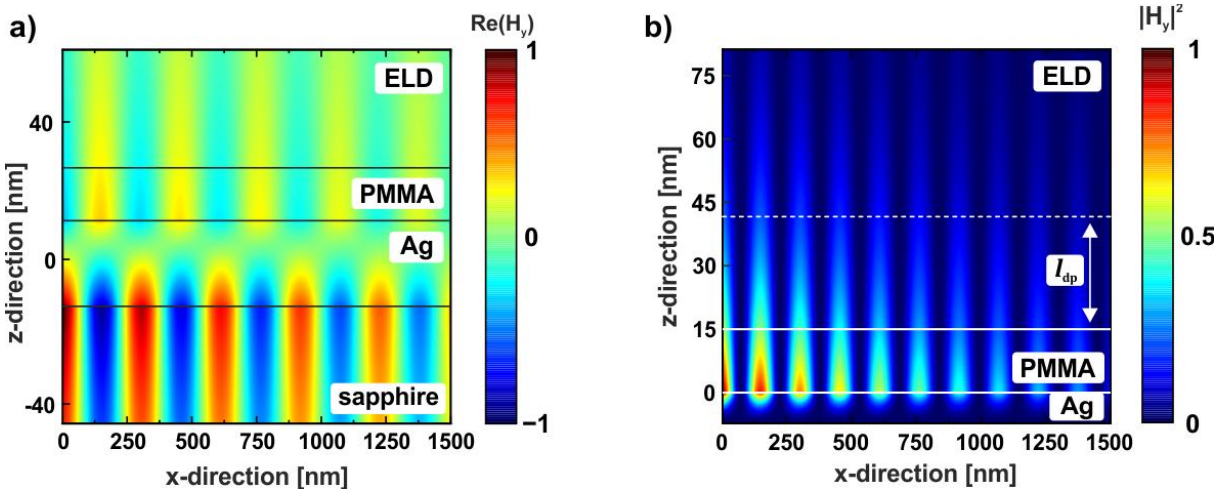

***Figure 5.19**: a) simulated 2D magnetic field distribution and the corresponding magnetic field intensity distribution of the SR-SPP mode using rigorous coupled wave analysis (RCWA) (the dashed line in b) indicates the penetration depth of the SR-SPP mode into the ELD solution).*

The magnetic field distribution in Figure 5.19a show that the SR-SPP mode is predominantly confined to the silver/sapphire interface. However, both modes (LR-SPP and SR-SPP) extend into the ELD solution, allowing interaction with the ELD solution and thus may contribute to the AgNP growth. Furthermore, after the metasurface has been grown, both hybrid modes can interact with the metasurface as well as an analyte replacing the ELD solution.

The further variation in silver film thickness t_{Ag} allows for a detailed characterization of the dispersion of the hybrid plasmonic modes as a function of the film thickness. The silver films were fabricated with thicknesses ranging from $t_{Ag} = 20$ nm to $t_{Ag} = 56$ nm. **Figure 5.20a** presents FTEM images of metasurfaces deposited on silver films of three different thicknesses. Notably, the diameter of the outer structure rings increases as t_{Ag} decreases, while the radius of the inner structure rings remains largely unchanged in cases (i) and (ii). This trend holds for larger t_{Ag} as well (see Figure 5.20b), until the hybridization effects diminish and the hybrid modes transition into distinct SPP_a and SPP_b modes, whose mode indices remain constant over t_{Ag}.

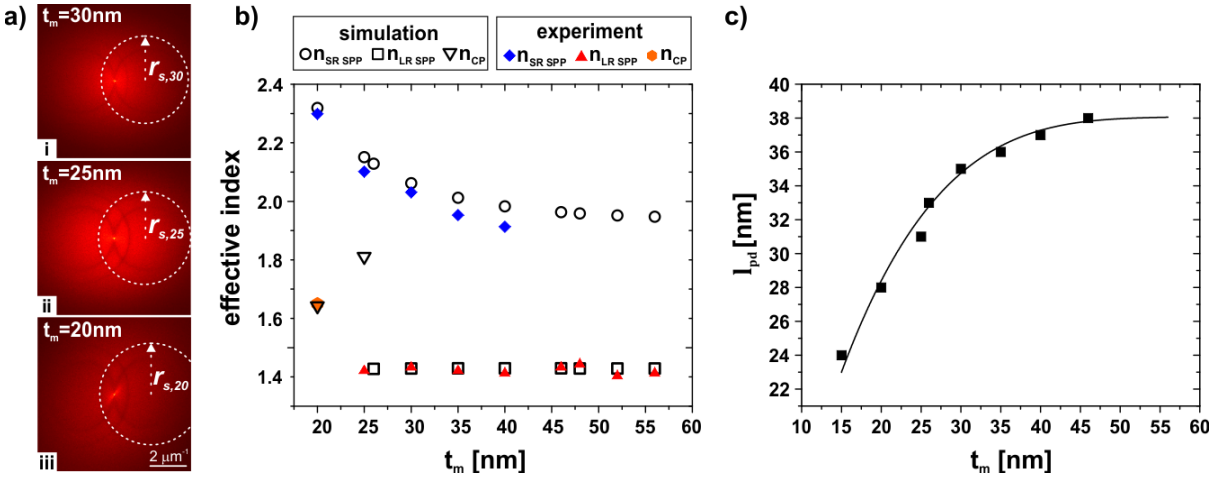

***Figure 5.20**: Dispersion of Hybrid Plasmonic Modes as a Function of Silver Film Thickness (t_{Ag}). a) FTEMs of metasurfaces fabricated on silver films with thicknesses of 30 nm (i), 25 nm (ii), and 20 nm (iii); b) Comparison of measured and simulated effective indices for long-range (LR) and short-range (SR) SPPs; c) Simulated penetration depth (l_{pd}) of SR-SPPs into the ELD*

solution as a function of t_{Ag}. Data points represent values for l_{pd} extracted from mode profiles calculated with a 1 nm resolution in the z-direction, while the solid line serves as a visual guide for interpretation.

In our experiments, hybridization effects (structure rings linked to SR-SPPs) were observed in the FTEMs for silver film thicknesses up to $t_{Ag} = 40$ nm. For $t_{Ag} = 20$ nm, the effective index of the SR-SPP even reaches 2.3, and simulations indicate that the corresponding penetration depth into the ELD solution is as short as 28 nm. Figure 5.20b compares the effective indices of the plasmonic modes obtained from both simulations and experiments, demonstrating a good agreement between the two. The close match, particularly for the SR-SPP modes at thinner silver films, suggests that the mode propagation is largely undisturbed by the presence of the metasurface, allowing the SR-SPP mode to maintain its characteristics even in the complex environment of the fabricated structures. Figure 5.20c illustrates the penetration depth (l_{pd}) of the SR-SPP mode as a function of t_{Ag}. In theory, vertical confinement of the SR-SPP mode should increase with decreasing t_{Ag}, which leads to enhanced surface sensitivity. However, in practice, fabricating continuous silver films with thicknesses below a few nanometers is technologically challenging due to the tendency of the films to form island structures. This behavior is influenced by various factors such as temperature, adhesion, and moisture.[96]

These findings highlight the tunability of the plasmonic modes by controlling the silver film thickness, offering a way to tailor the optical properties of the metasurface for specific sensing and photonic applications. As the film thickness decreases, the strong confinement of SR-SPPs near the surface becomes more pronounced, allowing for enhanced sensitivity to changes in the surrounding environment.

Only for $t_{Ag} = 20$ nm, a notable deviation was observed between the simulated and measured effective index of the LR-SPP (see Figure 5.20b). This discrepancy was consistent and remained robust against variations in the surface roughness of the silver film.

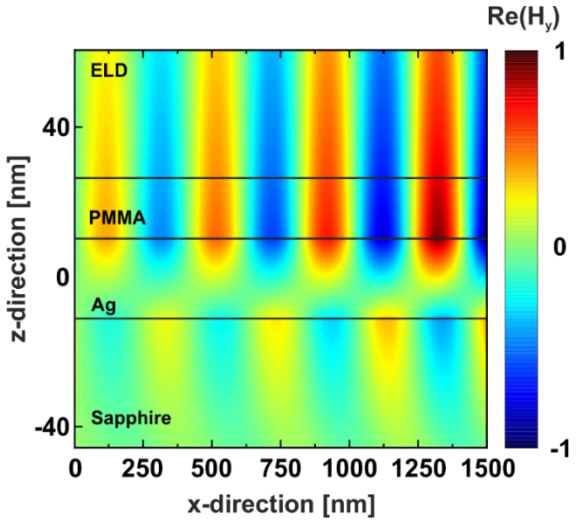

***Figure 5.21**: 2D magnetic field fistribution of the counter-propagating mode with an effective refractive index of 1.64 for $t_{Ag} = 20$ nm.*

Indeed, for $t_{Ag} < 20$ nm, structure rings could not be observed in the FTEMs, suggesting that the plasmonic behavior is severely impacted by the discontinuous nature of the films. This limitation highlights the importance of optimizing film deposition parameters for achieving high-quality, continuous thin films, which are critical for reliable plasmonic mode propagation and enhanced sensor performance.

In the simulation results (see **Figure 5.21**), a counter-propagating mode (propagating in the negative x-direction) could be found with an antisymmetric field profile and an effective index of $n_{cp} = 1.64$ (compared to the experimental value of $n_{cp} = 1.65$. This suggests that multiple modes, facilitated by the additional momentum provided by the metasurface, are involved in the process.

Interestingly, the expected LR-SPP mode could not be detected in simulations for silver films with thicknesses $t_{Ag} < 26$ nm. Despite this, experimental data still showed features originating from the LR-SPP mode for $t_{Ag} = 25$ nm (see Figure 5.20b). This discrepancy can likely be attributed to factors such as the limited measurement precision of the profilometer, or surface roughness—none of which are accounted for in the simulation. These factors may influence the experimental results, allowing the LR-SPP mode to persist even in films slightly thinner than what the simulation predicts.

This finding underscores the importance of considering real-world imperfections in experimental setups, which can lead to deviations from idealized simulation models and provide valuable insights into the behavior of plasmonic modes in complex environments.

To further support the hypothesis that multiple modes with significantly different mode indices and propagation directions can be involved in the process, additional experiments have been conducted using simultaneous illumination with two lasers at different wavelengths. **Figure 5.22a** shows the experimental setup for this approach. Instead of the half-cylindrical prism, a spherical plano-convex sapphire lens was used, which enables to excite plasmonic modes propagating nearly perpendicular to each other ($\phi \approx 90°$) within the x-y plane. In this configuration, the 532 nm laser propagates along the x-direction, while the 660 nm laser propagates along the y-direction.

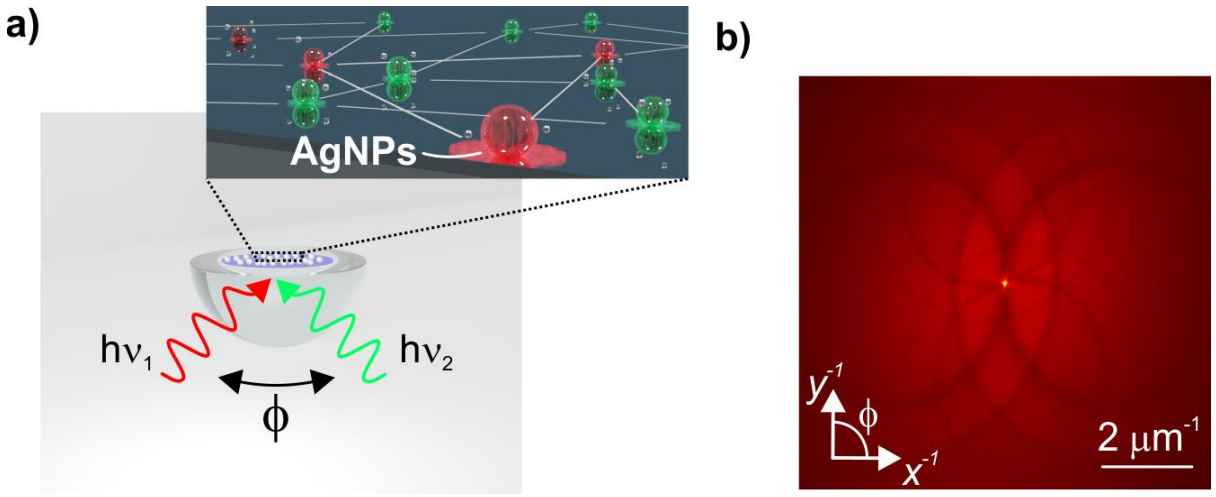

***Figure 5.22**: Disorder-engineered metasurfaces on thin silver films excited by two lasers simultaneously. a) Schematic of the experimental setup, illustrating the simultaneous illumination from two different lasers and the principle of particle formation under dual-wavelength excitation (inset); b) A typical FTEM of the resulting metasurface, displaying structure rings corresponding to the four hybrid plasmonic modes excited by the two lasers at different wavelengths.*

This arrangement introduces an additional degree of freedom in the system by enabling the excitation of plasmonic modes in two distinct propagation directions. The involvement of multiple propagation directions and mode indices adds complexity to the system, offering new possibilities for manipulating and tuning the optical response of the metasurface. From

an application perspective, this is particularly valuable, as it allows for the simultaneous utilization of multiple plasmonic modes, each with its own distinct mode profile, penetration depth, and effective index, all at the same location. This capability enhances the versatility and functionality of the system, enabling more sophisticated control and tuning of the optical properties.

5.4. Chapter Summary

In this chapter, it has been shown that the deposition of silver nanoparticles using the electro-less deposition of silver enables to create metasurfaces with engineered disorder. This engineered disorder exhibits a wide range of characteristics, achieved through deposition in darkness, light-controlled growth (photonic excitation), and surface plasmon polariton (SPP) excitation. First, by varying the deposition time only, disordered hyperuniformity can be observed and controlled, even without illumination (in darkness), via the deposition time. Light-controlled deposition further enables isotropic stealthy DHU and by using different incident light wavelengths enables to adjust K. Furthermore, incorporating SPPs allows for the fabrication of metasurfaces with anisotropic stealthy DHU, previously only described theoretically.

Following the path of SPP excitation during particle growth also enables sharp spectral features required for many optical applications, such as sensing. A key feature here is that, unlike conventional manufacturing methods, the fabrication and application environments can be identical. As a result, the sharp spectral feature is inherently aligned with the light source. Furthermore, it has been observed that sharp spectral features (indicating low loss) can be produced although the contributing SPP resonance possess significant losses. This phenomenon can be attributed to the coherent and highly parallel illumination and thus coherent interaction with the metasurface over a large area. Based on this finding, it has been shown that the presented method can also be used to harness short-range SPP (SR-SPP) modes within planar silver films, which is typically challenging due to the high index of the SR-SPP mode. However, the use of hybrid modes offers several advantages, particularly in reducing ambiguities in optical sensors due to their significantly different penetration depths of the modes into the analyte. Additionally, the SR-SPP exhibits exceptionally strong surface confinement, which could be a promising step towards single-molecule detection.

Chapter 6

Nonlinear Material Concepts

Following the waveguide concepts presented in chapters 4 and 5, this chapter will focus of the development of nonlinear materials characterized by three essential properties. First, they should exhibit substantial nonlinearity, enabling the efficient phase modulation of an electromagnetic wave. Second, the materials should be highly transparent, making them compatible with waveguide phenomena that rely on millimeter or even centimetre scale propagation lengths (see chapter 4). The third essential property is technological compatibility with methods of polymer technology, allowing for scalable and cost-efficient production.

6.1. Introducing Kerr Nonlinearity to PDMS via Swelling

(The following section is based on journal paper 3 of the publication list.)

In the following chapter, a method will be presented to facilitate the integration of nonlinear organic solvents, which typically show strong optical nonlinearity into optical waveguide architectures based on solid (thin) films[33]. The approach involves incorporating these organic solvents into poly-dimethylsiloxane (PDMS) via swelling. So far, in photonics PDMS has proven particularly useful in the development of stretchable optical components, but is not known to show substantial nonlinearity[141–143]. However, there are some reports in the literature about introducing optical nonlinearity into PDMS. For instance, some reported approaches involve embedding chromophores[144,145], plasmonic nanoparticles[146,147], perovskites[148,149], or 2D materials[150,151] into a PDMS host matrix. However, these techniques often face challenges, particularly the simultaneous introduction of significant absorption. This absorption can limit the performance of optical waveguides where high propagation lengths may be desired (see chapter 4). To evaluate the potential of incorporating nonlinear solvents in PDMS via swelling for use as a NLO material, first the nonlinear optical properties of the individual materials are assessed using the Z-scan technique. This approach allows for a precise characterization of

the nonlinear refractive index and absorption properties before incorporating them into the PDMS host matrix.

For the experiments, three different solvents were selected. First, nitrobenzene (NB) was chosen because of its strong nonlinearity reported in the literature[152]. Second, toluene (TL) was selected because of its reported nonlinearity (although less than NB) and its significant swelling behaviour in PDMS[95,152]. Finally, 2,6-lutidine (LT) was chosen as it also exhibits nonlinearity but is considerably less harmful compared to the other two solvents[153]. While the PDMS was investigated as a free-standing 1 mm thick film, the three solvents were investigated within a 1 mm thick quartz cell. The quartz cell did not show any nonlinearity under the corresponding experimental conditions.

Figure 6.1 shows the results of measurements on pure PDMS as well as different solvents using open-aperture (OA) and closed-aperture (CA) z-scans. The experiments were conducted at a pulse energy of 5.6 µJ and a repetition rate of 50 Hz. The results reveal distinct nonlinear optical properties among the different solvents (see Figure 6.1). All solvents exhibit a characteristic valley-peak profile, indicative of self-focusing (positive n_2), caused by the optical Kerr effect (OKE). As expected, NB shows the strongest OKE among the three candidates. The nonlinear refractive index could be measured as $n_2 = 22 \cdot 10^{-15}\,\mathrm{cm}^2/\mathrm{W}$ for nitrobenzene, which fits well to values found in the literature[21]. In addition to the Kerr effect, two-photon absorption (2PA) was observed in nitrobenzene (NB), as shown in the inset of Figure 6.1a. The inset shows the result of an OA Z-scan experiment.

Features of an optical Kerr effect were also found in the measurement results for both LT and TL as shown in Figures 6.1b and 6.1c. However, in both cases the OKE was less pronounced compared to NB. The same nonlinear refractive index of $n_2 = 7.1 \cdot 10^{-15}\,\mathrm{cm}^2/\mathrm{W}$ was measured for both LT and TL, which is approximately three times smaller than for NB. Notably, the absorption properties do not show nonlinearity for TL and LT. Furthermore, pure PDMS did not exhibit any detectable nonlinearity at a pulse energy of 5.6 µJ (Figure 6.1d).

The results shown in Figure 6.1 emphasize the solvent-specific nonlinear optical responses, with nitrobenzene showing the most significant nonlinearity. However, this is accompanied by nonlinear absorption, which could lead to thermal effects at higher illumination intensities.

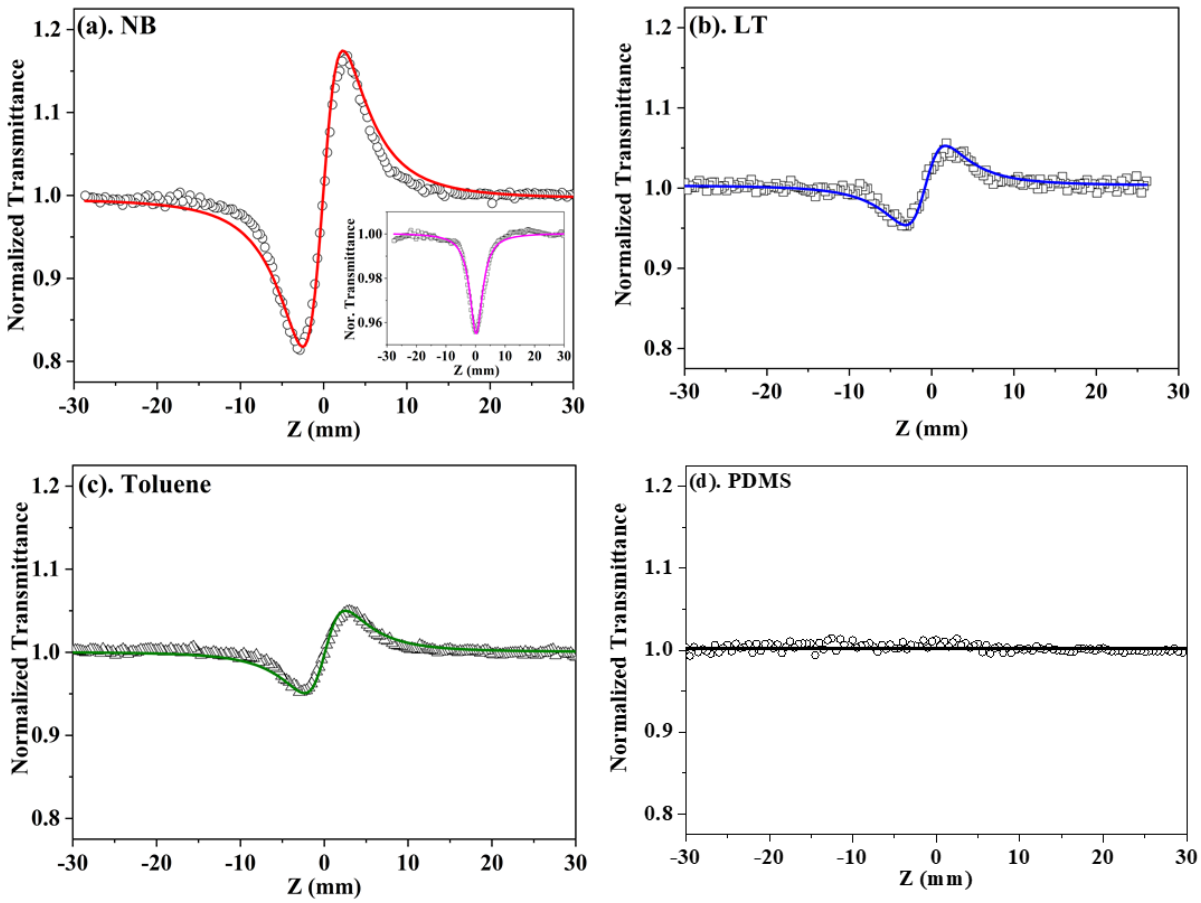

Figure 6.1: *Closed aperture Z-scan profiles of nonlinear solvents and the PDMS film. a) CA Z-scan profile for nitrobenzene and OA Z-scan profile of nitrobenzene (inset) showing nonlinear absorption (only observed in nitrobenzene); b) CA Z-scan profile for* 2,6-lutidine; c) *CA Z-scan profile for* toluene; d) *CA Z-scan profile for* PDMS. *Symbols are the experimental data and solid lines show the theoretical fit.*

In the next step, the swelling ability of PDMS with the three solvents is investigated. Therefore, PDMS slabs were fabricated in Teflon molds and then immersed in the three solvents. It could be observed that the swelling of the PDMS occurred on different time scales. Furthermore, significantly different amounts of each solvent were incorporated into the PDMS. **Figure 6.2** illustrates the solvent-specific swelling behaviour of the PDMS films as a function of time. At the point of saturated swelling, the thicknesses of the samples (initially 3 mm PDMS thickness in all cases) were found to be 3.1 mm (NB), 3.3 mm (LT), and 4 mm (TL). Also, the lateral dimensions of the samples show the same behaviour, as the swelling leads to an isotropic expansion of the material.

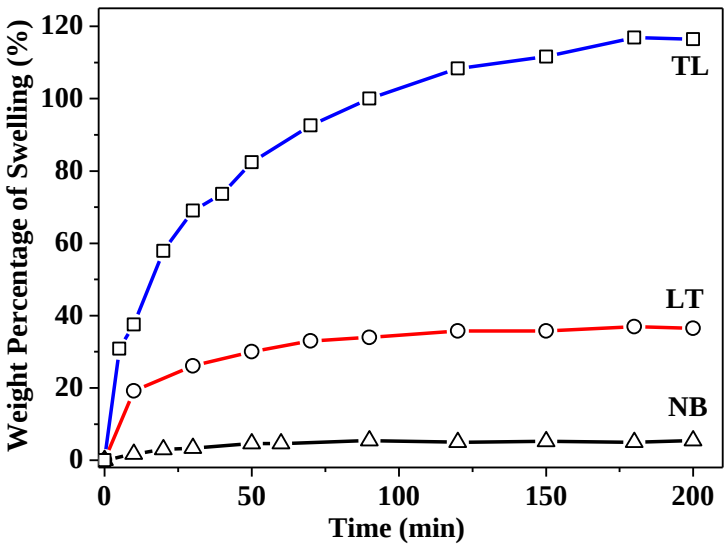

***Figure 6.2**: Weight change of the PDMS samples over time caused by solvent swelling.*

Nitrobenzene (NB) resulted in the least swelling, inducing only a 5.4% weight change in the PDMS. In contrast, 2,6-lutidine (LT) caused a stronger swelling, leading to a 36.5% weight increase. The most significant effect was observed with toluene (TL), which caused a substantial 116.3% weight change. At this point, it is worth noting that the material with the strongest Kerr effect (NB) shows the least swelling. Contrary to intuitive expectations, these results suggest that the solvent with the highest Kerr effect may not necessarily lead to the best nonlinear composite material. On the other hand, toluene, which has a Kerr nonlinearity only three times weaker than NB, allows for more than 20 times higher incorporation into PDMS. At this point, this finding renders TL a promising candidate for the goal to introducing nonlinearity into PDMS via solvent swelling.

To characterize the nonlinear optical properties of the composite materials, the samples are placed between two quartz slides. First of all to gain mechanical stability and to be able to mount the samples in the Z-scan setup. In addition, covering the samples with quartz prevents solvent evaporation during the measurement.

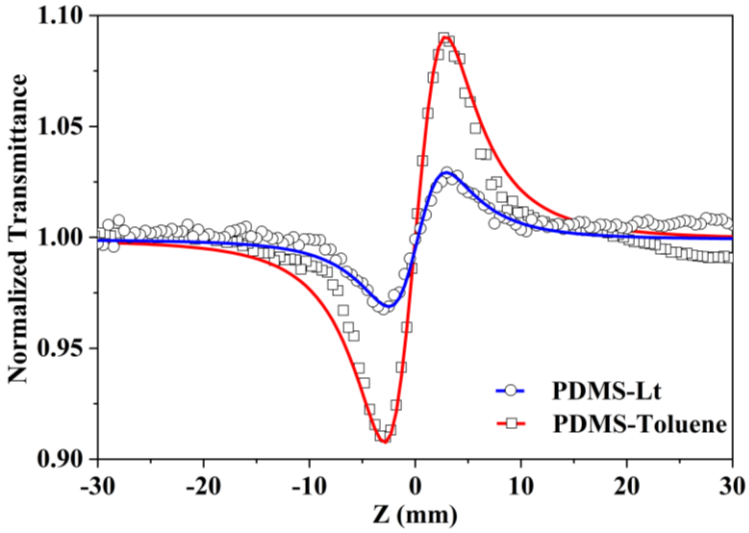

Figure 6.3: The comparative CA z-scan profiles of the PDMS incorporated with 2,6-lutidine and toluene at a pulse energy of 5.4 µJ. Symbols are the experimental data and solid lines indicate the theoretical fit.

Figure 6.3 presents the CA Z-scan profiles of the PDMS-TL and PDMS-LT composite samples, measured with a pulse energy of 5.4 µJ. Both samples exhibit an OKE. Notably, PDMS-TL shows a twofold stronger Kerr effect compared to PDMS-LT (see Figure 6.3) with a nonlinear refractive index of $n_2 = 3.1 \times 10^{-15}\ \mathrm{cm}^2/\mathrm{W}$. Open-aperture Z-scan measurements confirm the absence of nonlinear absorption processes in both composite samples. In contrast, PDMS/NB exhibits a strong thermally induced nonlinear optical response under the same experimental conditions. This thermal effect arises from the linear and two-photon absorption (2PA) of NB, leading to localized heating. In fact, the thermal effect in PDMS/NB was so pronounced that the z-scan measurements were significantly affected by artefacts. These artefacts include significant beam distortion, the formation of self-diffraction rings, and even photo-induced degradation processes. For pure PDMS, thermal effects were only observed at higher pulse energies above 7.4 µJ.

Thermal effects caused by (nonlinear) absorption are a well-known phenomenon in NB, with several options available for mitigating them. Therefore, we reduced the pulse energy to 0.8 µJ and lowered the repetition rate from 50 Hz to 10 Hz in our measurements of PDMS/NB to minimize thermal effects. However, at pulse energies up to 0.8 µJ, no nonlinear behaviour was detected in the PDMS/NB samples. For higher pulse energies, only thermal effects and photo-induced damage due to absorption were observed. This suggests that the detection

limit for the Kerr effect in PDMS/NB lies above the damage threshold of the material. Interestingly, neither pure PDMS nor NB alone exhibited thermal effects at a pulse energy of 1.2 μJ, indicating that the thermal effects in PDMS/NB cannot be explained by superposition of the properties of the individual materials.

In addition to the inherent nonlinear optical (NLO) properties and swelling behaviour, a third critical factor for material selection is the absorption properties. Beyond potential thermal nonlinearities and material degradation, absorption can introduce significant limitations in the design of photonic devices, such as low-loss waveguides.

In nonlinear optics, it is quite common to compensate for relatively low NLO effects by increasing the light-matter interaction length, thereby achieving the same phase shift in the propagating wave. For this strategy to be effective, however, material absorption must be sufficiently low to avoid excessive absorption losses over the desired interaction length.

At 532 nm, the linear absorption coefficient α for NB is around $2\ \mathrm{m}^{-1}$, while for TL it is much lower ($\alpha = 0.24\ \mathrm{m}^{-1}$)[154,155]. At 400 nm, this disparity in absorption becomes even more pronounced, with NB showing a 30-fold higher absorption compared to TL. A trend that further increases with shorter wavelengths. This significant difference suggests that the PDMS/TL composite is particularly advantageous for applications at shorter wavelengths, especially in the ultraviolet (UV) range.

Although nitrobenzene (NB) is one of the most well-known NLO materials, the PDMS/NB composite exhibited the strongest thermal contributions and the lowest swelling effect in PDMS. This underscores the importance of considering not only the nonlinear optical properties but also swelling behaviour and absorption characteristics when selecting materials for photonic applications.

In order to exclude any residual thermal contributions to the nonlinear properties of the PDMS/TL and PDMS/LT samples, intensity-dependent closed-aperture (CA) Z-scan measurements were conducted. **Figure 6.4** displays the CA Z-scan profiles of the samples under varying pulse energies, and thus illumination intensities. The experimental data were fitted using equation 2.7 (solid lines in Figure 6.4), and the corresponding nonlinear refractive indices were derived. In both cases, the nonlinear refractive index remained constant across

different irradiance levels (see insets in Figure 6.4). This confirms that the observed nonlinear refraction is attributed to the optical Kerr effect, with thermal effects being negligible.

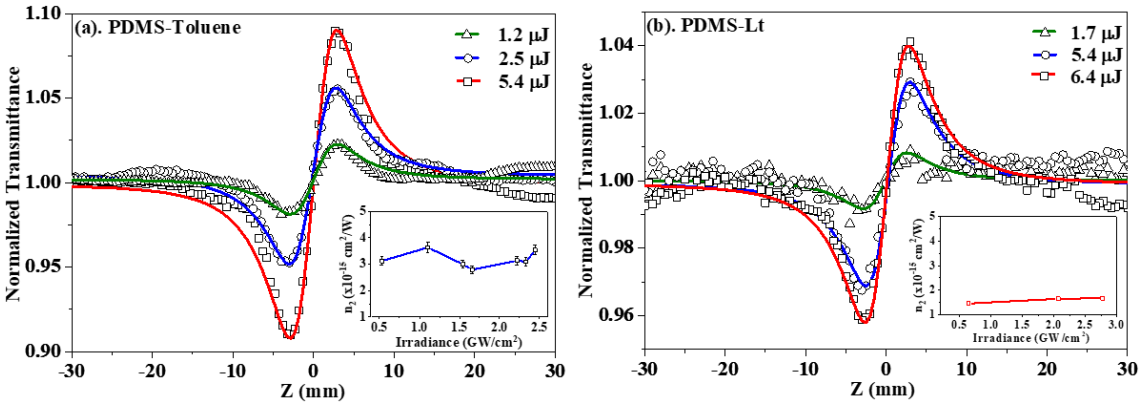

***Figure 6.4**: Intensity dependent CA Z-scan profiles of the PDMS-toluene (a) and PDMS/Lt samples (b). Symbols represent the experimental data and solid lines show the theoretical fit. The insets in a) and b) show the nonlinear refractive indices as a function of the irradiance. An irradiance of 0.53 GW/cm^2 corresponds to a pulse energy of 1.2 µJ in our experiment.*

The following table shows all third order nonlinear refractive indices of all composite samples derived by using equation 3.4 and shown in the following Table.

Sample	n_2 (x10^{-15}cm^2/W)	β_{2PA} (cm/GW)	Re($\chi^{(3)}$) (x10^{-16}cm^2/V^2)
NB	22.8	0.36	1.97
LT	7.1	-	0.56
TL	7.1	-	0.57
PDMS/TL	3.1	-	0.26
PDMS/LT	1.5	-	0.11
PDMS/NB[1]	n.a.	n.a.	n.a.

[1]not applicable (n.a.), because of measurement results governed by significant artefacts caused by thermal effects and photo-induced degradation of the samples within the entire experimental parameter range.

6.2. Controlling Thermal Nonlinear Effects in Nitrobenzene

(The following section is based on journal paper 4 of the publication list.)

Although for the application in PDMS/solvent composite materials, the strong thermal effects in NB may seem unpromising. However, thermal nonlinearities can be of technological interest as well, as long as applications do not require very short response times. In particular, they can be used for highly precise temperature measurement and, consequently, for radiation detection as well. A concept, which is being investigated in a recent project at the LGOE. Further investigations have shown that thermal effects in NB can be influenced by an external electric field. The results of these investigations will be discussed in the following. Building up on the observation of thermal nonlinear effects in NB in the previous chapter, now the investigation of the thermal-induced nonlinear refractive index in NB will be the focus. Therefore, again CA and OA Z-scan measurements under picosecond illumination at a wavelength of 532 nm with varying repetition rates are conducted. The quartz cell used for the measurements had an optical path length of 1.4 mm. The beam waist radius ω_0 of the focussed laser beam was measured 21.1 µm using the knife-edge method. **Figure 6.5** shows the CA Z-scan profiles, along with the deduced values for the effective nonlinear refractive indices of NB when pumped at various repetition rates (10 Hz, 50 Hz, 100 Hz, 300 Hz, 500 Hz, 750 Hz, and 1 kHz). For referencing, the empty quartz cell was tested under the same experimental conditions in both CA and OA Z-scan configuration. The results show no optical nonlinearity of the empty quartz cell under the described experimental conditions.

NB exhibits three distinct types of Z-scan profiles across repetition rates ranging from 10 Hz to 1 kHz (Figure 6.5a). At low repetition rates (≤ 600 Hz), the Z-scan curve displays a valley followed by a peak, indicating self-focusing nonlinear refraction due to the optical Kerr effect. Below 200 Hz, the Z-scan curves maintain a constant amplitude, suggesting the absence of any thermal contributions.

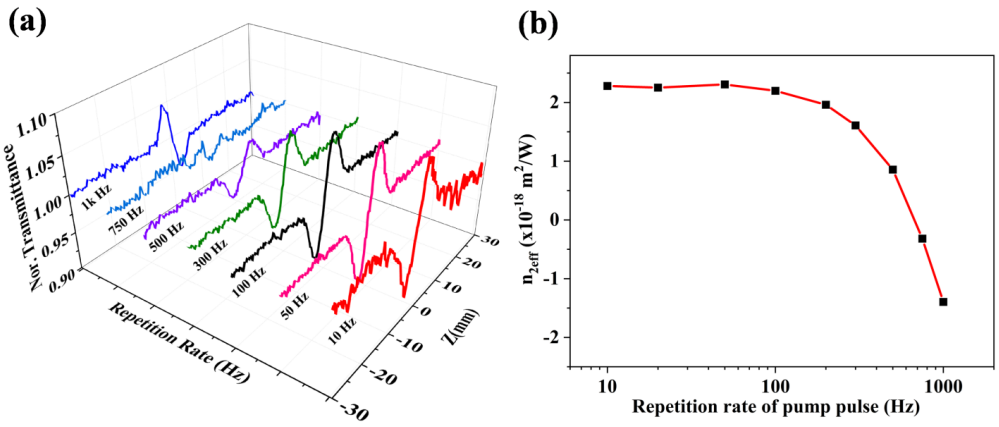

***Figure 6.5**: a) Closed aperture Z-scan profiles of NB with various pulse repetition rates at constant peak power; b) The effective nonlinear refractive index as a function of the repetition rate of the laser.*

However, above 200 Hz, the magnitude of the valley-peak profile begins to diminish, eventually flattening around 750 Hz due to the accumulation of thermal effects from the intense pump pulses. While the Kerr nonlinear response of NB shows self-focusing (positive n_2) behaviour in the CA Z-scan, the contributions lead to self-defocusing (negative n_2). At higher repetition rates (800 Hz and above), the NLR curves shift from the valley-peak to a peak-valley profile, indicating dominant thermal induced nonlinear refraction.

This behaviour is quite typical for many materials, as the thermal energy has less time to dissipate with increasing repetition rates. As a result, beyond a certain repetition rate, the changes in the refractive index do not fully vanish before the next pulse interacts with the sample material. Consequently, thermal effects accumulate.

In the next step, a DC electric field is applied to the nitrobenzene, using a quartz cell equipped with two electrodes spaced 10 mm apart (see **Figure 6.6**). Initially, aluminum electrodes were used for the experiment. However, after a few minutes of applying voltage, a dark, almost black, veil appeared on the surface of the cathode, indicating the occurrence of an electrochemical reaction. In some literature, this effect is often attributed to impurities in the nitrobenzene. However, after replacing the aluminum electrodes with stainless steel electrodes, the issue was no longer observed.

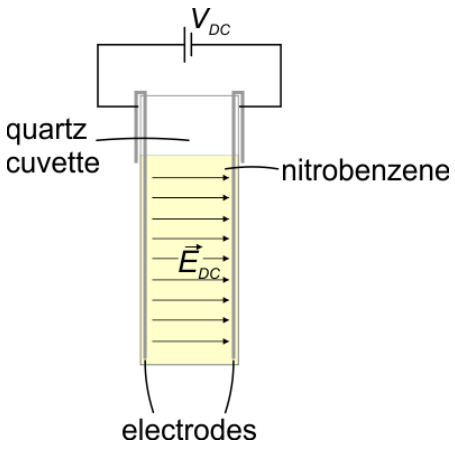

***Figure 6.6**: Schematic of the cuvette used for Z-scan experiments with applied DC fields. A quartz cuvette filled with nitrobenzene and flanked by two electrodes. A DC voltage is applied to generate a homogeneous electric field between the two electrodes.*

For the z-scan experiments, the sample cell was placed on the linear stage in the z-scan setup so that the horizontally polarized beam propagated centrally between the electrodes. **Figure 6.7** presents the normalized CA/OA Z-scan profiles of nitrobenzene (NB) with and without the application of an electric DC field. In addition, the measurements were repeated at both low (50 Hz) and high (1 kHz) laser repetition rates. For all other measurements, the experimental conditions remained constant, with the only variable being the applied DC field strength.

At a repetition rate of 50 Hz, NB exhibits the typical valley-peak profile in the absence of a DC field, corresponding to its Kerr nonlinear optical response. When a DC field, ranging from $1 \cdot 10^5$ V/m to $7 \cdot 10^5$ V/m, was applied, the Z-scan profiles did not show any significant change. These results were independent on the polarization direction of the laser beam with respect to the DC field.

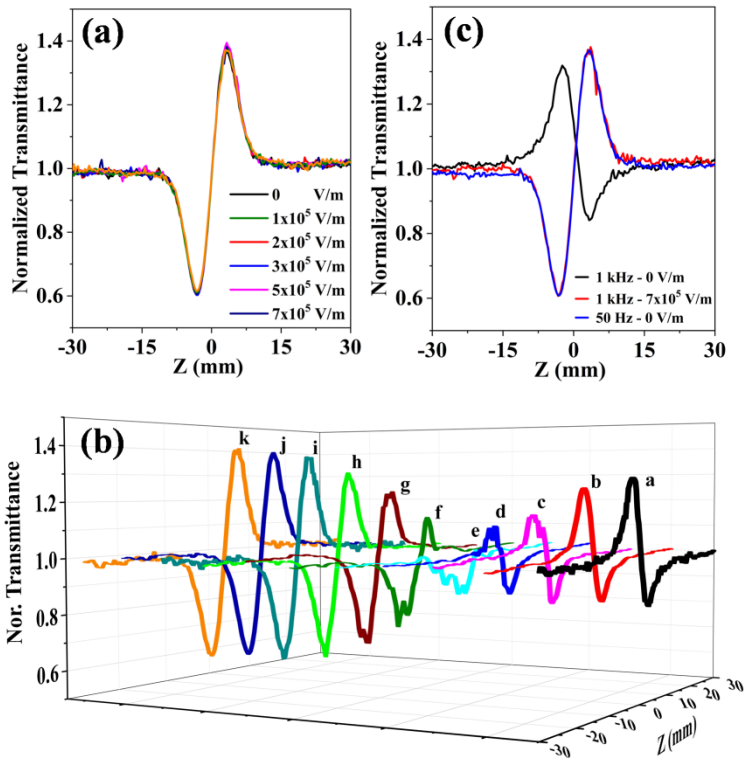

***Figure 6.7**: CA Z-scan profiles of NB in presence of various electric field strengths at a repetition rate of the laser of 50 Hz (a) and 1 kHz (b); c) Comparison of the CA Z-scan profiles of NB under 1 kHz (with 0 and 7x10^5 V/m) and 50 Hz repetition rate pumping at 0 V/m.*

Figure 6.7b shows the normalized CA z-scan profiles of NB at a 1 kHz repetition rate, both in the absence and presence of various external DC fields. In contrast to the results at 50 Hz, a significant variation in magnitude and a reversal in the valley-peak positions are observed. Without a DC field, the CA Z-scan curve (black line) exhibits a peak-valley profile, which indicates that thermal-induced nonlinear refraction is dominant, rather than the optical Kerr effect. However, with the application of a DC field, the thermal effects appear to be reduced, resulting in a scan profile that closely resembles the pure Kerr nonlinear optical response observed at a 50 Hz repetition rate without a DC field (see Figure 6.7c).

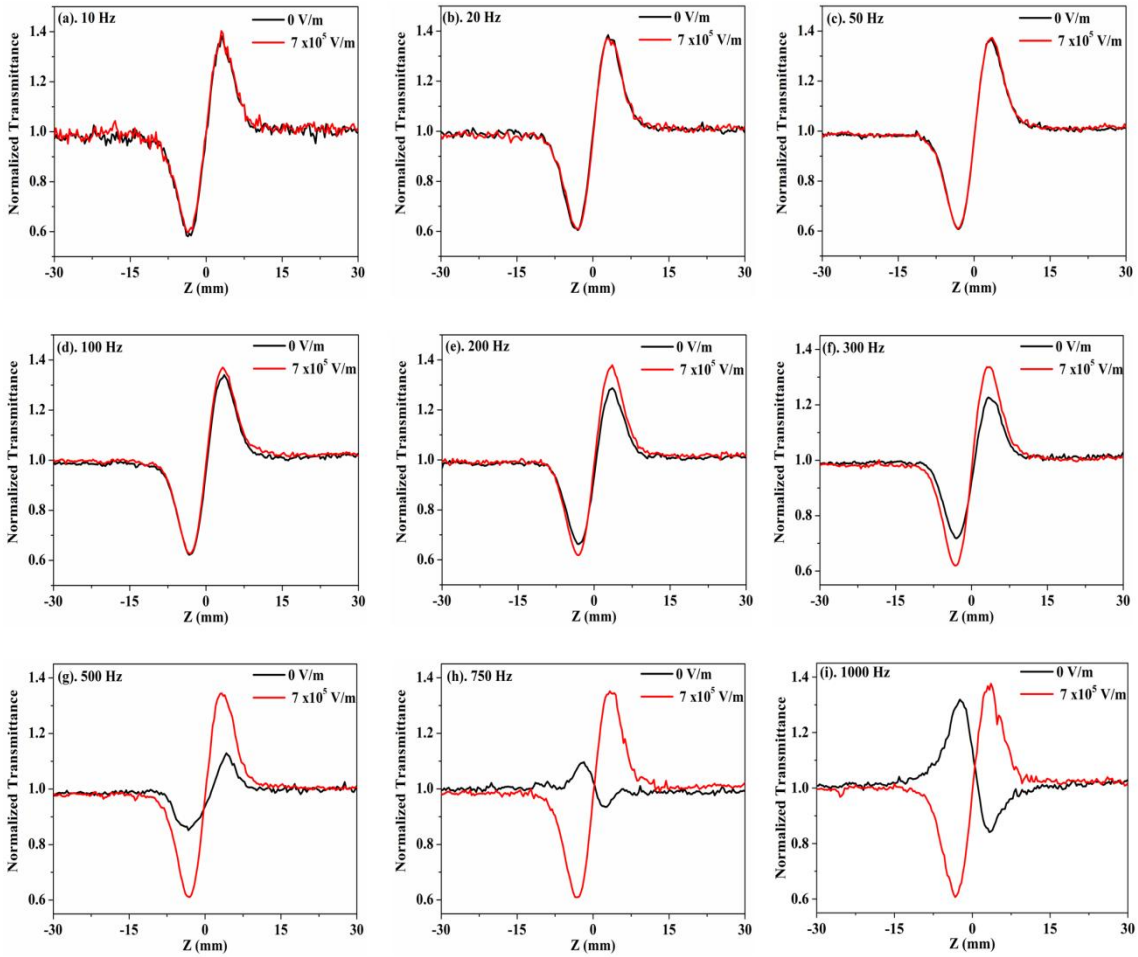

***Figure 6.8**: CA z-scan profiles of nitrobenzene with various repetition rates of the laser in absence and presence of a DC field with different field strengths at a laser pulse energy of 2.5 µJ.*

To further investigate the accumulation of thermal effects in relation to the repetition rate, additional z-scan experiments were conducted, both with and without the application of a DC field. For all measurements, a constant external DC field of $7x10^5$ V/m and a pulse energy of 2.5 µJ were applied. **Figure 6.8** shows the CA z-scan profiles of NB without a DC field (black curves) and with the DC field (red curves) across a repetition rate range of 10 Hz to 1 kHz.

In all CA Z-scan measurements, the red curves representing the $7x10^5$ V/m DC field are identical, representing the optical Kerr effect of the sample material. At repetition rates below 200 Hz (Figures 6.8a–d), the magnitudes and positions of the valley-peak profiles remain unchanged with or without the DC field, confirming the absence of cumulative thermal effects at these low RR. However, as the pulse repetition rate increases beyond 200 Hz, the magnitude of the black curves (no DC field) diminishes significantly, indicating the

accumulation of thermal effects. At even higher repetition rates, the profile changes from a valley-peak to a peak-valley pattern above 750 Hz, displaying the dominance of thermal effects. Remarkably, in all cases, the optical Kerr effect was fully preserved in the presence of the DC field.

When an external DC field is applied to the nitrobenzene (NB) solvent, a noticeable solvent stirring occurs within the sample cell. This rapid electrical stirring is highly effective in dissipating the thermal load generated by solvent absorption under high-intensity laser pumping. To estimate the flow velocity of the NB, we tracked the motion of particles suspended in the solvent using a high frame-rate camera at various DC field strengths (see Supporting Information of [156]).

With a laser beam diameter of 42 µm in our Z-scan setup and an inter-pulse interval of 1 ms, this flow velocity is sufficient to clear the heated material from the illuminated region before the next laser pulse interacts with it. This observation aligns with the results from the Z-scan measurements, where genuine Kerr nonlinearity (positive nonlinear refraction) was observed for DC fields exceeding $5 \cdot 10^5$ V/m, confirming the effective thermal dissipation.

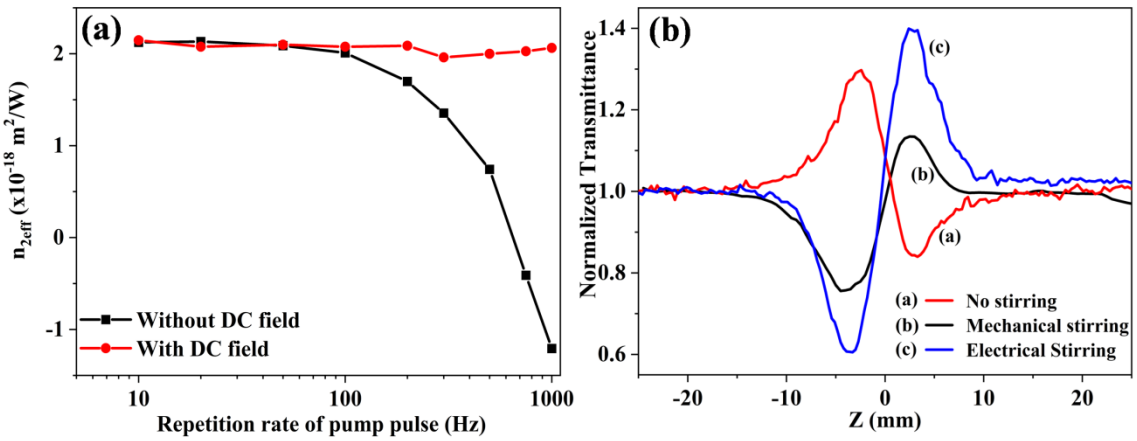

***Figure 6.9**: Controlling the effective nonlinearity via an external DC field. a) Change in the nonlinear refractive index of NB in absence and presence of a DC field as a function of the repetition rate of the laser; b) CA Z-scan profiles of NB without stirring (a), with mechanical stirring (b) and with electrical stirring (applied DC field) (c).*

Figure 6.9a shows the deduced effective nonlinear optical refractive indices of nitrobenzene (NB) in the absence (■) and presence (●) of a DC field, plotted as a function of pulse repetition rate. When an external DC field of $7 \cdot 10^5$ V/m is applied, the nonlinear refractive indices of

NB remain consistent across the entire repetition rate range from 10 Hz to 1 kHz, with no alteration in n_2 (curve ●). This demonstrates that the pure Kerr nonlinear optical response, previously masked by dominant thermal effects, is fully restored with the application of the external DC field. This approach offers a reliable method for determining the intrinsic nonlinear optical coefficients of organic liquids when interacting with long-duration or high-repetition-rate laser pulses. Figure 6.9b presents a comparison between the described method of electric stirring and mechanical stirring. The measurements in the figure indicate that, at the same required input power, electric stirring has a stronger impact on the nonlinearity.

6.3. Dielectric elastomeric actuators for optical phase shifting

The results shown in this section have been part of a Bachelor thesis that I have supervised[157]. Even though optically nonlinear effects, such as the optical Kerr effect or the Pockels effect, are frequently used to influence the phase of an electromagnetic wave, there are other possibilities based on entirely different effects. In nonlinear optics, a change in the phase φ of an electromagnetic wave passing a nonlinear medium (e.g. a Pockels material) is often expressed as

$$\Delta\varphi = \frac{2\pi}{\lambda_0}\Delta n L,$$

where λ_0 is the fixed wavelength, Δn is the induced change of the refractive index (e.g. using the Pockels effect), and L is the interaction length with the nonlinear medium. Intuitively, the interaction length, which is the second parameter that could be manipulated to achieve a phase shift, is difficult to change without complex mechanical setups. However, there are other possibilities to change the interaction length ΔL.

One approach, which will be discussed in this section relies on dielectric elastomeric actuators (DEAs). The concept behind DEAs is the deformation of a soft dielectric elastomeric material (commonly a polymer) by an electrostatic force. The following **Figure 6.10** shows a schematic sketch of a DEA, which consists of a dielectric elastomeric slab of thickness d_0 and the dielectric permittivity ε_r. The elastomer slab is sandwiched between two electrodes to apply an electric voltage V.

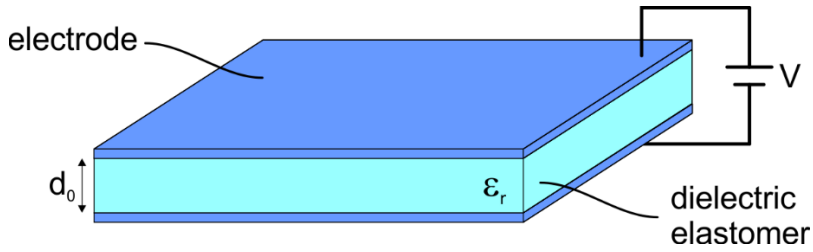

Figure 6.10: *Sketch of a simple DEA adapted from [132].*

For small deformations of the elastomer, the following relationship between the change in the thickness Δd of the elastomer slab and the applied voltage V is valid in good approximation.

$$\frac{\Delta d}{d_0} = -\frac{\varepsilon_0 \varepsilon_r}{\mathrm{Y}} \left(\frac{V}{d_0}\right)^2,$$

where Y is the Young's modulus of the elastomer. [158]

One way to utilize such a DEA as an optical phase shifter would be to introduce a reflection of light at one of the elastomer-electrode interfaces. Thus, an optical phase shifter based on such a DEA has been constructed and the phase shifting properties have been investigated in an experiment. The corresponding results are presented and briefly discussed in the following section.

First, a dielectric elastomeric layer is required for this experiment. A possible candidate would certainly be PDMS, as used in previous experiments. According to the manufacturer data, the Young's modulus of PDMS with a 10:1 ratio of base and curing agent is about $\mathrm{Y} \approx 2$ MPa. However, as can be seen from the above equation, the Young's modulus is a key factor that can be adjusted to achieve the maximum possible deformation per applied voltage.

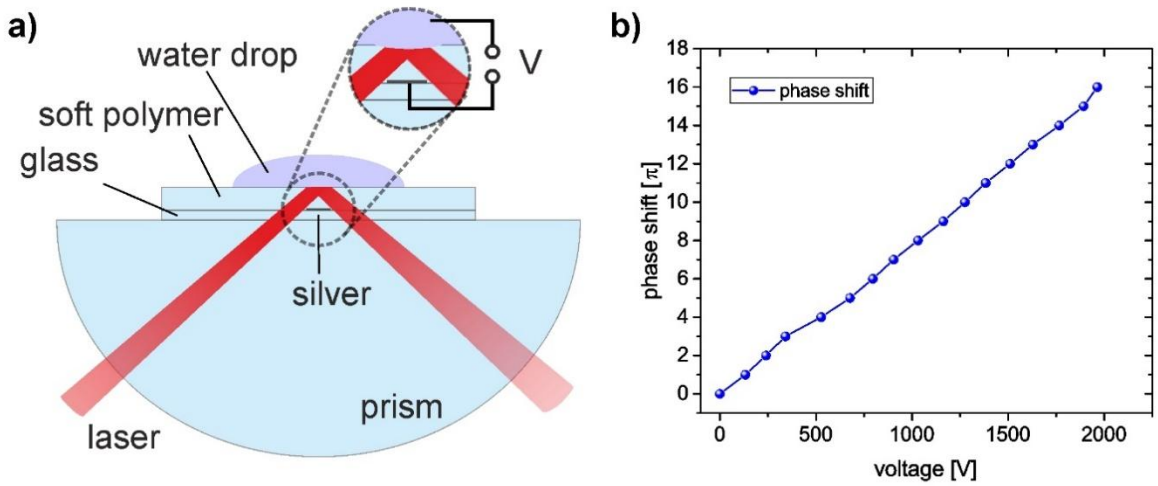

***Figure 6.11**: Setup and Measurement on DEA-based optical phase shifting.*

Therefore, SilGel (Wacker), which is significantly softer ($Y \approx 5\,\mathrm{kPa}$, according to manufacturer data) yet also highly transparent, has been used for the experiments. To apply a voltage across the elastomer layer, two electrodes have to be realized. Therefore, the bottom electrode is implemented as a silver electrode, which is deposited via thermal evaporation. Then, the elastomer layer, approximately 750 µm thick, was deposited onto a glass via cast and cure. The curing of the elastomer layer was conducted at 100°C on a hot plate for 15 minutes. A drop of water is then used a top electrode. The reason for using water as top electrode is twofold. On the one hand, a stiff metal electrode (e.g., silver or gold) on top of a soft elastomer could crack, which would reduce or even completely destroy the conductivity of the metal film. On the other hand, the refractive index profile of the stack using water enables to characterize the voltage dependent phase shift in a total internal reflection geometry. The sample was therefore placed on a glass prism, with index-matching liquid (PDMS base) in between.

Similar to the experiments on plasmonic waveguides shown in the previous chapter, a laser beam was then directed at the sample under an angle of total internal reflection (TIR) at the elastomer/water interface (**see Figure 6.11a**). The sample was adjusted with respect to the laser in a way that the silver electrode is passed (see inset in Figure 6.11a). When a DC voltage is applied between the electrodes, the electrostatic force causes the elastomer to compress in the direction of the applied field, in this case here moving the upper interface of the elastomer closer towards the silver electrode. Thus, the optical path length of the reflected

laser beam is altered and a phase shift is introduced. The resulting phase shift as a function of the applied voltage was then measured using a Mach-Zehnder-Interferometer, where the ATR Setup was placed in one interferometer arm.

The results of these interferometric measurements are shown in Figure 6.11b and demonstrate that this DEA can achieve a phase shift of π (e.g. for the switchable waveguides discussed in chapter 4 at a voltage of around 125V. It can be estimated the modulation speed of such a DEA-based optical phase shifter to be below 100 µs, as DEAs have been shown to operate at frequencies up to 20 kHz in acoustic applications.[159]

Furthermore, it is suprising that the measured phase changes linearly with the applied voltage. Therefore, additional experiments were conducted to separate possible different effects from each other. For this purpose, a semi-transparent electrode made of indium tin oxide (ITO) was used as the bottom electrode. Despite potential issues with long-term stability, a silver electrode was used as the top electrode, fabricated via ELD instead of thermal evaporation, since many silicones gels can outgas under high-vacuum conditions.

The following **Figure 6.12** shows phase measurements conducted at a perpendicular incidence angle. In the first measurement, shown in Figure 6.12a, the laser beam is directly reflected at the silver electrode (see inset), allowing the interferometer to detect only changes in the thickness of the elastomer layer. In this configuration, the laser does not propagate through the elastomer. In the second setup, shown in Figure 6.12b, the laser beam first passes through the elastomer layer and is then reflected at the silver electrode (see inset), which enables to detect both changes in the layer thickness and potential changes in the refractive index of the layer.

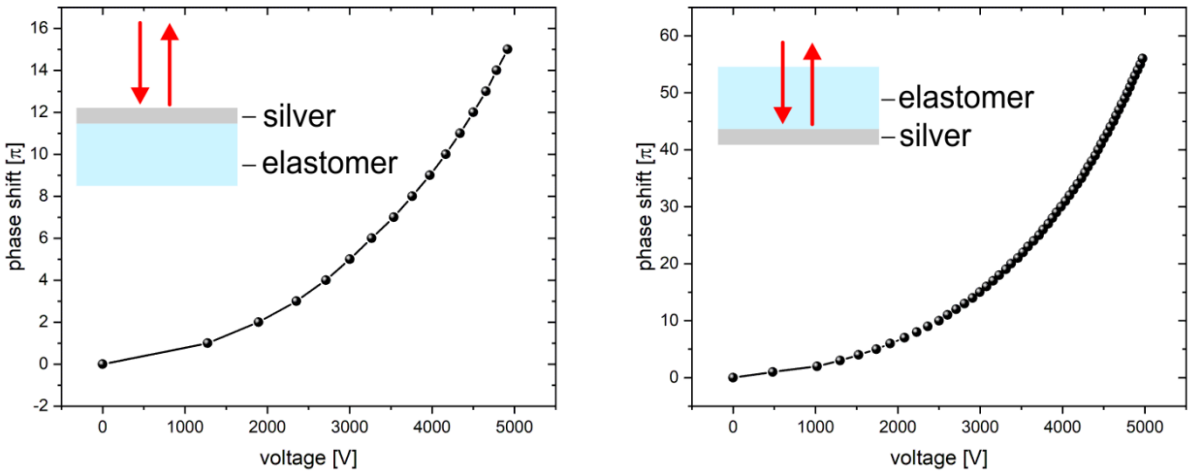

***Figure 6.12**: Phase measurements under perpendicular incidence. a) measured phase shift corresponding to the pure change in thickness; b) measured phase shift caused by both geometric and refractive index change.*

On the one hand, the phase shifts shown in Figure 6.12 both exhibit a quadratic dependency with respect to the applied voltage, as suggested by the above equation. However, the significant difference observed when comparing the two measurement curves indicates a notable effect due to the change in refractive index caused by the uniaxial compression of the material. In this context, the high-voltage range close to 5kV is of particular interest, because, due to the quadratic dependency, a small signal of 30V at an operating point close to 5000V is needed to achieve a phase shift of π. This means an improvement by a factor of 4 compared to the results shown in Figure 6.11.

For practical implementation, it would be necessary to investigate whether this voltage range could be used by applying an appropriate electrical bias, possibly even a mechanical pre-stress. This could significantly enhance the usability of DEA-based optical phase shifters, also in terms of switching speed, by enabling low operation voltages. Further experiments are required to separate the different phenomena and to understand the impact of effects like birefringence on the phase shifting. However, these experiments will be part of future activities and are beyond the scope of this thesis.

6.4. Chapter Summary

The presented NLO composite materials exhibit both optical nonlinearity as well as solid film characteristics, making them highly suitable for integration into layer stacks. At the same time they are still highly transparent, which is in contrast to many other approaches known from the literature, including dyes or metal nanoparticles. Unlike liquid films, the composite materials further eliminate the need for spacers to maintain film thickness, simplifying their application in stacked optical waveguide architectures. However, encapsulation is still necessary to prevent solvent degassing and ensure long-term material stability in application environments.

Despite its strong nonlinearity, nitrobenzene (NB) has proven less practical for integration in PDMS due to weak swelling and significant thermal effects and photo-induced damage. Interestingly, these effects cannot be explained by a straightforward superposition of the properties of the individual materials; PDMS/NB exhibits far less thermal stability than either material alone. The PDMS/TL composite demonstrates superior nonlinear properties compared to PDMS/LT. This is due to the stronger swelling of TL in PDMS, combined with its high transparency, particularly at shorter wavelengths. The transparency of TL allows for extended light-matter interaction lengths, enhancing the nonlinear effects on the light wave. From a practical perspective, toluene (TL) and 2,6-lutidine (LT) present a significant advantage over nitrobenzene (NB) as they are harmful. Furthermore, is has been demonstrated that an external DC field can effectively control the thermal contribution to the nonlinear optical response of nitrobenzene. At sufficiently high field strengths, the thermal nonlinearity can be completely suppressed, allowing for the measurement of the pure Kerr effect via Z-scan, even at high laser pulse repetition rates. Additionally, electrical stirring offers the advantage of contactless operation without the need for moving mechanical parts, making it suitable for integration into miniaturized systems.

Chapter 7

Summary and Outlook

In summary, in this thesis both novel sensitive and nonlinear optical waveguides, as well as corresponding nonlinear materials were introduced. First, in Chapter 3, the concept of node aligned waveguide gratings was discussed. A strongly tuneable propagation length of the TE_1 waveguide mode characterizes this node mode concept. The tuneable propagation length depends on the symmetry of the waveguide with respect to the layer thicknesses and the refractive indices. At this point, I would first like to place these results in the context of current development trends in optical waveguide technology. Growing fields in recent years in the field of optical waveguides have been approaches focused on compatibility with silicon technology, such as Silicon-on-Insulator (SOI). However, in many cases the fabrication technology for such waveguides has a distinct disadvantage: achieving a symmetry in growth direction. In contrast, in polymer technology a symmetric waveguide can be achieved by simply "sandwiching" two layer stacks on top of each other. This straightforward approach renders symmetry technologically facile. Furthermore, the approach presented in this thesis can be used across a wide range of wavelengths, from ultraviolet (UV) to IR and beyond. The only requirements are ensuring the transparency of the polymers used and, if necessary, adjusting the dimensions of layers and gratings.

In fact, the symmetric polymer waveguides shown in Chapter 3.1 are compatible with silicon technology as well through lamination and even enable extension into the third dimension via multiple stacking steps. Since aligning the waveguide on a chip with the necessary precision is technologically challenging, a subsequent adjustment of the on-chip light source is required.

For this purpose, the concept of zero diffraction, introduced in Section 3.2, offers a potential solution. As shown, zero diffraction allows for control over the propagation of light beams within an optical slab waveguide using an electric voltage. The deflection of the light beams occurs at an optical grating, which can now not only provide controlled local in- or out-coupling but also enables in-plane deflection[160]. By varying the structural parameters, the

light can thus be directed to practically any position across the waveguide and then be out-coupled at the desired location.

As shown in Section 3.2, zero diffraction enables the suppression of light interaction with an optical grating, similar to a BIC, enabling optical switching of practically infinite contrast. Furthermore, the zero diffraction waveguide structure in fact resembles a network of miniaturized Mach-Zehnder interferometers. Two spatially separated beams repeatedly intersect at specific locations (dots), where they interfere either constructively or destructively. This type of optical system is especially valuable in the field of quantum technology, where a network of optical switches is essential for selectively addressing individual optically active qubits. Conventional methods, have so far among other reasons been limited by high coupling losses, restricting the number of interconnected switches to only a few. The concept of zero diffraction could mean a significant advancement in overcoming these limitations, a prospect that will be explored further in subsequent research.

The subsequent Chapter 5 was focused on plasmonic waveguides, introduced as a classical approach of miniaturization by using plasmonic effects. The fundamental idea behind this research is that an optical structure grown under specific illumination conditions becomes highly sensitive to any changes in those conditions. The presented structures were based on a planar plasmonic stack combined with a metasurface that can interact with the planar waveguide.

The inherent adaptability of the AgNPs during growth enables the creation of a metasurface with an optical response, such as reflection or scattering, which is highly sensitive to even minute changes in the surrounding electromagnetic environment. This sensitivity is a critical feature for high-performance sensing applications, where precise detection of small environmental variations (e.g. by molecule binding events) is essential. Conventionally, after nanostructures are fabricated, they must be removed from the fabrication environment, which introduces the need for complex post-process alignment with respect to the probing light source. This additional step can increase the complexity of the system, reduce precision, and introduce alignment errors. In the approach presented in Chapter 5.2, the identical light source can be used for both fabrication and probing. This eliminates the need for post-fabrication adjustments, as the incident angle of the light is already perfectly aligned with the sharp resonances of the metasurface that emerge during fabrication. By utilizing multiple

waveguide modes simultaneously, e.g. modes that have substantially different penetration depths into the analyte, can be very benefitial for enhancing the selectivity of the sensor.

In addition, the harnessing of SR-SPPs in planar silver films has been demonstrated through plasmon-mediated growth of plasmonic metasurfaces. This method enables a facile way for the utilization of this hybridization phenomenon. Although several methods for utilizing the phenomenon are known in the literature, there is an important aspect I would like to emphasize at this point.[138] The key advantage of the method presented in this thesis is that the high losses—and the associated short propagation length— of the SR-SPP mode do not govern the width of the spectral features. Instead, the sharpness is determined by the size of the area that is coherently illuminated by the incident laser as well as the laser divergence. This is because, under growth conditions, the lossy SR-SPP mode does in fact not interact with the metasurface anymore (**dark** structure rings in the FTEM). Instead, the waveguide behaves as in the low loss case without the metasurface (before the particle growth) at this particular position. In close spectral proximity, however, the interaction between waveguide mode and metasurface is present again. Therefore, the feature width is not dependent on the losses of the mode involved in the particle growth but on the size of the illumination area and the laser beam divergence. This way, in this waveguide system, both the advantages of the strong localization of the SR-SPP mode and the spectral sharpness, which corresponds to the delocalized excitation of the particle ensemble, can be harnessed. Future work in this field will focus on optimizing light-controlled growth, exploring additional excitation schemes, and investigating other material compositions.

Chapter 6 focused on the development of materials for the efficient phase switching of light. Initially, PDMS/NLO liquid composite materials fabricated via swelling were studied. The nonlinearity of the composite materials was characterized by the Z-Scan technique. An especially interesting aspect was the importance of multiple parameters in material selection. For instance, the material with the strongest nonlinearity is not necessarily the most suitable one for the composite material, because of the material specific swelling behaviour. Also, the observation that the properties of PDMS/TL composite samples cannot be explained by a simple superposition of the individual material properties could be substantial. This suggests the presence of an effect that potentially enables the reduction of parasitic thermal nonlinearities through a specific material combination. Additionally, it was observed that,

under high illumination intensity, a permanent change in the refractive index seems to occur. In this context, further experiments are needed to determine whether this phenomenon could be applicable for laser-based structuring in material processing applications.

In the next section 6.2, thermal effects, particularly pronounced in nitrobenzene, were investigated. It was discovered that the nonlinear properties of nitrobenzene can be controlled by applying an external electric field. Through the continuous exchange of material under the influence of the electric field, the thermal contributions are continuously modified. As a result, the material can exhibit either a positive or negative nonlinear refractive index, depending on the field strength. This finding is particularly interesting for applications in electrically tuneable nonlinear lenses, as it allows the device to switch from self-focusing to self-defocusing behaviour.

Additionally, these studies aimed to clarify the timescales on which thermal nonlinearities occur in nitrobenzene, to assess its potential use in switchable waveguides where speed is not the primary requirement. One example is the use of such waveguides as adaptive light concentrators in photovoltaics. Since the position of the sun changes gradually over time, thermal nonlinearities could serve as a mechanism for optical adaptation in this context.

The thesis concluded with Section 6.3, which introduced DEAs as an alternative to conventional NLO materials. For this purpose, the phase of a laser beam was measured in an interferometer, where the path length changes due to the electromechanical deformation of an elastomer. Future activities will focus primarily on the use of even softer materials and the application of an electrical or mechanical bias, aiming to reduce the operating voltage required for a π phase shift.

List of References

1. A. Willner, *Optical Fiber Telecommunications*. Vol. 6., Academic Press, Waltham, USA (2019).

2. Essiambre, R. J. & Tkach, R. W., Capacity trends and limits of optical communication networks*. Proceedings of the IEEE* **100,** 1035–1055 (2012).

3. Xiong, J., Hsiang, E.-L., He, Z., Zhan, T. & Wu, S.-T., Augmented reality and virtual reality displays: emerging technologies and future perspectives. *Light Sci. Appl.* **10**, 216 (2021).

4. Huang, D. et al. *Optical Coherence Tomography*. *Science,* **254**, 1178–1181 (1991).

5. Leal-Junior, A. G. et al., Polymer Optical Fiber Sensors in Healthcare Applications: A Comprehensive Review. *Sensors* **19**, (2019).

6. Boas, D. A., Pitris, C. & Ramanujam, N., Handbook of biomedical optics. *BioMedical Engineering OnLine,* **11** (2012).

7. Wang, X., Li, Z. & Su, L., Soft Optical Waveguides for Biomedical Applications, Wearable Devices, and Soft Robotics: A Review. *Adv. Intell. Syst.* **6**, 2300482 (2024).

8. Nizamoglu, S. et al., Bioabsorbable polymer optical waveguides for deep-tissue photomedicine. *Nat. Commun.* **7**, 10374 (2016).

9. Berthold, J. W., INDUSTRIAL APPLICATIONS OF FIBER OPTIC SENSOR. *Fiber Optic Sensors* 573–591 (2024).

10. Majumdar, J. D. & Manna, I., Laser material processing. *Int. Mater. Rev.* **56**, 341–388 (2011).

11. Leach, R., Optical Measurement of Surface Topography. Springer, Berlin Heidelberg (2011).

12. Panda, P. & Chakroborty, S., Optical sensor technology and its application in detecting environmental effluents: a review. *Int. J. Environ. Anal. Chem.* **104**, 4057–4072 (2024).

13. Murphy, K. et al*.,* A low-cost autonomous optical sensor for water quality monitoring. *Talanta* **132**, 520–527 (2015).

14. Vikesland, P. J., Nanosensors for water quality monitoring. *Nat. Nanotechnol.* **13**, 651–660 (2018).

15. Becher, C. et al., 2023 roadmap for materials for quantum technologies. *Mater. Quantum Technol.* **3**, 12501 (2023).

16. O'Brien, J. L., Furusawa, A. & Vučković, J., Photonic quantum technologies. *Nat. Photonics* **3**, 687–695 (2009).

17. Jones, F. R., Glass fibres. *Woodhead Publishing Limited and CRC Press LLC*, Sawston, USA (2001).

18. Xu, Y. *et al.,* Optical Refractive Index Sensors with Plasmonic and Photonic Structures: Promising and Inconvenient Truth. *Adv. Opt. Mater.* **7**, 1801433 (2019).

19. Holmström, S. T. S., Baran, U. & Urey, H., MEMS laser scanners: A review. *J. Microelectromechanical Syst.* **23**, 259–275 (2014).

20. Wang, D., Watkins, C. & Xie, H., MEMS Mirrors for LiDAR: A Review. *Micromachines* **11**, (2020).

21. Boyd, R. W., *Nonlinear Optics*. 3. Edition, Academic Press (2008).

22. Mandal, M. et al*.,* A review of electro-optic, semiconductor optical amplifier and photonic crystal-based optical switches for application in quantum computing. *J. Opt.* **52**, 603–611 (2023).

23. Kaino, T. & Tomaru, S., Organic materials for nonlinear optics. *Adv. Mater.* **5**, 172–178 (1993).

24. Giordmaine, J. A., Nonlinear Optical Properties of Liquids. *Phys. Rev.* **138**, 1599-1606 (1965).

25. Milton, K. & Schwinger, J., *Classical electrodynamics*. CRC Press (2024).

26. Suter, U. W. & Flory, P. J., Optical anisotropy of polystyrene and its low molecular analogues. *J. Chem. Soc. Faraday Trans. 2* **73**, 1521–1537 (1977).

27. Kinase, W., Kobayashi, J. & Yamada, N., Optical Anisotropy of Tetragonal Barium Titanate. *Phys. Rev.* **116**, 348–350 (1959).

28. Hansson, G., Karlsson, H., Wang, S. & Laurell, F., Transmission measurements in KTP and isomorphic compounds. *Appl. Opt.* **39**, 5058–5069 (2000).

29. Garmire, E., Nonlinear optics in daily life. *Opt. Express* **21**, 30532 (2013).

30. Liu, K., Ye, C. R., Khan, S. & Sorger, V. J., Review and perspective on ultrafast wavelength-size electro-optic modulators. *Laser Photonics Rev.* **9**, 172–194 (2015).

31. Saleh, B. E. A. & Teich, M. C., Fundamentals of Photonics. *John Wiley & Sons*, New York, USA (2019).

32. Agrawal, G. P., Nonlinear fiber optics. in Nonlinear Science at the Dawn of the 21st Century 195–211, *Springer*, Berlin Heidelberg (2000).

33. Ho, P. P. & Alfano, R. R., Optical Kerr effect in liquids. *Phys. Rev. A* **20**, 2170–2187 (1979).

34. Kalpouzos, C., Lotshaw, W. T., McMorrow, D. & Kenney-Wallace, G. A., Femtosecond laser-induced Kerr responses in liquid carbon disulfide. *J. Phys. Chem.* **91**, 2028–2030 (1987).

35. Palese, S., Schilling, L., Miller, R. J. D., Staver, P. R. & Lotshaw, W. T., Femtosecond optical Kerr effect studies of water. *J. Phys. Chem.* **98**, 6308–6316 (1994).

36. Smith, N. A. & Meech, S. R., Ultrafast Dynamics of Polar Monosubstituted Benzene Liquids Studied by the Femtosecond Optical Kerr Effect. *J. Phys. Chem. A* **104**, 4223–4235 (2000).

37. Bongu, S. R., Buchmüller, M., Neumaier, D. & Görrn, P., Electric Control of Thermal Contributions to the Nonlinear Optical Properties of Nitrobenzene. *Adv. Phys. Res.* **3** (1), 2300053 (2024).

38. Bautista, J. E. Q. et al., Thermal and non-thermal intensity dependent optical nonlinearities in ethanol at 800 nm, 1480 nm, and 1560 nm. *J. Opt. Soc. Am. B* **38**, 1104–1111 (2021).

39. Khurgin, J. B., Sun, G., Chen, W. T., Tsai, W.-Y. & Tsai, D. P., Ultrafast Thermal Nonlinearity. *Sci. Rep.* **5**, 17899 (2015).

40. Minovich, A. E. et al., Functional and nonlinear optical metasurfaces. *Laser Photon. Rev.* **9**, 195–213 (2015).

41. Wu, L. et al*.,* Recent Advances of Spatial Self-Phase Modulation in 2D Materials and Passive Photonic Device Applications. *Small* **16**, 2002252 (2020).

42. Maier, S. A., Plasmonics: Fundamentals And Applications, *Springer*, Berlin Heidelberg, (2007).

43. Raether, H., Surface plasmons on smooth surfaces. in Surface Plasmons on Smooth and Rough Surfaces and on Gratings, *Springer*, Berlin Heidelberg, (1988).

44. Kang, L., Jenkins, R. P. & Werner, D. H., Recent Progress in Active Optical Metasurfaces. *Adv. Opt. Mater.* **7**, 1801813 (2019).

45. Padilla, W. J., Basov, D. N. & Smith, D. R., Negative refractive index metamaterials. *Mater. Today* **9**, 28–35 (2006).

46. Chen, M. K. et al*.,* Principles, Functions, and Applications of Optical Meta-Lens. *Adv. Opt. Mater.* **9**, 2001414 (2021).

47. Khan, S. A. et al., Optical Sensing by Metamaterials and Metasurfaces: From Physics to Biomolecule Detection. *Adv. Opt. Mater.* **10**, 2200500 (2022).

48. Ni, X., Kildishev, A. V & Shalaev, V. M., Metasurface holograms for visible light. *Nat. Commun.* **4**, 2807 (2013).

49. Zheng, G. et al*.,* Metasurface holograms reaching 80% efficiency. *Nat. Nanotechnol.* **10**, 308–312 (2015).

50. Chang, C.-C. et al., High-Temperature Refractory Metasurfaces for Solar Thermophotovoltaic Energy Harvesting. *Nano Lett.* **18**, 7665–7673 (2018).

51. Lan, S. et al., Metasurfaces for Near-Eye Augmented Reality. *ACS Photonics* **6**, 864–870 (2019).

52. Lee, G.-Y. et al*.,* Metasurface eyepiece for augmented reality. *Nat. Commun.* **9**, 4562 (2018).

53. Luo, Y. et al*.,* Metasurface-Based Abrupt Autofocusing Beam for Biomedical

Applications. *Small Methods* **6**, 2101228 (2022).

54. Qiu, C.-W., Zhang, T., Hu, G. & Kivshar, Y., Quo Vadis, Metasurfaces? *Nano Lett.* **21**, 5461–5474 (2021).

55. Zhang, S. *et al.,* Metasurfaces for biomedical applications: imaging and sensing from a nanophotonics perspective. *Nanophotonics* **10**, 259–293 (2021).

56. Wang, K., Chekhova, M. & Kivshar, Y., Metasurfaces for quantum technologies. *Phys. Today* **75**, 38–44 (2022).

57. Su, V.-C., Huang, S.-Y., Chen, M.-H., Chiang, C.-H. & Xu, K.-L., Optical Metasurfaces for Tunable Vortex Beams. *Adv. Opt. Mater.* **11**, 2301841 (2023).

58. Georgi, P. et al*.,* Metasurface interferometry toward quantum sensors. *Light Sci. Appl.* **8**, 70 (2019).

59. Fromm, D. P., Sundaramurthy, A., James Schuck, P., Kino, G. & Moerner, W. E., Gap-dependent optical coupling of single 'bowtie' nanoantennas resonant in the visible. *Nano Lett.* **4**, 957–961 (2004).

60. Horák, M. et al*.,* Comparative study of plasmonic antennas fabricated by electron beam and focused ion beam lithography. *Sci. Rep.* **8**, 1–8 (2018).

61. Pelton, M., Aizpurua, J. & Bryant, G., Metal-nanoparticle plasmonics. *Laser Photonics Rev.* **2**, 136–159 (2008).

62. Girard, C., Near fields in nanostructures. *Reports Prog. Phys.* **68**, 1883–1933 (2005).

63. Lv, J. T. et al*.,* Plasmonic nanoantennae fabricated by focused Ion beam milling. *Int. J. Precis. Eng. Manuf.* **16**, 851–855 (2015).

64. Tseng, A. A., Recent developments in micromilling using focused ion beam technology. *J. Micromechanics Microengineering* **14**, (2004).

65. Mayer, M., Schnepf, M. J., König, T. A. F. & Fery, A., Colloidal Self-Assembly Concepts for Plasmonic Metasurfaces. *Adv. Opt. Mater.* **7**, 1800564 (2019).

66. Rycenga, M. et al*.,* Controlling the synthesis and assembly of silver nanostructures for plasmonic applications. *Chem. Rev.* **111**, 3669–3712 (2011).

67. Li, S. et al., A green-light gain-assisted metamaterial fabricated by self-assembled electrochemical deposition. *Appl. Phys. Lett.* **103**, 181910 (2013).

68. Härtling, T. et al., Photochemical tuning of plasmon resonances in single gold nanoparticles. *J. Phys. Chem. C* **112**, 4920–4924 (2008).

69. Paul, A., Kenens, B., Hofkens, J. & Uji-i, H., Excitation polarization sensitivity of plasmon-mediated silver nanotriangle growth on a surface. *Langmuir* **28**, 8920–8925 (2012).

70. Scarabelli, L., Coronado-Puchau, M., Giner-Casares, J. J., Langer, J. & Liz-Marzán, L. M., Monodisperse gold nanotriangles: Size control, large-scale self-assembly, and performance in surface-enhanced raman scattering. *ACS Nano* **8**, 5833–5842 (2014).

71. Sutter, P., Li, Y., Argyropoulos, C. & Sutter, E., In Situ Electron Microscopy of Plasmon-Mediated Nanocrystal Synthesis. *J. Am. Chem. Soc.* **139**, 6771–6776 (2017).

72. Brooks, J. L., Warkentin, C. L., Saha, D., Keller, E. L. & Frontiera, R. R., Toward a mechanistic understanding of plasmon-mediated photocatalysis. *Nanophotonics* **7**, 1697–1724 (2018).

73. Zhang, Y. et al., Surface-Plasmon-Driven Hot Electron Photochemistry. *Chem. Rev.* **118**, 2927–2954 (2018).

74. Zhang, J., Langille, M. R. & Mirkin, C. A., Synthesis of silver nanorods by low energy excitation of spherical plasmonic seeds. *Nano Lett.* **11**, 2495–2498 (2011).

75. Langille, M. R., Personick, M. L. & Mirkin, C. A., Plasmon-mediated syntheses of metallic nanostructures. *Angew. Chemie - Int. Ed.* **52**, 13910–13940 (2013).

76. Bjerneld, E. J., Murty, K. V. G. K., Prikulis, J. & Käll, M., Laser-induced growth of Ag nanoparticles from aqueous solutions. *ChemPhysChem* **3**, 116–119 (2002).

77. Bjerneld, E. J., Svedberg, F. & Käll, M., Laser induced growth and deposition of noble-metal nanoparticles for surface-enhanced Raman scattering. *Nano Lett.* **3**, 593–596 (2003).

78. Park, J. S., Yoon, J. H. & Yoon, S., Spatially controlled SERS patterning using photoinduced disassembly of gelated gold nanoparticle aggregates. *Langmuir* **26**, 17808–17811 (2010).

79. Liu, T., Wang, W., Liu, F. & Wang, S., Photochemical deposition fabricated highly sensitive localized surface plasmon resonance based optical fiber sensor. *Opt. Commun.* **427**, 301–305 (2018).

80. Yu, S., Qiu, C.-W., Chong, Y., Torquato, S. & Park, N., Engineered disorder in photonics. *Nat. Rev. Mater.* (2020) doi:10.1038/s41578-020-00263-y.

81. Merkel, M., Stappers, M., Ray, D., Denz, C. & Imbrock, J., Stealthy Hyperuniform Surface Structures for Efficiency Enhancement of Organic Solar Cells. *Adv. Photonics Res.* **5**, 2300256 (2024).

82. Ko, J. H. et al*.,* Lithography-Free, Large-Area Spatially Segmented Disordered Structure for Light Harvesting in Photovoltaic Modules. *ACS Appl. Mater. Interfaces* **14**, 44419–44428 (2022).

83. Torquato, S. & Stillinger, F. H., Local density fluctuations, hyperuniformity, and order metrics. *Phys. Rev. E* **68**, 41113 (2003).

84. Chen, D. & Torquato, S., Designing disordered hyperuniform two-phase materials with novel physical properties. *Acta Mater.* **142**, 152–161 (2018).

85. Philcox, O. H. E. & Torquato, S., Disordered Heterogeneous Universe: Galaxy Distribution and Clustering across Length Scales. *Phys. Rev. X* **13**, 11038 (2023).

86. Florescu, M., Torquato, S. & Steinhardt, P. J., Designer disordered materials with large, complete photonic band gaps. *Proc. Natl. Acad. Sci.* **106**, 20658 LP – 20663 (2009).

87. Man, W. et al*.,* Isotropic band gaps and freeform waveguides observed in hyperuniform disordered photonic solids. *Proc. Natl. Acad. Sci. U. S. A.* **110**, 15886–15891 (2013).

88. Piechulla, P. M. et al*.,* Antireflective Huygens' Metasurface with Correlated Disorder Made from High-Index Disks Implemented into Silicon Heterojunction Solar Cells. *ACS Photonics* **8**, 3476–3485 (2021).

89. Gorsky, S. et al*.,* Engineered hyperuniformity for directional light extraction. *APL Photonics* **4**, 110801 (2019).

90. Zito, G., Rusciano, G., Pesce, G., Dochshanov, A. & Sasso, A., Surface-enhanced Raman imaging of cell membrane by a highly homogeneous and isotropic silver nanostructure.

Nanoscale **7**, 8593–8606 (2015).

91. Piechulla, P. M. et al*.,* Tailored Light Scattering through Hyperuniform Disorder in Self-Organized Arrays of High-Index Nanodisks. *Adv. Opt. Mater.* **9**, 2100186 (2021).

92. Kim, J. & Torquato, S., Effect of imperfections on the hyperuniformity of many-body systems. *Phys. Rev. B* **97**, 54105 (2018).

93. Castro-Lopez, M. et al*.,* Reciprocal space engineering with hyperuniform gold disordered surfaces. *APL Photonics* **2**, 61302 (2017).

94. Piechulla, P. M. et al*.,* Fabrication of Nearly-Hyperuniform Substrates by Tailored Disorder for Photonic Applications. *Adv. Opt. Mater.* **6**, 1701272 (2018).

95. Lee, J. N., Park, C. & Whitesides, G. M., Solvent Compatibility of Poly(dimethylsiloxane)-Based Microfluidic Devices. *Anal. Chem.* **75**, 6544–6554 (2003).

96. Polywka, A., Vereshchaeva, A., Riedl, T. & Görrn, P., Manipulating the morphology of silver nanoparticles with local plasmon-mediated control. *Part. Part. Syst. Charact.* **31**, 342–346 (2014).

97. Meudt, M. et al*.,* Plasmonic Black Metasurface by Transfer Printing. *Adv. Mater. Technol.* **3**, 1800124 (2018).

98. Jakob, T. et al*.,* Transfer printing of electrodes for organic devices: nanoscale versus macroscale continuity. *Appl. Phys. A* **120**, 503–508 (2015).

99. Trost, S. et al*.,* Plasmonically sensitized metal-oxide electron extraction layers for organic solar cells. *Sci. Rep.* **5**, 1–9 (2015).

100. Saito, Y., Wang, J. J., Smith, D. A. & Batchelder, D. N. A, Simple Chemical Method for the Preparation of Silver Surfaces for Efficient SERS. *Langmuir* **18**, 2959–2961 (2002).

101. Polywka, A., Tückmantel, C. & Görrn, P., Light controlled assembly of silver nanoparticles. *Sci. Rep.* **7**, 45144 (2017).

102. Polywka, A., Jakob, T., Stegers, L., Riedl, T. & Görrn, P., Facile Preparation of High-Performance Elastically Stretchable Interconnects. *Adv. Mater.* **27**, 3755–3759 (2015).

103. Shutsko, I. et al*.,* Enhanced hybrid optics by growing silver nanoparticles at local

intensity hot spots. *Nanophotonics* **8**, 1457–1464 (2019).

104. Sheik-bahae, M., Said, A. A. & Van Stryland, E. W., High-sensitivity, single-beam n_2 measurements. *Opt. Lett.* **14**, 955 (1989).

105. Sheik-Bahae, M., Said, A. A., Wei, T. H., Hagan, D. J. & Van Stryland, E. W., Sensitive Measurement of Optical Nonlinearities Using a Single Beam. *IEEE J. Quantum Electron.* **26**, 760–769 (1990).

106. Görrn, P., Rabe, T., Riedl, T. & Kowalsky, W., Loss reduction in fully contacted organic laser waveguides using TE 2 modes. *Appl. Phys. Lett.* (2007).

107. Görrn, P., Waveguide, Method of projecting light from a waveguide, and display. US Patent 10,739,623. (2016).

108. Meudt, M., Bogiadzi, C., Wrobel, K. & Görrn, P., Hybrid Photonic–Plasmonic Bound States in Continuum for Enhanced Light Manipulation. *Adv. Opt. Mater.* **8**, 2000898 (2020).

109. Meudt, M., Henkel, A., Buchmüller, M. & Görrn, P., A Theoretical Description of Node-Aligned Resonant Waveguide Gratings. Optics **3** (1), 60-69 (2022).

110. Kurahashi, N. et al*.,* Distributed Feedback Lasing in Thermally Imprinted Phase-Stabilized CsPbI 3 Thin Films. *Adv. Funct. Mater. **34** (45),* 2405976 (2024).

111. Meudt, M., Passive and Active Waveguide Systems for Solar Concentrators. Dissertation, Bergische Universität Wuppertal (2022).

112. Mak, K. F., Lee, C., Hone, J., Shan, J. & Heinz, T. F., Atomically Thin MoS2: A New Direct-Gap Semiconductor. *Phys. Rev. Lett.* **105**, 136805 (2010).

113. Novoselov, K. S. et al*.,* Electric Field Effect in Atomically Thin Carbon Films. *Science* **306**, 666–669 (2004).

114. Gervais, F. & Fonseca, V., Lithium Tantalate (LiTaO3). in Handbook of Optical Constants of Solids 777–805, Academic Press (1997).

115. Kumada, A. & Hidaka, K., Directly High-Voltage Measuring System Based on Pockels Effect. *IEEE Trans. Power Deliv.* **28**, 1306–1313 (2013).

116. von Neumann, J. & Wigner, E. P., Über merkwürdige diskrete Eigenwerte. in The Collected Works of Eugene Paul Wigner: Part A: The Scientific Papers 291–293, *Springer*, Berlin Heidelberg (1993).

117. Parker, R. Resonance effects in wake shedding from parallel plates: Some experimental observations. *J. Sound Vib.* **4**, 62–72 (1966).

118. Plotnik, Y. et al*.,* Experimental Observation of Optical Bound States in the Continuum. *Phys. Rev. Lett.* **107**, 183901 (2011).

119. Hsu, C. W. et al*.,* Observation of trapped light within the radiation continuum. *Nature* **499**, 188 (2013).

120. Hsu, C. W., Zhen, B., Stone, A. D., Joannopoulos, J. D. & Soljačić, M., Bound states in the continuum. *Nat. Rev. Mater.* **1**, 16048 (2016).

121. Kodigala, A. et al., Lasing action from photonic bound states in continuum. *Nature* **541**, 196–199 (2017).

122. Romano, S. et al., Optical Biosensors Based on Photonic Crystals Supporting Bound States in the Continuum. *Materials (Basel).* **11**, (2018).

123. Zhang, Z. et al*.,* Coherent Perfect Diffraction in Metagratings. *Adv. Mater.* **32**, 1–6 (2020).

124. Saleh, B. E. A. & Teich, M. C., Fundamentals of Photonics. *John Wiley & Sons*, New York, USA (2019).

125. Görrn, P., Wellenleiteranordnung und Verfahren zur Ablenkung wenigstens eines Lichtstrahls bzw. Lichtstrahlpaares. Patent DE102021127637A1 (2023).

126. Wurtz, G. A. et al*.,* Designed ultrafast optical nonlinearity in a plasmonic nanorod metamaterial enhanced by nonlocality. *Nat. Nanotechnol.* **6**, 107–111 (2011).

127. Reshef, O. et al*.,* Multiresonant High-Q Plasmonic Metasurfaces. *Nano Lett.* **19**, 6429–6434 (2019).

128. Wang, B. et al., High-Q Plasmonic Resonances: Fundamentals and Applications. *Adv. Opt. Mater.* **9**, 2001520 (2021).

129. Liang, Y., Tsai, D. P. & Kivshar, Y., From Local to Nonlocal High-Q Plasmonic Metasurfaces. *Phys. Rev. Lett.* **133**, 53801 (2024).

130. Bin-Alam, M. S. et al*.,* Ultra-high-Q resonances in plasmonic metasurfaces. *Nat. Commun.* **12**, 974 (2021).

131. Torquato, S., Disordered hyperuniform heterogeneous materials. *J. Phys. Condens. Matter* **28**, 414012 (2016).

132. Tavakoli, N. et al*.,* Over 65% Sunlight Absorption in a 1 μm Si Slab with Hyperuniform Texture. *ACS Photonics* **9**, 1206–1217 (2022).

133. Shutsko, I., Buchmüller, M., Meudt, M. & Görrn, P., Plasmon-Induced Disorder Engineering for Robust Optical Sensors. *Adv. Opt. Mater.* **10**, 2102783 (2022).

134. Yu, S., Qiu, C.-W., Chong, Y., Torquato, S. & Park, N., Engineered disorder in photonics. *Nat. Rev. Mater.* **6**, 226–243 (2021).

135. Torquato, S., Hyperuniformity and its generalizations. *Phys. Rev. E* **94**, 22122 (2016).

136. Fan, B. et al*.,* Refractive index sensor based on hybrid coupler with short-range surface plasmon polariton and dielectric waveguide. *Appl. Phys. Lett.* **100**, 111108 (2012).

137. Yanai, A. & Levy, U., The role of short and long range surface plasmons for plasmonic focusing applications. *Opt. Express* **17**, 14270–14280 (2009).

138. Frank, B. et al*.,* Short-range surface plasmonics: Localized electron emission dynamics from a 60-nm spot on an atomically flat single-crystalline gold surface. *Sci. Adv.* **3**, e1700721 (2017).

139. Tuniz, A., Chemnitz, M., Dellith, J., Weidlich, S. & Schmidt, M. A., Hybrid-Mode-Assisted Long-Distance Excitation of Short-Range Surface Plasmons in a Nanotip-Enhanced Step-Index Fiber. *Nano Lett.* **17**, 631–637 (2017).

140. Berini, P., Long-range surface plasmon polaritons. *Adv. Opt. Photon.* **1**, 484–588 (2009).

141. Qi, D., Zhang, K., Tian, G., Jiang, B. & Huang, Y., Stretchable Electronics Based on PDMS Substrates. *Adv. Mater.* **33**, 2003155 (2021).

142. Polywka, A., Jakob, T., Stegers, L., Riedl, T. & Görrn, P., Facile Preparation of High-

Performance Elastically Stretchable Interconnects. *Adv. Mater.* **27**, 3755–3759 (2015).

143. Li, X. et al*.,* Stretchable Binary Fresnel Lens for Focus Tuning. *Sci. Rep.* **6**, 25348 (2016).

144. Kolaric, B., Desprez, S., Brau, F. & Damman, P., Design of curved photonic crystal using swelling induced instabilities. *J. Mater. Chem.* **22**, 16205–16208 (2012).

145. Usui, K., Matsumoto, K., Katayama, E., Akamatsu, N. & Shishido, A., A Deformable Low-Threshold Optical Limiter with Oligothiophene-Doped Liquid Crystals. *ACS Appl. Mater. Interfaces* **13**, 23049–23056 (2021).

146. Haripadmam, P. C., Thanuja, T. H., Varsha, G. S., Beryl, C. D. & Aji, A., Nonlinear optical absorption in PVA films doped by the novel natural dye extract from C. redflash leaves. *Opt. Mater. (Amst).* **112**, 110804 (2021).

147. Fu, B. et al*.,* Recent Progress on Metal-Based Nanomaterials: Fabrications, Optical Properties, and Applications in Ultrafast Photonics. *Adv. Funct. Mater.* **31**, 2107363 (2021).

148. Bai, T. et al*.,* CH3NH3PbI3 perovskite:poly(N-vinylcarbazole) blends for broadband optical limiting. *RSC Adv.* **7**, 1809–1813 (2017).

149. Johnson, V. & Gandhiraj, V., Enhanced nonlinear characteristics of polymer-perovskite hybrid (PVA/CMC/LaAlO3) fabricated via solution casting process for optical limiting applications. *J. Mater. Sci. Mater. Electron.* **34**, 2103 (2023).

150. Guo, J. et al*.,* Graphdiyne-Polymer Nanocomposite as a Broadband and Robust Saturable Absorber for Ultrafast Photonics. *Laser Photon. Rev.* **14**, 1900367 (2020).

151. Mu, H. et al., Black Phosphorus–Polymer Composites for Pulsed Lasers. *Adv. Opt. Mater.* **3**, 1447–1453 (2015).

152. Hellwarth, R. W., Effect of Molecular Redistribution on the Nonlinear Refractive Index of Liquids. *Phys. Rev.* **152**, 156–165 (1966).

153. Piazza, R., Degiorgio, V. & Bellini, T., Kerr effect in binary liquid mixtures. *J. Opt. Soc. Am. B* **3**, 1642–1646 (1986).

154. Kedenburg, S., Vieweg, M., Gissibl, T. & Giessen, H., Linear refractive index and

absorption measurements of nonlinear optical liquids in the visible and near-infrared spectral region. *Opt. Mater. Express* **2**, 1588–1611 (2012).

155. Cabrera, M. H., Marcano, O. A. & Ojeda, A. J., Absorption Spectra of Nitrobenzene Measured With Incoherent White-Light Excitation. *AIP Conf. Proc.* **992**, 1183–1188 (2008).

156. Bongu, S. R., Buchmüller, M., Neumaier, D. & Görrn, P., Electric Control of Thermal Contributions to the Nonlinear Optical Properties of Nitrobenzene. *Adv. Phys. Res.* **3**, 1–7 (2024).

157. Mielczarek, M., Charakterisierung von Elastomeren zur elektromechanischen Phasenmodulation eines Laserstrahls, Bachelor-Thesis, Bergische Universität Wuppertal, (2022).

158. Kaal, W. & Herold, S., Electroactive Polymer Actuators in Dynamic Applications. *IEEE/ASME Trans. Mechatronics* **16**, 24–32 (2011).

159. Keplinger, C. et al., Stretchable, Transparent, Ionic Conductors. *Science* **341**, 984–987 (2013).

160. Henkel, A., Knoth, C., Buchmüller, M. & Görrn, P., Electric Control of the In-Plane Deflection of Laser Beam Pairs within a Photonic Slab Waveguide. *Optics* **5**, 342–352 (2024).